NANOSCINTOMETRY : A PATHWAY TO ABSOLUTE DOSIMETRY OF IONISING RADIATIONS.

Ian Cameron McDougall

A Thesis Submitted for the Degree of PhD
at the
University of St Andrews

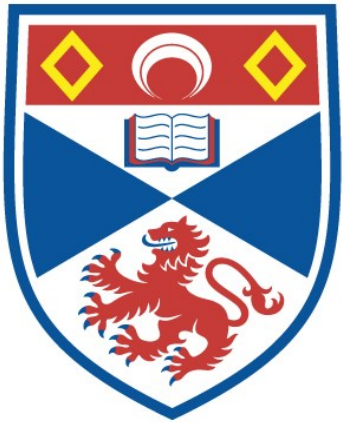

1998

Nanoscintometry

A Pathway to Absolute Dosimetry of Ionising Radiations

by

Ian Cameron McDougall

B.Sc (Dundee Institute of Technology), GradInstP, M.Sc (St Andrews)

A Thesis Submitted for the Degree of Doctor of Philosophy

at the University of St. Andrews

July 1998

ProQuest LLC.
789 East Eisenhower Parkway
P.O. Box 1346
Ann Arbor, MI 48106 – 1346

Thesis Organisation

Declaration

I, Ian Cameron McDougall, hereby declare that this thesis has been composed by myself, that it is a record of my own work, and that it has not been accepted in partial or complete fulfilment of any other degree or professional qualification.

Ian C. McDougall

July, 1998

Acknowledgements

I would like to thank my supervisor, Dr. D. E. Watt, for the support, guidance and encouragement he has given me throughout this project, and for his boundless enthusiasm that made it all possible.

A huge debt of gratitude must also be paid to Dr G.E. Thomas of the University of Dundee for his guidance and perseverance in developing our statistical models. Thanks also must go to my colleagues, both past and present, in the Radiation Biophysics Unit, Dr J. S. P. Crossman, Dr M. Chaar, Dr R. M. Nassar, Dr A. S. Alkharam and J. Y. Tamboul for their endless discussions and humour. George Radley, George Cummingham and the staff of the Physics Workshop for their help in constructing various and often obscure pieces of equipment. Fritz Akerboom for his expertise with glass. Moira MacKenzie and the staff of the Physics/Maths Library for their help and swift service. Jim Park and the staff of the Electronics Workshop. Dr. B Grosswendt of PTB, Braunschweig in Germany for his useful suggestions on Monte Carlo modelling and the Commission of European Communities for supporting my research under contract F14PCT960044-NANDET.

Finally, I would like to thank my Mother and Father for their years of unfaltering support and encouragement, and for giving me the determination to continue when the light of hope burned so dim.

Certification

I hereby certify that the candidate, Ian Cameron McDougall, has fulfilled the conditions of the Resolution and Regulations of the University of St Andrews appropriate to the degree of Ph.D.

Signature of Supervisor

Date

.....1998.....

Better to travel in hope,
than arrive in doubt.

Dedication

To all those who made a difference in my life.

Abstract

It is now accepted that the deleterious effects induced by ionising radiations in mammalian cells are caused by the simultaneous breaking of both strands of the DNA helix by a single track. These effects are optimised when the mean free path of primary ionisation, λ, matches the 2 nanometre mean chord distribution of DNA. However, there is currently no method of measuring radiation damage in terms of λ. The aim of this project has been to design and construct a detector with a λ response function capable of providing a measure of the absolute biological effectiveness of a radiation, independent of radiation type.

Organic scintillation molecules, in the condensed phase, have been identified as being most suitable for bio-effectiveness measurements. Tissue equivalent and of comparable interaction cross-section, these nanodetectors are capable of signalling individual interactions with the emission of a scintillation photon, or scinton. Using a 20 μm scintillation film and DEP hybrid photodiode, spectra containing single and plural scinton events were recorded. These spectra reveal unique differences in the radiation quality of photon-emitting radioisotopes.

A model of radiation action on scintillators in the condensed phase, analogous to the direct and indirect actions observed in intra-cellular DNA, has been developed and used

to predict the characteristic yields of single and plural scinton events. The model was further developed to provide probabilities of 'paired' scinton events originating from fluor sites with a mean spacing of 2 nm. These critical 'paired' events are representative of double strand breaks and interpretation of these events that will yield bio-effectiveness data. Using Poisson distributions, a scintillator with optimised fluor concentration was developed for use in bio-effectiveness detectors.

Loss calculations within the detector revealed an inconsistency in exponential attenuation theory, which appears to be inadequate when applied to light-guides. Consequently a new model of photon transport in light-pipes based on a Monte Carlo simulation has been developed and offers a more rigorous alternative.

Calibration of the detector highlighted the need for a simple yet effective technique for photomultiplier tube (PMT) gain calibration in the laboratory. A technique using Cerenkov radiation was developed and provides good correlation with published gain figures.

Although this prototype detector has not yet been fully tested, nor the associated bio-effect model fully developed to allow extraction of bio-effectiveness data from the collected spectra, preliminary results suggest this technique to be promising alternative and offers a route towards the measurement of absolute dosimetry with potential application in radiotherapy and radiation protection.

List of Publications

McDougall, I. C., Alkharam, A. S., Thomas, G. E. and Watt, D. E., *A Scintillation Method for Measurement of the Bio-Effectiveness of Ionizing Radiations by Simulation of the Cellular Response.*, Proceedings of the IRPA Regional Symposium on Radiation Protection in Neighbouring Countries of Central Europe 1997, Prague, 548-551, 1997

McDougall, I. C. and Watt, D. E., *Calibration of Photomultiplier Systems Using Cerenkov Radiation.*, University Report BIOPHYS 4/97.

McDougall, I. C. and Watt, D. E., *Calibration of Photomultiplier Systems Using Cerenkov Radiation*, Submitted for publication

Table of Contents

List of Figures

List of Tables

Chapter I

Introduction

1.1 Introduction

In 1985, Watt proposed a radical re-appraisal of the effectiveness of the currently adopted method for assessment of radiation induced damage in fields of dosimetry and radiation protection. The new model proposed that radiation induced damage in mammalian cells could be assessed with far greater accuracy by use of the mean free path of primary ionisation rather than the current absorbed dose model which has proved to have inherent practical difficulties. The critical damage mechanism, the simultaneous breaking of both strands of the DNA helix, was found to be optimised when the primary charged particle radiation mean free path matched the mean chord separation of DNA, approximately 2 nm. Crucially, this finding proved to be independent of radiation type and thereby obviated the need for radiation quality factors.

Subsequent research and modelling by Alkharam (1997) and Watt *et al.* (1997), has provided evidence that all significant biological end-points, such as chromosomal aberrations, oncogenic transformations and cell inactivation, can be predicted from the initial yield of double strand breaks in the DNA induced during irradiation. Therefore, a method of detecting double strand DNA breaks as they are induced

would provide an accurate assay of the magnitude of radiation damage in *real-time*, unlike conventional TLDs and film badges which provide a somewhat delayed measure of accumulated absorbed dose from a purely historical view-point.

The physical practicalities of assessing yields of DNA double strand breaks in irradiated tissue prohibit direct analysis of tissue *in-vivo*, and thus an alternative detection protocol is required. In 1995, Watt suggested that organic scintillators might be used as microscopic radiation detectors which could simulate the response of mammalian DNA. By using a thin film of polymerised organic scintillator and analysing the yields of single and plural spatially correlated photons emitted while under irradiation, it is possible by statistical modelling, to derive the associated yield of double strand breaks that the same radiation field would induce in mammalian tissue. The design of just such a detector and the subsequent interpretation of its data is presented here.

This novel approach to dosimetry not only provides a method of more accurate assessment of radiation induced damage, but also provides a positive route towards absolute dosimetry of biological damage.

1.2 An Overview of Current Dosimetry

Currently, in both fields of radiation protection and medical radiotherapy, the energy deposition model is used to estimate risk factors for radiation exposure and optimum deliverable doses to inactivate clinical carcinomas. This model depends on a highly localised deposition of energy by the primary ion in biological tissue, leading to the production of high yields of δ-rays which are assumed to enhance the

inactivation efficiencies of the incident radiation. This has lead to an interest in high LET heavy ion therapy in the treatment of certain types of carcinoma.

Current legislation governing radiation protection based upon the LET model is recognised as having fundamental shortfalls. The most notable of these being the need for the radiation quality factor, introduced by the ICRU (ICRU Report 19, 1971), which incorporates a maximum correction factor of 20 to correlate the theoretically predicted dose risk of high LET particles with that observed in tissue.

When the LET based system of dosimetry was first postulated, models of radiation damage assumed that biological cellular structures alone were the radio-sensitive sites which responded to irradiation. However, it is now widely accepted that intranuclear DNA contains the critical radio-sensitive sites (Yang *et al.*, 1989 and Frankenberg, 1994), and more specifically, that double strand breaks in the DNA helix are the critical precursors to the formation of lesions in mammalian cells. However, measurement of the fundamental number of strand breaks is beyond the scope of the LET model as it concentrates on indiscriminate energy deposition within the cellular volume.

1.3 A New Approach to Dosimetry

The nucleus of a mammalian cell contains approximately 6 to 26 pg of double stranded DNA dependent on cell type which forms the biochemical means of communicating genetic heredity from one generation to the next during cell division. It also controls the overall function of the reproduction and apoptosis of each individual cell. In radiological protection, it is therefore essential to have some

measure of the damage induced in DNA for the assessment of the risk of cell inactivation or other radiological end-points.

DNA in its simplest form is a long chain polymer comprising sugar deoxyribose molecules linked together by phosphate groups. The sugars in each chain are themselves connected to one of four heterocyclic bases: cytosine, thymine, adenine and guanine, which in turn combine in pairs to form the double stranded DNA helix. Strands are separated by a mean chord length of approximately 2 nm.

When ionising radiation is incident upon and traverses through a biological target volume, it undergoes a series of electrostatic energy-dissipating interactions with bound molecular electrons along the entire length of the primary track. The magnitude of energy exchanged between primary radiation and electron in these interactions determines whether the bound electron is merely excited into a higher energy level or completely removed leaving behind an ionised molecule and producing a δ-ray.

In the confines of the mammalian cell nucleus, both excitation and ionisation events lead to the induction of single and multiple breaks in the molecular bonds of the double stranded DNA helix. Single strand breaks, though potentially lethal to the cell if associated with a highly localised concentration of additional single-strand breaks, are not inherently life threatening to the cell which can more than adequately recover from single strand damage using the cell's natural repair mechanisms. Double-strand DNA breaks are far more difficult to repair and have a potentially more lethal action on the nucleus. These double strand breaks are now generally considered to be the precursors of radiation induced damage in mammalian cells.

In 1995, Watt *et al.* proposed a revolutionary model that permitted the yield of initial individual DNA double strand breaks to be indirectly detected, thus providing

a method of determining the absolute biological effectiveness (ABE) of a radiation field. The model developed from earlier models (Watt *et al.*, 1985, Chen *et al.*, 1986, Watt, 1989(1) & 1989(2) and Watt *et al.*, 1990) in which the reciprocal of specific primary ionisation, or mean free path, λ, was shown to be a fundamental quality parameter which determined the likelihood of occurrence of the observed biological end-points induced by incident ionising radiations. As the mean free path of primary ionisation approaches close to and matches the mean chord length of the DNA helix, at approximately 2 nm, radiation induced effects are optimised. These enhancement effects are independent of radiation type. Any associated δ-ray contribution is shown to be minimal. When the same end-points are investigated in terms of LET and RBE, no such correlation is obtained. The effects are specifically the result of radiation events with the optimum mean spacing of primary ionisation.

Figure 1.1 illustrates the correlation obtained when ionisation mean free path, λ, is used as the fundamental quantity. A point of inflection at 1.5 nm is clearly visible and is attributed to the mean chord spacing of the strands of the DNA segment and identifies the double-strand break as the critical lesion for cell inactivation. This structure is only observed in the presence of double stranded DNA. Enzymes containing single stranded DNA, such as ϕX-174, do not exhibit this structure. The enhancement of inactivation damage above unity in the saturation region, $\lambda < 2$ nm, is attributed to high energy δ-rays escaping the primary cell nucleus and crossing into neighbouring cell nuclei where they may induce a double strand break.

Based upon these fundamental findings, a new and revolutionary approach towards radiation dosimetry is presented here. Operating at the nanometre level, the model of Nanoscintometry makes use of the novel concept of molecular

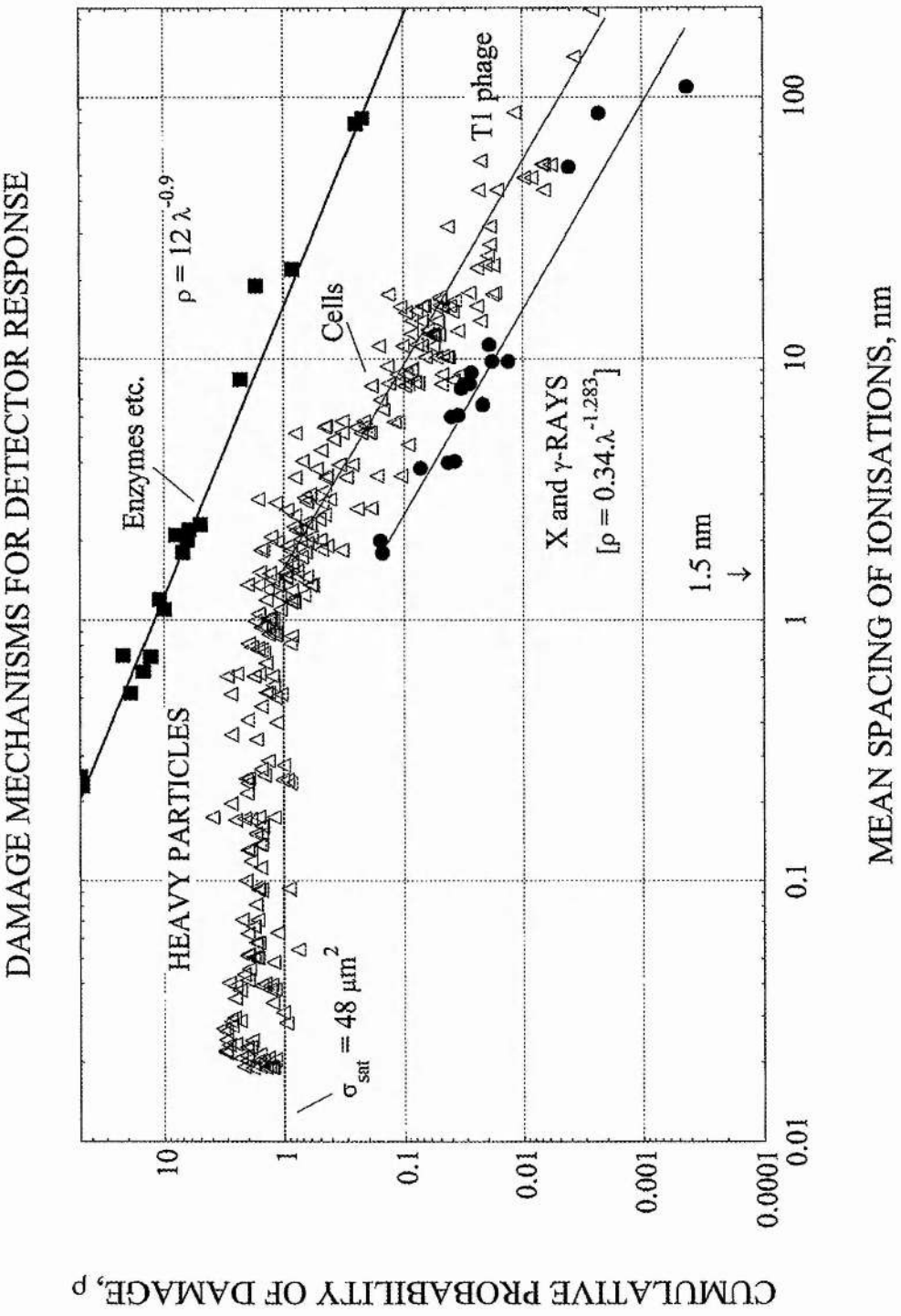

Figure 1.1 Cumulative damage probability as a function of primary charged particle mean free path (Watt, 1997).

nanodetectors to indirectly detect individual radiation interactions with the DNA helix by simulating critical DNA dimensions within the detector itself. With a response function closely matching that of the DNA, the proposed detector is capable of indirectly measuring the number of double strand breaks in the DNA helix, thus providing for the first time a measure of the absolute biological effectiveness of a radiation field that is independent of radiation type. There is no need for radiation quality factors.

Chapter II

Nanoscintometry:

A Pathway to Absolute Dosimetry?

2.1 Introduction

A detector capable of indirectly detecting a single DNA double-strand break would have to be comparable in size to a segment of the DNA itself, possessing a similar response function to radiation and capable of signalling individual occurrences of radiation interactions. Such detectors already exist in the form of organic scintillation molecules. Though differing significantly in both molecular size and structure, scintillation molecules could nonetheless be dispersed throughout a suitable bulk polymer medium such that their mean inter-molecular sizing approximately matched the mean chord of the DNA helix.

Their physical construction would also differ significantly from the conventional scintillation detectors. Watt *et al.* (1995) suggest a thin film scintillator of thickness no greater than 20μm, although scintillators of just a few microns would be more suited. By reducing thickness such that it is less than the mean track length of the incident primary radiation, the scintillator no longer acts as an energy deposition detector, but instead becomes sensitive to the instantaneous mean free path of the

radiation. If the film thickness is reduced further to around 6μm, it would approximately match the sensitive nuclear volume of a single mammalian cell. Such a dimension would significantly reduce the number of unwanted events.

In a radiation field, the detector would respond with the emission of scintillation photons, or scintons. Scintons would be emitted randomly from various sites within the phosphor, and the majority of events would be of no dosimetric value. Events of particular interest would be plural events: paired spatially-correlated photons emitted from adjacent fluor sites spaced at the requisite 2 nm. By modelling the effects of radiation interactions in the detector, a statistical relationship can be constructed allowing these events to be distinguished from other non-spatially correlated events. The resultant number of spatially correlated plural events would be proportional to the number of DNA double strand breaks induced by the same radiation field, and would therefore provide the absolute biological effectiveness of the radiation.

Collection of these single and multiple scinton events has only recently been made possible with the introduction of the Hybrid Photo Diode, manufactured by Delft Electronische Producten in the Netherlands.

2.2 Chemistry of Organic Scintillators

Ever since Rutherford and Marsden first used a zinc sulphide coated screen to detect α-particle scattering in 1908, both organic and inorganic scintillating molecules have become increasing prevalent in radiation detection.

The process by which a scintillation photon, or scinton, is emitted from an organic scintillation molecule is known as fluorescence and is a characteristic feature of delocalised electrons associated with the unsaturated carbon-carbon double bonds

which are manifest in all aromatic molecules. In these molecules, as with any unsaturated cyclic or straight chain organic molecule, only two or three of the four valence electrons of carbon associated with the double bond are used in chemical bonding and are strongly localised in s orbitals which lie between adjacent atoms in the molecule. The remaining one or two valance electrons are essentially delocalised within the molecule and populate π orbitals which extend in symmetrical lobes above and below each carbon atom of the double bond. The length of the carbon-carbon double bond, approximately 0.14 nm, is short enough to allow interactions between adjacent π orbitals. These interactions lead to the combining of similar spin polarised orbitals to produce two elongated areas of high delocalised electron concentrations above and below not only the carbon atoms producing the double bond, but also along the length of the double bond itself (Fessenden *et al* 1986).

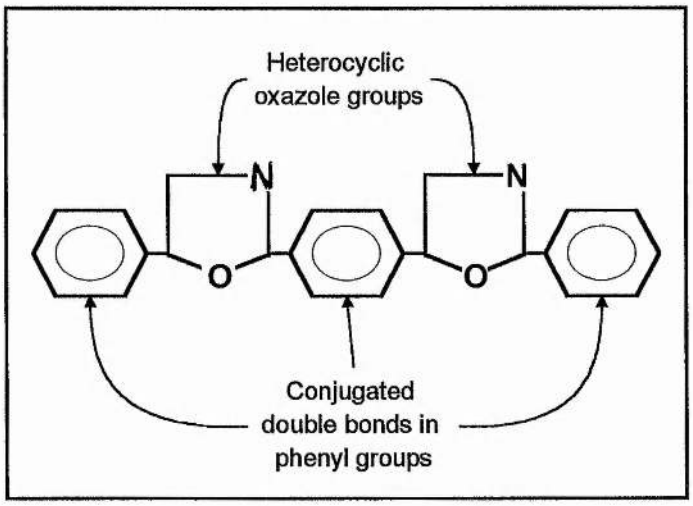

Figure 2.1 Illustration of the positions of conjugated carbon-carbon double bonds within the phenyl groups of the POPOP (1,4-(bis-{2-(5-phenyloxazolyl)}-benzene)) molecule (Brooks, 1979).

In aromatic compounds, which by definition are of a cyclic molecular structure, the alternate single and double bond arrangement, or conjugate double bonds, provide higher than usual localised concentrations of occupied π orbitals along the circumference of the molecule. These orbitals interact in exactly the same way as orbitals in straight chain molecules. However, because of the cyclic structure of the molecule, the π orbitals interact to form two annular electron clouds which lie in parallel planes above and below the conjugated double bond region.

The excitation potentials of individual electronic states in the π orbitals are directly associated with the number of double bonds present in the molecule. As the number of double bonds increase, the energy required for excitation is decreased.

2.3 Organic Scintillation Processes

The internal processes in organic scintillator molecules which lead to the emission of photons are comprised of two main mechanisms. The *prompt* emission, or fluorescence, is an almost instantaneous response to high energy photon, primary ion and δ ray interactions, with photons, or scintons, being emitted within several tens of nanoseconds after the interaction (Brooks 1979). The second process, known collectively as the *delayed* emission, is much weaker in intensity than prompt emissions (Brooks 1979) and is the combined effect of two decay processes: the *delayed emission* and *delayed fluorescence*. The true delayed component results from the decay of the triplet T_1 states to the S_0 ground state. The second delayed component, or delayed fluorescence, results from the S_1 to S_0 decay, with the S_1 state having been populated by the thermal activation of the lower energy T_1 triplet state. *(See figure 2.2)*

These decay processes are generally preceded by a short delay which arises from the transfer of energy from solvent to solute. It is assumed that incident high energy particles mainly excite solvent molecules as they make up the greater bulk of the scintillator. This energy is then transferred to the solute after a short decay time (Kallmann *et al,* 1957).

2.3.1 Prompt Emission

Prompt fluorescent emissions from a scintillation molecule occur in areas of low to average excitation density, areas which are produced by fast high energy particles depositing energies less than the ionisation potential of the scintillator molecule through electromagnetic interactions. The process leading to the emission of a photon involves the excitation of electrons in ground state π orbitals to their excited singlet S_n states. Generally, excited electrons will populate the vibrational substates of the S_2 and S_3 singlet states as these states have the largest transitional moments from the S_0 ground state (Birks 1964).

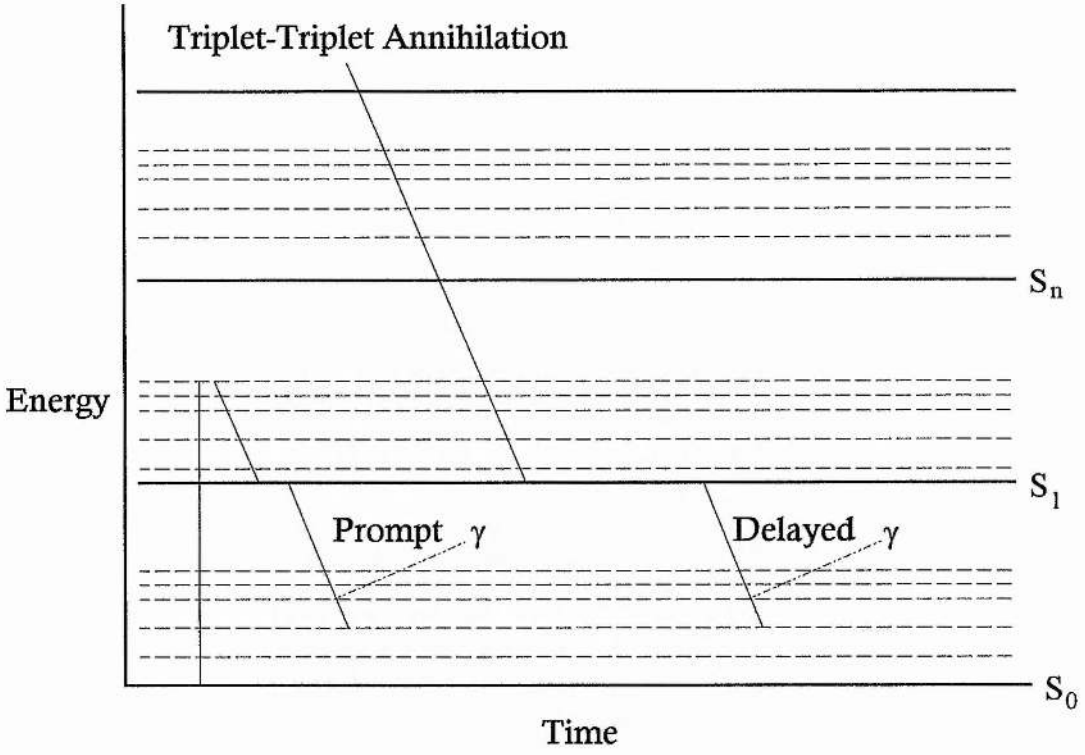

Figure 2.2 Schematic representation of prompt and delayed photon emissions in organic scintillation molecules.

These high energy states are highly unstable and rapidly decay to the lowest vibrational substate of the excited S_1 state in the order of 10^{-11} seconds. This de-excitation of the S_n states is highly efficient and follows a non-radiative path, with energy being expended as heat and through phonon coupling to the vibrational energy states of the entire molecule (Brooks 1979). The S_1 state is several orders of magnitude more stable than the S_n states, and decays exponentially in a time characteristic of the specific scintillator molecule, normally in the order of 1 to 80 nanoseconds. The subsequent S_1 - S_0 decay route exhibits a high radiative branching probability, and it is this decay that is responsible for the principle light output from the scintillator molecule (Brooks 1979). The S_1 - S_0 decay is typically only 3eV giving the characteristic blue light.

Although each singlet state is quantised into a discreet energy level, each state, including the S_0 state, possesses multiple vibrational substates existing at slightly higher energies, allowing for non-monoenergetic decays. The S_1 - S_0 decay does not always decay to the lowest vibrational energy state of the S_0 state, but rather may decay to a higher vibrational state with the emission of a photon of the corresponding energy (Brooks 1979). This property of the S_1 - S_0 decay produces a broadband output energy spectrum, rather than a single monochromatic wavelength, and as the emitted photon is rarely of an energy equivalent to the S_1 excitation energy, it is therefore unlikely to be re-absorbed through singlet photon absorption. This latter property ensures that emitted photons are transmitted through the scintillator with extremely high efficiency, as the material appears essentially transparent to the photon.

2.3.2 Population of S_1 State

Delocalised ground state electrons in π orbitals can be promoted into excited S_n states by various interactions. These highly excited states will then decay to populate the S_1 state, the decay of which gives rise to the prompt fluorescence component. The S_1 population mechanisms outlined below all lead to the production of prompt fluorescence and do not include the S_1 population mechanisms that lead to delayed fluorescence.

2.3.2.1 Incident Ions

The passage of a charged particle through the scintillation medium can promote de-localised electrons in the S_0 ground state into the higher S_n states by imparting energy onto the electron through electromagnetic interactions. The energy transferred onto the electron will depend upon the kinetics of the interaction, however two possible situations will result. An electron with energy less than the ionisation potential of the scintillation molecule will be termed excited and will remain bound within the molecule. This process leads directly to the population of the S_n states. In the case of electrons possessing energy greater than the ionisation potential of the molecule, they will be ejected and become free-travelling δ-rays. This latter process will not lead to the direct population of the S_n states of the source molecule, but may lead to S_n population in other neighbouring molecules. The population of triplet states from the S_0 is spin-forbidden.

2.3.2.2 δ Rays

Free-travelling δ-rays that are sufficiently energetic to reach neighbouring scintillation molecules can induce the population of S_n singlet states through electron-electron interactions with bound S_0 electrons in the adjacent molecule. If the energy exchanged in these interactions exceeds the ionisation potential of the scintillation molecule, further δ-rays will be produced.

2.3.2.3 High Energy Photons

Energy absorbed by S_n ground state electrons from high energy photons produced during ion recombination can lead to further population of excited S_n states.

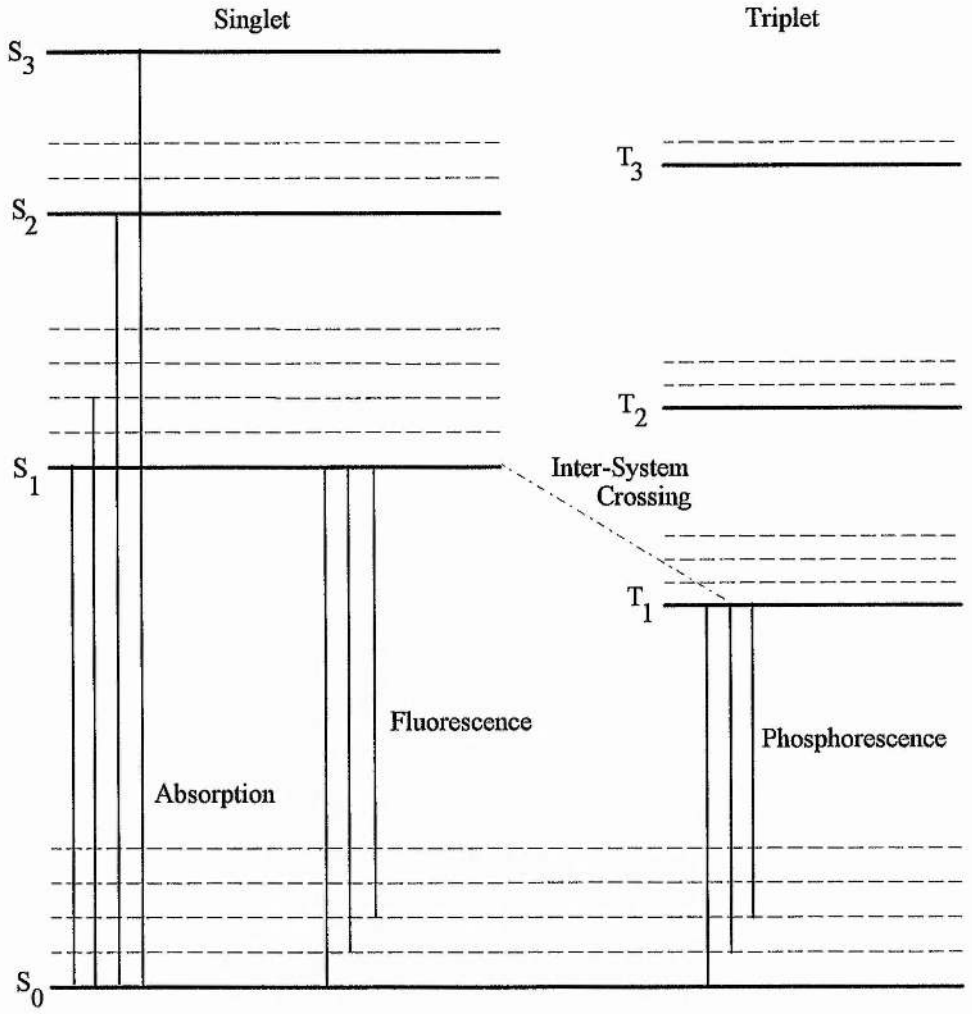

Figure 2.3 Energy levels of an organic molecule with π-electron structure (Birks, 1964).

2.4 Delayed Emissions

Delayed photon emissions from scintillator molecules form the second of the scintillation processes (Birks 1964). These emissions result from two distinctive decay routes; the *Delayed Component* or *Phosphorescence* which involves the T_1 -

2.4.1 Delayed Component

The delayed component, known as phosphorescence, results from the decay of the metastable T_1 triplet state which has a mean lifetime of 10^{-4} seconds depending on the scintillator (Birks 1964). T_n triplet states are populated from the corresponding S_n singlet state by intersystem crossing which involves spin reversal of the S_n electron through spin-orbit coupling (Birks 1964). This process allows the S_n singlet state to cross to the T_n triplet state by non-radiative conversion. Excited T_n triplet states decay rapidly and non-radiatively to the lowest vibrational substate of the T_1 triplet state with the same high efficiency as the S_n - S_1 singlet state decay (Brooks 1979). Direct T_n decay to the S_0 ground state is strongly forbidden (Brooks 1979).

The delayed phosphorescent emission that results is due to the decay of the relatively stable T_1 triplet state to a vibrational substate of the S_0 ground state. As each triplet state lies lower in energy than the corresponding singlet state, photons from this decay are observed as having a longer wavelength. Phosphorescence is readily observed in rigid solutions at low temperatures when non-radiative quenching to the S_0 ground state is inhibited. The intensity of these emissions is weaker than that of prompt fluorescence (Brooks 1979) and they decay exponentially with a longer time constant (Birks 1964).

2.4.2 Delayed Fluorescence

The second delayed emission, known as delayed fluorescence, results from the decay of the S_1 singlet state to a vibrational substate of the S_0 ground state. Although possessing the same emission spectrum as the prompt fluorescence emission (Birks 1964), this decay route differs from prompt fluorescence as the excited S_1 state is populated from the lower energy T_1 metastable triplet state.

The excited T_1 metastable triplet state is originally populated from an excited S_n state by intersystem crossing to the corresponding excited T_n state and then by internal non-radiative conversion of excess excitation energy. Although the predominant decay route from the T_1 state is directly to a vibrational substate of the S_0 ground state leading to phosphorescence, under favourable thermal energy conditions, the delayed fluorescence process can compete with this decay. Electrons in the excited T_1 state can acquire enough additional energy through thermal activation to make the non-radiative conversion back to the excited S_1 state (Birks 1964). The repopulated S_1 state then decays radiatively to a vibrational substate of the S_0 ground state, emitting the characteristic delayed fluorescence emission. The decay period of the S_1 state is lengthened by this process to approximately 10^{-6} seconds or longer (Birks 1964), and is related to the S_1 - T_1 energy difference, the lifetime of the metastable T_1 state and the temperature. It is assumed that the metastable T_1 state is not the only triplet state that can undergo a thermally activated non-radiative conversion back an excited S_n state (Birks 1964), however this conversion will be prohibited if the available thermal activation energy is less than the S_n - T_n energy difference.

2.5 Population of T_1 State

Population of the T_1 triplet state occurs by two main routes (Birks 1964).

2.5.1 Ion Recombination

Free-travelling δ-rays that have lost the bulk of their kinetic energy through extramolecular interactions are primarily responsible for the population of triplet states by the process of ion recombination (Voltz *et al.* 1966). Primary ion, δ ray and high energy photon interactions which impart energies greater than the molecular ionisation potential will cause bound π orbital electrons to be completely removed from the scintillator molecule leaving the molecule as an ion. Through the Coulomb force, both the positively charged scintillator ion and the negatively charged electron will recombine to re-establish charge equilibrium when δ-ray energy conditions favour. The process of ion recombination is primarily responsible for the population of excited T_n triplet states.

2.5.2 Intersystem Crossing

Intersystem crossing leads to the population of the T_n triplet states. This population mechanism leads primarily to the main delayed component, phosphorescence. However in the presence of sufficient thermal activation energy, the process can be reversed such that excited T_n states can repopulate the original excited S_n states, producing delayed fluorescence.

2.6 Exciton Interactions

The exciton model of energy transfer was originally proposed to explain the migration of excited electrons, or excitation waves, through the lattice structures of organic crystals (Hall, 1962 and Fowler, 1964). Thought of as being unique to organic crystal lattices, the exciton model can also be used to describe the migration of deposited energy, in the form of excited *bound* electrons, through organic plastic and liquid phosphors.

Exciton interactions play an important role in the transfer of energy between bulk host and scintillation molecules. The diffusion and interaction of these excitons within the centre track core and outside of this region lead to the population of lower energy states that will undergo radiative decay.

The exciton-exciton interaction which leads to the population of excited singlet states is triplet-triplet annihilation. Two excitons in excited T_1 states interact in a triplet-triplet annihilation to form an excited S_1 singlet state, a S_0 singlet ground state and phonons (Brooks 1979). The T_1 exciton is a relatively stable entity, and will migrate through the scintillator until it annihilates itself on interaction with another exciton. The length of time by which this scintillation emission is delayed is dependent on the kinetics of the exciton and the mean length of its migration.

2.7 Ionisation Saturation

Ionisation saturation or quenching as it is generally described, occurs in regions of the track core where high specific ionisation and excitation density are present and affects all organic scintillators. Such densities are produced by ions with high dE/dx, characteristics of heavy or slow ions. In these areas, the increased ionisation

produced by high *dE/dx* ions ionises most if not all the potential fluor centres, thus reducing the possible number of photons that may be emitted. Deposited energy is effectively wasted on ionising molecules that are already ionised, with no additional light output being produced. Saturation mainly affects the fast scintillation component, with much less effect on the delayed component (Birks 1964).

2.8 Scintillation Models

Ever since organic molecules were first used to detect ionising radiations by virtue of their ability to scintillate, no one theory has managed to explain fully or predict the outcome of every single experiment. To this end, several comparable models have been suggested by researchers in this field, notably Birks (1951), Chou (1952), Wright (1953) and more recently Blanc (1962) and Voltz *et al.* (1966). For the most part, these models were based on or verified by observed light responses produced by electrons, protons, deuterons, tritons and α-particles. However, the scarcity of high energy heavy ion accelerators in the 1950's precluded any studies to be made with heavy ions, generally considered to have A>4. From light response data produced by heavy ions (Becchetti *et al.*, 1976) many of these models became inadequate in their explanations and predictions at higher energies.

In order that a model may satisfactorily explain scintillation behaviour in a given radiation field, several primary physical characteristics of ion interactions with matter and scintillation response must be embodied in its final design. Energy deposition, *dE/dx*, the energy that is deposited by the primary ion in the scintillation medium per unit track length, is assumed by all researchers to be the primary parameter that gives rise to light output. The luminescent response of organic scintillators, *L(E)*, is a

non-linear function of the incident ion's kinetic energy and exhibits an inverse proportionality to the ion's mass (Birks 1951). This latter characteristic means that as an incident ion's mass increases for the same ion kinetic energy, the specific luminescent response is reduced. The importance of ion mass is further indicated in experiments using various isotopes of the same element. In such a case (Becchetti *et al.* 1976), the least massive isotope will produce a larger response for the same energy.

It is the objective of all scintillation models to explain light output in terms of the specific luminescence, dL/dx. This parameter, expressed as the light output per unit track length, is directly proportional to the number of scintillation events within a unit track length. It is assumed that this value will include the individual contributions of the prompt component and both delayed components, and at a fundamental level, will be a precise measure of the number of radiative decays per unit track length.

Data on the light output produced by heavy ions is very scarce, with only a few researchers publishing data for $^{14}N^{+}$ and $^{16}O^{+}$ (Becchetti *et al.*, 1976), $^{12}C^{+}$, $^{16}O^{+}$, $^{32}S^{+}$, $^{40}Ca^{2+}$ and $^{81}Br^{+}$ (Becchetti *et al.*, 1976), $^{16}O^{+}$, $^{35,37}Cl^{+}$, $^{40}Ar^{+}$, $^{79,80}Br^{+}$ and $^{127}I^{+}$ (Muga *et al.*, 1973), and $^{14}N^{+}$ and $^{16}O^{+}$ (Muga *et al.*, 1973), though nothing heavier. Generally, extensive data is available for electrons, protons, deuterons and α-particles produced by many researchers, and it is on these results that many of the current scintillation theories are based.

2.8.1 Birks Model

The pioneering Birks model (Birks 1951), which forms the basis of many later organic scintillation models, describes energy deposition in the form of ion linear energy transfer, LET, as the main mechanism leading to the induction of light output or fluorescence. Electronic excitation energy induced by incident particles is transferred from molecule to molecule in the form of an exciton. Light output arises from the capture of the exciton by a single molecule. In this model, which is confined to the behaviour of unitary organic phosphors, no distinction is made between prompt singlet decay and the delayed singlet and triplet decay emissions. For the simplest charged particle, the electron, which interacted with matter through excitation and ionisation processes along its random-walk path, specific fluorescence, dL/dx, appears linear and is described as being proportional to LET, thus

$$\frac{dL}{dx} = S\frac{dE}{dx} \qquad (2.1)$$

where S is the absolute scintillation efficiency and describes the scintillator's effectiveness at converting deposited energy into a fluorescent output, a figure typically quoted as only 4% for electrons (Birks 1964). Birks also notes that S is not constant but depends on the type and energy of the incident radiation. The electron's remaining energy is lost by collisions with other electrons and nuclei and as heat.

Equation (2.1) is based upon observed light output produced by fast (1 MeV) electrons in an anthracene crystal creating a low specific ionisation and excitation density along the primary track core, and its predictions closely agree with experimental data (electrons with energies in the range 125 keV to 3 MeV and

electrons and μ-mesons up to 170 MeV). However, when this simple model is applied to heavier ions, such as protons, deuterons, tritons and α-particles, the phenomenon described by Birks (1964) as ionisation quenching, or more commonly known as saturation, occurs and equation (2.1) becomes invalid.

Saturation is present in regions of high specific ionisation and excitation density such as those produced by high *dE/dx* ions (slow or heavy ions), and has the effect of reducing the overall efficiency of scintillation which can otherwise be seen as being proportional to the ion's mass and kinetic energy (Birks 1964). This in part explains the behaviour of degraded light outputs produced by increasingly heavier isotopes of the same element at similar energies. Birks describes the effects of ionisation quenching as being caused by the presence of quenching centres; scintillation molecules with fractured molecular bonds induced by irradiation. Damaged molecules promote a non-radiative decay route leading to de-excitation without the production of scintillation quanta, thus reducing specific scintillation efficiency. To overcome the effects of ionisation quenching, Birks (1951) proposed

$$\frac{dL}{dx} = \frac{S.\frac{dE}{dx}}{\left(1 + kB.\frac{dE}{dx}\right)} \qquad (2.2)$$

where k is the quenching parameter (related to the relative exciton capture cross-section of a damaged molecule to that of an undamaged molecule) and B is a constant such that $B.dE/dx$ is the specific ionisation and excitation density along the track core.

While this model offers good agreement with light production data from electrons and light ions in organic crystals and begins to explain the causes of photon

yield degradation in high excitation and ionisation densities, it generally underestimates the effects of ionisation saturation when using heavy ions (A > 4). This shortfall leads to the model predicting a higher specific scintillation efficiency for high *dE/dx* ions than is actually observed. The assumption is made that at high *dE/dx*, equation (2.2) reduces to $dL/dx = A/kB$, which is constant, implying a linear response. Investigations by Newman *et al.* (1961) with light output data from heavy ions ($^{4}He^{2+}$, $^{14}N^{+}$ and $^{16}O^{+}$) revealed that this model is inadequate at describing the fluorescent response of lightly ionising particles, and indicates that light production is more than just a function of specific energy loss. In the case of $^{14}N^{+}$ and $^{16}O^{+}$ data, specific scintillation efficiency has to be reduced by a factor of approximately 5 before any correlation can be made.

2.8.2 Chou Model

The Chou (1952) model is based very closely on the original Birks model, but has received little attention. The model introduces an additional quadratic denominator to give the relationship

$$\frac{dL}{dx} = \frac{S\frac{dE}{dx}}{\left[\left(1 + kB\frac{dE}{dx}\right) + \left(C.\frac{dE}{dx}\right)^{2}\right]} \qquad (2.3)$$

where B and C are constants. Birks (1964) comments that this model is only valid when C = 0, and therefore equation (2.3) becomes equation (2.2).

2.8.3 Wright Model

The Wright model (Wright, 1953) supports Birks' (1951) proposal that organic scintillator efficiencies and decay times are not constant characteristics of the detector, but rather depend on the nature and energy of the absorbed radiation.

In agreement with Birks (1951), this model describes the effects of ionisation quenching, or saturation, as being the predominant cause of the low values of specific scintillation efficiency observed in experiments. It is also noted that the use of heavily ionising particles, such as slow or heavy ions, cause a further reduction in specific scintillation efficiency due to increased localised saturation, and that a slight decrease in decay time may also be observed. These effects are ascribed to the additional influence of bimolecular quenching between neighbouring excited or ionised molecules, which can promote non-radiative decay routes to the S_0 ground state. Quenching of fluorescence, the phenomenon of reduced scintillation efficiency observed with high LET ions, is described as being related to both monomolecular and bimolecular processes in the centre track core or excitation column.

Using this model, scintillation output is calculated in terms of the total energy deposition of an ion penetrating a distance Δx in the scintillation medium. The excitation column surrounding the primary ion track, of length Δx, will contain excess energy corresponding to $dE/dx.\ \Delta x$. At time t after absorption of the ion the excess energy produced by ionisation and excitation is

$$d\varepsilon = -(p + k + a\varepsilon)\varepsilon.dt \qquad (2.4)$$

where aε is the rate of energy dissipation by bimolecular processes, k is the rate of energy dissipation by monomolecular processes and p is the rate of energy dissipation due to fluorescence emission. This excess molecular energy, $d\varepsilon$, in the form of both excited and ionised molecules, gives rise to a total light output per unit track length

$$\frac{dL}{dx} = p\int_0^{\infty} \varepsilon . dL = \frac{p}{a} \ln\left(1 + \frac{a}{p} + k.\frac{dE}{dx}\right) \qquad (2.5)$$

When dE/dx is small, equation (2.5) becomes

$$\frac{dL}{dx} = \frac{\frac{p}{p+k}.\frac{dE}{dx}}{\left(1 + \frac{1}{2}.\frac{a}{p+k}.\frac{dE}{dx}\right)} \qquad (2.6)$$

Equation (2.6) is in close agreement with the semi-empirical model proposed by Birks (1951), where $p/(p+k)$ is the specific scintillation efficiency and $½.a/(p+k)$ is the product of quenching and excitation and ionisation densities per unit track length.

This model shows good agreement with observed light curves for protons, deuterons and α-particles with energies up to 15 MeV obtained by Wright (1953). From the results of these experiments Wright makes the observation that the decay time of fluorescence is longer when the scintillation molecule is excited by ionising radiation than it is when excited by UV radiation. This observation is interpreted as being due to additional photon absorption and emission processes caused by the

presence of ionised molecules (Birks 1951). Additionally, Wright interprets this delay in terms of the finite time taken for ion recombination to take place.

The application of this model to data obtained by Brooks (1956) indicates that equation (2.6) agrees closely with light responses for electrons of energy between 0.2 and 10 MeV, protons of energy between 2 and 15 MeV and α-particles of energy between 5 and 20 MeV. At energies below these ranges, this model underestimates light responses observed in experiments, while above these values, this model overestimates light output and fails to account for the effects of saturation.

This model is criticised by Voltz *et al.* (1966) as being similar to the Birks model (1951) in its inability to predict the onset of ionisation saturation for high LET ions. Similarly, this model does not make reference to the individual effects of prompt and delayed phosphorescent and fluorescence components, nor to the direct effects of δ-rays and secondary ionisation.

2.8.4 Blanc Model

The Blanc *et al.* (1962) model is based upon the diffusion of excitons from the centre track core and describes the effects of ionisation quenching in terms of exciton capture. Generally, ionising particles are considered to excite dN molecules, subsequently described as excitons, into the S_1 singlet state within a unit track length, dr. These excitons diffuse radially from the track core, undergoing one of two possible interactions. Firstly, they may non-radiatively de-excite through a damaged molecule acting as a quenching centre, or may de-excite radiatively with the emission of a scintillation quantum. Exciton density at a point M at a distance r from the centre track core at time t is given by

$$\frac{\partial n}{\partial t} = D\nabla^2 n - f(r,t).n - g(r,t).n^2 - \sum_{=3}^{\infty} h_j(r,t).n^j + R(r,t) \qquad (2.7)$$

where D is the exciton diffusion coefficient, f, gn and $h_j.n^{j-1}$ are the probabilities of uni-, bi-, and j-molecular de-excitation, and R(r,t) is the number of fluorescence photons absorbed per second per unit volume around M. Blanc *et al.* (1962) simplified this equation by neglecting j-molecular de-excitation to

$$\frac{\partial n}{\partial t} = D\nabla^2 n - (p+q).n - a.n^2 + R(r,t) \qquad (2.8)$$

The solution of equation (2.8), dN/dr, is the total number of excitons per unit track length at time, t, expressed relative to the initial number of excitons produced.

Few data are available from researchers who have used this model, however Birks (1964) indicates that this model reaffirms the success of Birks' own model (1951) in empirical calculations.

2.8.5 Voltz Model

Voltz *et al.* (1966) proposed that overall scintillation output should be described in terms of z, the ionic charge, and dE/dx, the ion LET, and for the first time makes a distinction between the individual contributions of the prompt and delay components as well as the effects of δ-rays. This approach differs significantly from previous treatments which describe light output in terms of the combined effects of both components.

Voltz *et al.* define scintillation output as being proportional to the number of electrons in singlet and triplet states per unit track length. Triplet states produced during ion recombination are assumed to annihilate in triplet-triplet interactions to form additional excited singlet states. The light output produced by the de-excitation of the S_1 singlet state, producing the prompt component, is defined as

$$\frac{dL}{dx} = \eta \frac{dN_s}{dx} \qquad (2.9)$$

where η is the quantum efficiency of fluorescence and dN_S/dx is the number of excited electrons in the S_1 singlet state per unit track length. Voltz *et al.* note that dN_S/dx is again related to the nature of the incident particle, and that it is reduced by quenching effects caused by interactions between the highly excited S_n singlet states. This effect introduces alternate non-radiative de-excitation routes to the S_0 ground state thus reducing the overall efficiency of fluorescence.

The delayed light output resulting from the de-excitation of S_1 singlet states produced by T_1 triplet-triplet annihilations is defined as

$$\frac{dL'}{dx} = \eta\alpha \frac{dN_T}{dx} \qquad (2.10)$$

where η is the quantum efficiency of fluorescence, α is the number of S_1 singlet states produced by a triplet-triplet annihilation and dN_T/dx is the number of excited electrons in the T_1 triplet state per unit track length.

The combined light output of both prompt and delayed decays can be defined as the sum contribution of both components

$$\frac{dS}{dx} = \frac{dL}{dx} + \frac{dL'}{dx} \qquad (2.11)$$

The specific luminescence, *dS/dx*, is therefore a measure of the total number of photons emitted per unit track length.

By incorporating expressions for excited singlet and triplet state decays, effects of secondary excitations and ionisations (δ-rays), and the kinetics of quenching centres, Voltz *et al.* developed a model that is in very close agreement with experimental results and successfully predicts the onset of saturation and the observed reduction in specific scintillation efficiency.

2.9 A New Approach to Dosimetry

A fundamental need of current models for assessing radiation dose and risk factors is that they require a foreknowledge of radiation type. Such a knowledge is required in order that the correct quality or scaling factor may be applied to the measured absorbed dose to obtain the dose equivalent in tissue. Using absorbed dose alone, we find that high LET particles produce greater biological damage than low LET radiations, such as electrons, even though both particles deposit the same total energy per unit mass.

The introduction of the quality factor, Q, corrects this anomaly by ascribing differing damage potentials to different radiation types, such that the dose equivalent, H, is given by

$$H=DQ \qquad (2.12)$$

where D is the absorbed dose.

In chapter 1, however, it was shown that LET-based models do not provide adequate correlation between energy deposition and subsequent radiation damage. Fundamental to the LET system of dosimetry is the concept that cell inactivation probability or killing power of a radiation is proportional to energy transfer. As LET increases, the yield of primary ionisations, or δ-rays, also increases. Delta-rays are created during the interactions of primary radiations with the absorbing medium. Energy is transferred from the incident radiation onto bound molecular electrons causing them to be ejected from their orbits, producing an ionised molecule and a high energy free electron, or δ-ray. These δ-rays radiate outwards from the central track creating an envelope of dense ionisation and it is assumed that they add to the overall biological effectiveness of the radiation.

In order to obtain a better understanding of the biological damage induced by irradiation, it is necessary to approach dosimetry and the effects of radiation action from a radically new standpoint. It is accepted that although increasing radiation damage may appear proportional to LET, damage can more accurately be described in terms of the damage caused to the intranuclear DNA. More specifically, a number of biological endpoints, including oncogenic transformations, chromosomal aberrations and cell inactivation, can be directly related to the yield of double strand

breaks in mammalian DNA (Watt, 1997). It follows that if a detector could be designed to simulate the same response as DNA, then that device would be capable of measuring the absolute biological effectiveness (Watt, 1989). By virtue of its close analogy to DNA, no foreknowledge of radiation type would be required, and quality factors could be ignored. In 1995, Watt *et al.* proposed a theoretical model for such a detector.

In seeking a suitable device that would meet all the stringent criteria of an absolute dosimeter, Watt *et al.* (1995) identified organic scintillators as being of particular interest. These poly-cyclic aromatic scintillation molecules have been commercially produced in various concentrations and in various solvents to produce sensitive radiation detectors which respond to irradiation by the emission of a photon of light. Scintillators have an efficiency of light output which is modified by saturation effects to an extent dependent of particle type. Mammalian cells have radiosensitivities which show a similar trend for saturation effects dependent on radiation type.

In the scintillator, energy is absorbed by the bulk polymer with the production of excitons. These excitons then diffuse through the bulk material until trapped by a fluor site, where a scinton, or scintillation photon is emitted. Each scinton emission can be considered as an indicator.

In this model, photon yield is established by calculation of the primary electron spectrum and the associated equilibrium electron spectrum in the irradiated material. The concentration of excitons, $C_x(E)$, calculated from the equilibrium electron spectrum, is given by

$$C_x(E) = \varphi_{eq}(E)\, I(E) \qquad (2.13)$$

where $\varphi_{eq}(E)$ is the differential fluence spectrum of equilibrium electrons per unit source concentration of generated electrons. $I(E)$ is the linear primary ionisation of the electrons.

The mean number of active centres at risk, $N_r(E)$, is given by

$$N_r(E)\Delta E = \frac{\varphi_{eq}(E)\Delta E}{x_a} \qquad (2.14)$$

where x_a is the mean distance between active centres, and is determined from the concentration of fluor molecules in the phosphor.

Numerical integration of equation 2.14 over the equilibrium spectrum gives the total number of active centres at risk of interaction, given by

$$N_{T,a} = \sum_j N_r(E_j)\Delta E_j = \frac{\sum_j \varphi_{eq}(E_j)\Delta E_j}{x_a} \qquad (2.15)$$

The total number of at-risk sites, $N_{T,a}$, with further manipulation, leads to the absolute photon yield of the phosphor. This model has yet to be tested with heavy ions. Good correlation has however been obtained from phosphors irradiated with γ-rays and it has specific applications in nanodosimetry.

2.9.1 Exciton Migration

The exciton model of energy migration in an organic crystalline lattice (Birks *et al.*, 1951, Hall, 1962) is used to explain the mechanism by which charge-carriers can undergo inter-molecular migration. Excitons are generally produced by the absorption of a photon leading to molecular excitation. The resulting excitation may then undergo intra- and inter-molecular migration (Choi *et al.*, 1963) before being annihilated by another exciton or trapped by an impurity.

In the plastic scintillator, the vast majority of primary radiation interactions occur in the polymerised bulk solvent, polyvinyl toluene (PVT). A weak yield of scintons is produced by irradiation of PVT, but the solvent almost exclusively absorbs excitation energy to produce excitons (Birks, 1964). The mean energy expended in the production of an exciton is ~10eV. PVT scintons are generally of short UV wavelengths, 340 nm (Birks, 1964), and are thus severely attenuated by UV absorption bands in the Perspex light-pipe. It is assumed that few PVT scintons reach the photocathode. A second route for PVT scintons is absorption by wave-shifting POPOP sites. The yield of such scintons is assumed to be negligible in comparison to the yield of exciton produced scintons.

The mean diffusion length of an exciton is limited by the mean distribution of impurities in non-scavenging conditions or scavenging exciton traps. These molecules, the scinton emitting POPOP molecules, have a mean distribution of approximately 5 nm. The probability that an exciton will interact with an active centre in the scintillator, P_a, is given by

$$P_a = 1 - \exp(-\sigma_{ex} . \Phi_{ex}) \qquad (2.16)$$

where Φ_{ex} is the fluence of excitons, and

σ_{ex} is the exciton activation cross-section.

As yet, there appears to be no published value for the latter, but it is estimated as $1 \times 10^{-18} cm^{-2}$.

2.9.1.1 Exciton Life-Time

The mean life-time of an exciton is related to the concentration of impurity molecules in the scintillator volume. These impurities act as exciton traps and thus reduce the exciton life time. In non-scavenging conditions, the mean life time of the exciton, $(\tau_{0x})_0$, is given as

$$(\tau_{0x})_0 = \frac{1}{k_{fx} + k_{ix}} \qquad (2.17)$$

where k_{fx} and k_{ix} are the rate parameters of fluorescence and internal quenching respectively.

2.9.2 Plastic Phosphor - NE102A

The plastic phosphor, NE102A, designed and manufactured by Nuclear Enterprises Ltd. (now Bicron NE), is a general purpose scintillator that is widely and successfully used in the detection of α, β, γ-rays, fast neutrons and protons (Nuclear Enterprises Ltd, 1995). As an organic polymer, it is capable of being manufactured in a variety

of shapes and thicknesses, and in its thin film form, of only 20μm thickness, is ideally suited for use in microdosimetry applications.

2.9.2.1 Composition of NE102A

The precise chemical composition for the manufacture of the plastic scintillator NE102A remains commercially sensitive. However, an approximated by-weight composition was released by Nuclear Enterprises Ltd. (1986) and from this data, the critical number of active fluor sites per unit volume, N, may be calculated:

$$N = \frac{\rho . P . N_A}{w_F} \qquad (2.18)$$

where ρ is the mean density of the scintillator, 1.032g.cm^{-3},

P is the percentage by-weight composition of each constituent molecule,

N_A is Avogadro's Number, 6.022 x 10^{23}, and

w_F is the formula weight of each molecule.

Table 2.1 Physical Data on NE102A

Name	Chemical Name	Formula	Formula Weight	Percentage Composition	Molecules cm^{-3}
PVT	Polyvinyl Toluene	$C_6H_4.CH_3.C_2H_3$	118g	96.975%	5.107 x 10^{21}
PT	*p*-Terphenyl	$C_{18}H_{14}$	230g	2.975%	8.039 x 10^{19}
POPOP	1,4-bis-2-5-phenyloxazolyl benzene	$C_{24}H_{16}N_2O_2$	364g	0.05%	8.537 x 10^{17}

2.9.3 Distribution of Fluor Sites

The spatial distribution of molecules in a given volume is dependent on the molecular concentration and when present in extremely high concentrations, on the mean physical and chemical dimensions of the molecule. This latter condition, which defines the minimum spacing of any two molecules, is often a qualifying factor associated with complete spatial randomness (CSR) exhibited by substances in the liquid phase.

If a known concentration of fluor molecules, C_a, are present in a known constant volume of constant average density, and are randomly and homogeneously distributed throughout the volume, then the mean spacing between fluor molecules, x_a, is given by

$$x_a = \Gamma(4/3).\left(\frac{3}{4\pi\, C_a}\right)^{\frac{1}{3}} \qquad (2.19)$$

where $\Gamma(x)$ is the Gamma function, and $\Gamma(4/3)$ is approximately 0.893.

Table 2.2 Molecular Distributions in NE102A

Molecule	Mean Molecular Spacing (nm)
PVT	0.32
PT	1.28
POPOP	5.84

2.9.4 Spatial Probability of Paired Fluor Sites

The mean spacing between POPOP fluor molecules, x_a, is characterised by the concentration of active centres per unit volume, which in NE102A is approximately 6

nm. However, in order to allow later extraction of the scinton yield from paired fluor sites with an intermolecular spacing of 2 nm, matching the mean chord of double stranded DNA in mammalian cells, it is necessary to calculate the number of paired sites that fit this condition.

The probability of two fluor sites at exactly a spacing of 2 nm is zero, however, the population distribution of mean, x_a, may be calculated. Using the Gamma Function or Gamma Distribution, the probability of the existence of paired active centres with an intermolecular spacing of $x \leq x_0$, is given by

$$P(x) = 1 - \exp\left\{-\left(\frac{x.\Gamma(4/3)}{x_a}\right)^3\right\} \qquad (2.20)$$

where x is the desired spacing range of 2 nm,

x_a is the mean spacing between molecules, and

$\Gamma(4/3)$ is the Gamma function, equal to 0.893.

Table 2.3 Spatial Distribution of Paired Fluor Sites using the Gamma Function

Spatial Window (nm)	Gamma Function P(x)
2 ± 0.0	0
2 ± 0.1	6.328e-5
2 ± 0.2	1.269e-4
2 ± 0.3	1.911e-4
2 ± 0.4	2.563e-4
2 ± 0.5	3.227e-4
2 ± 0.6	3.907e-4
2 ± 0.7	4.606e-4
2 ± 0.8	5.327e-4
2 ± 0.9	6.073e-4

2.9.5 Chemically Engineered ABE Scintillator

By altering the concentrations of individual molecular components in the NE102A plastic scintillator, the mean fluor distribution can be made to closely approximate the critical dimensions of double stranded DNA. While this approach was not investigated for suitability, the desired concentrations of solvent and solute molecules are presented here. The concentration of the POPOP molecule, as the primary source of scinton emissions, must be increased some 25 times to achieve the desired 2 nm spacing.

Table 2.4 Enhanced concentrations of NE102A for ABE dosimetry.

Name	Chemical Name	Formula	Formula Weight	Percentage Composition	Molecules cm^{-3}
PVT	Polyvinyl Toluene	$C_6H_4.CH_3.C_2H_3$	118g	94.05%	4.953×10^{21}
PT	*p*-Terphenyl	$C_{18}H_{14}$	230g	2.975%	8.039×10^{19}
POPOP	1,4-bis-2-5-phenyloxazolyl benzene	$C_{24}H_{16}N_2O_2$	364g	1.245%	2.125×10^{19}

2.10 Event Probabilities

From each recordable spectrum of single (k=1) and plural (k=2, 3, 4,..) scinton peaks and a detailed knowledge of the composition of the plastic scintillation detector, the application of a statistical model allows extraction of event probabilities. The probabilities of most interest are those of 'paired spatially correlated' events.

2.10.1 Activator Sites

Organic fluor sites are spread randomly and uniformly throughout the irradiated detection medium, and can spatially occur singly as a lone centre or doubly as a pair of close centres. If we consider a primary track of energy, E, incident on the detector, and assume the following definitions:

$N_T(E)$ is the expected number of all active centres at risk,

$N_2(E)$ is the expected total number of paired active centres at risk, and

$N_1(E)$ is the expected total number of single active centres at risk.

It then follows that

$$N_T(E) = N_1(E) + 2.N_2(E) \qquad (2.21)$$

and

$$N_2(E) = \tfrac{1}{2} P(2).N_T(E) \qquad (2.22)$$

so

$$N_1(E) = (1\text{-}P(2)).N_T(E) \qquad (2.23)$$

where $P(2)$ is the expected proportion of all fluor centres which lie within the 1-2 nm range. The probability that randomly paired molecules occur within the 1- 2 nm is given by

$$P(x) = 1 - \exp\left\{-\left(\frac{x.\Gamma(4/3)}{x_{fl}}\right)^3\right\} \qquad (2.24)$$

where x is the desired spacing range of 2 nm

x_{fl} is mean spacing between molecules at a given concentration.

$\Gamma(4/3)$ is the Gamma function, equal to 0.893

2.10.2 Scinton Emissions

Scinton emissions can be produced in two separate interactions: by the direct action of primary radiation on fluor sites; and by the indirect action of a diffusing exciton trapped by a fluor site.

Scinton emissions from the primary track are recorded as occurring singly, in twos, in threes, in fours, and so on. An individual scinton can arise from a single centre (or from half of a double centre); two scintons may arise from two separate single centres, or from a double centre. These, and further possibilities are given in the following table:

Table 2.5 Scinton emission combinations

number of scintons, k	*Number of single events*	*number of double events*
0	0	0
1	1	0
2	2	0
	0	1
3	3	0
	1	1
4	4	0
	2	1
	0	2
5	5	0
	3	1
	1	2

2.10.3 Single Scinton Condition

Single scinton events are defined as those events in which a primary ionisation or diffusing exciton stimulate a fluor centre resulting in the emission of single scinton. There are two possible interactions which can produce a single scinton event:

1. A primary ionisation or exciton stimulates a single spatially uncorrelated centre, and
2. A primary ionisation or exciton stimulates one half of a spatially correlated double centre.

In the case of direct interactions with primary radiation, the probability that primary radiation will interact with a single fluor centre, at least once, is

$$H(1,E) = 1 - \exp\left(-\frac{I}{2I_0}\right) \qquad (2.25)$$

where I is linear primary ionisation of the primary radiation, and

I_0 is the linear primary ionisation corresponding to $\lambda = 2$ nm.

In the case of the capture of a diffusing exciton, the probability that the exciton will interact with an active centre is

$$P_a = 1 - \exp(-\sigma_{ex}.\Phi_{ex}) \qquad (2.26)$$

where σ_{ex} is the exciton capture cross-section, and

Φ_{ex} is the exciton fluence

The net probability that a fluor centre will be stimulated by an exciton or by direct action of a primary radiation is

$$H_T(1,E) = 1 - \exp\left\{-\left(\sigma_{ex}.\Phi + \frac{I}{2I_0}\right)\right\} \qquad (2.27)$$

It then follows that the probability of stimulating a centre to produce a single scinton event is

$$P_a(E).H_T(1,E) \qquad (2.28)$$

where $H_T(1,E)$ is the net probability that a fluor centre will be 'hit,' and

$P_a(E)$ is the probability of stimulating a fluor centre, given by

$$P_a(E) = 1 - exp[-\varphi_x(E).\sigma_a(E)] \qquad (2.29)$$

where $\sigma_a(E)$ is the exciton production cross-section,

$\varphi_x(E)$ is fluence of excitons per unit source concentration, given by

$$\varphi_x(E) = C_x(E).\lambda_x \qquad (2.30)$$

where

$$C_x(E) = \varphi_{eq}(E).I(E) \qquad (2.31)$$

where $\varphi_{eq}(E)$ is differential fluence spectrum of equilibrium electrons per unit source concentration of generated electrons,

λ_x is the mean diffusion length for an exciton, and

$I(E)$ is the linear primary ionisation for the component electron track.

The probability, then, of a single scinton event being produced by one half of a spatially correlated pair of centres is

$$2.P_a(E).H_T(1,E).(1-P_a(E).H(1,E)) \qquad (2.32)$$

Taking both event probabilities into account, the expected total number of single scinton events produced in the detection medium is

$$N_T(E).P_a(E).H(1,E).(1-P(2).P_a(E).H(1,E)) \qquad (2.33)$$

where $P_a(E)$ is the probability of stimulating an active centre and $H(1,E)$ is the probability that the centre at risk is 'hit', i.e. there is at least one ionisation in the centre at risk.

The probability that an 'unpaired event' occur at a fluor centre is

$$P(1,E) = H_T(1,E).(1-P(2).H_T(1,E)) \qquad (2.34)$$

2.10.4 Double Scinton Condition

Double scinton events arise when an ionisation stimulates both centres of a paired centre. In the biological context, this is the equivalent of the double strand break in DNA. Its probability of occurrence is

$$(P_a(E).H(1,E))^2 \qquad (2.35)$$

and the expected total number of double scintons occurring, i.e., from double events, is

$$½.P(2).N_T(E).(P_a(E).H(1,E))^2 \qquad (2.36)$$

The probability that a spatially correlated 'paired event' (one hit simultaneously in each fluor centre spaced at 2 nm) will occur is

$$P(2,E) = \tfrac{1}{2}.P(2).(H_T(1,E))^2 \qquad (2.37)$$

Spatially uncorrelated 'paired events' such as those produced in time-coincidence at sites spaced greater than 2 nm apart are treated as two single events.

2.10.5 Theoretical Scinton Yields

The average number of single events per electron track is

$$N(1,E) = N_T(E).H_T(1,E).(1 - P(2).H_T(1,E)) \qquad (2.38)$$

Therefore, the probability of exactly k single events, analogous to single strand breaks in DNA, occurring is

$$P_1(k) = \frac{N(1,E)^k.\exp(-N(1,E))}{k!} \qquad (2.39)$$

The average number of spatially correlated 'paired events' is

$$N(2,E) = N_T(E).P(2).(H_T(1,E))^2 \qquad (2.40)$$

And therefore, the probability of exactly k paired events, analogous to double strand breaks in DNA, occurring is

$$P_2(k) = \frac{N(2,E)^k . \exp(-N(2,E))}{k!} \qquad (2.41)$$

2.11 Probability Theory

Let X be the number of 'double scinton' events and S be the number of 'single scinton' events arising from an experiment with the equilibrium distribution, ϕ_{eq}. Then, from equation 2.21, the total number of scintons, T, is

$$T = S + 2.X \qquad (2.42)$$

Given $T = k$, the probability that at least one paired event occurs is determined by $\Pr(X \geq 1 \mid T = k)$. This is equivalent to

$$\Pr(X \geq 1 \mid T = k) = 1 - \Pr(X=0 \mid T=k) \qquad (2.43)$$

where

$$\Pr(X = 0 \mid T = k) = \frac{\Pr(X = 0).\Pr(S = k)}{\Pr(T = k)} \quad k=0,1,2,.... \qquad (2.44)$$

Both distributions in S (single scintons) and X (double scintons) are assumed to be Poissonian with respective means given by

$$\mu_S(E) = N_T(E).P_a(E).H(1,E).(1 - P(2).P_a(E).H(1,E)) \qquad (2.45)$$

and

$$\mu_X(E) = \frac{1}{2}P(2).N_T(E).(P_a(E).H(1,E))^2 \qquad (2.46)$$

Averaging over the energy distribution yields the probability coefficients are then:

$$g_r = \Pr(X = r) = \int_0^\infty \frac{\mu_X(E)^r}{r!}\exp(-\mu_X(E)).\varphi_{eq}(E).dE \quad \text{r=0,1,2, 3,....} \quad (2.47)$$

and

$$h_S = \Pr(S = s) = \int_0^\infty \frac{\mu_S(E)^S}{s!}\exp(-\mu_S(E)).\varphi_{eq}(E).dE \quad \text{s=0,1,2, 3,....} \quad (2.48)$$

For particular values of r and s it may be possible to simplify the expressions. However, in general, numerical integration will have to be used to evaluate g_r and h_s for those values of r and s which are necessary in calculating $\Pr(T=k)$ and hence $\Pr(X>1 \mid T=k)$. Calculation of the probabilities $\Pr(T=k)$ and hence $\Pr(X \geq 1 \mid T = k)$ are obtained from the coefficients in g_r and h_s as follows

$$\Pr(T=k)=\sum_{r=0}^{k/2} g_r h_{k-2r} \qquad (2.49)$$

and

$$\Pr(X \geq 1 \mid T = k) = 1 - \frac{g_0 h_k}{\Pr(T=k)} \qquad (2.50)$$

The probability of paired spatially correlated events occurring in the k = zero and the k = 1 scinton peaks is clearly zero. For higher order peaks with each event due to exactly '*k*' scintons, the probabilities, from equation 2.43, are:

$$\Pr(X \geq 1 \mid T = 2) = \frac{g_1 h_0}{g_0 h_2 + g_1 h_0} \qquad (2.51)$$

$$\Pr(X \geq 1 \mid T = 3) = \frac{g_1 h_1}{g_0 h_3 + g_1 h_1} \qquad (2.52)$$

and

$$\Pr(X \geq 1 \mid T = 4) = \frac{g_1 h_2 + g_2 h_0}{g_0 h_4 + g_1 h_2 + g_2 h_0} \qquad (2.53)$$

2.12 Theoretical Nanoscintometric Spectra

Calculated theoretical spectra for isotopes ^{55}Fe, ^{60}Co, ^{137}Cs and ^{241}Am, obtained from the model described in Section 2.11 are presented on the following four pages. Each spectrum contains the expected number of 'k' scintons per channel per unit photon fluence as a function of channel, and the associated number of single and double strand breaks. An idealised plane of 10μm spheres of NE102A was used in the calculation, and no account was taken of scinton losses through escape, transmission inefficiencies of the phosphor, or interpeak contributions from adjacent peaks. These latter effects are likely to be important and must be evaluated for a practical device.

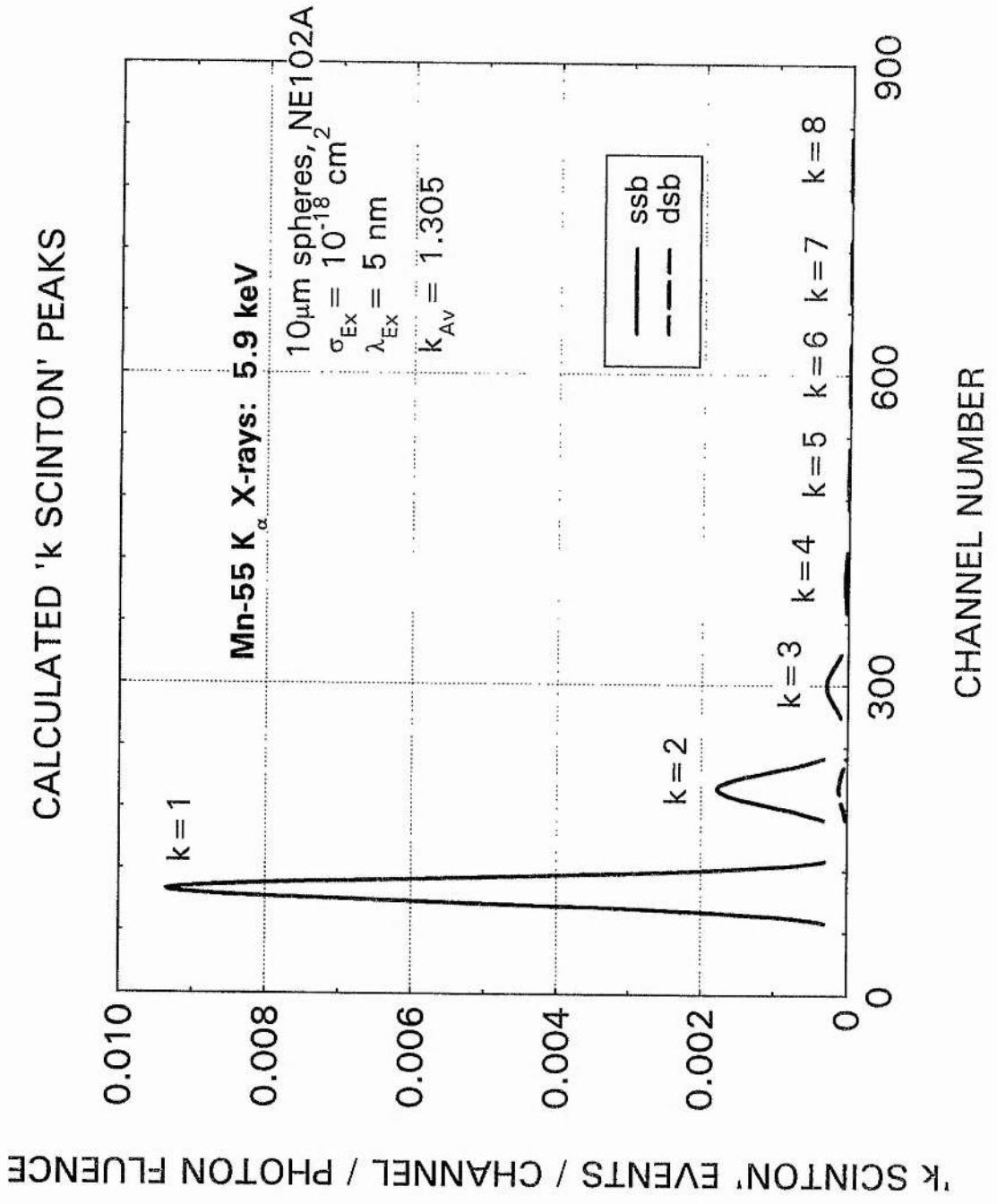

Figure 2.4 Theoretical scinton yield for iron-55

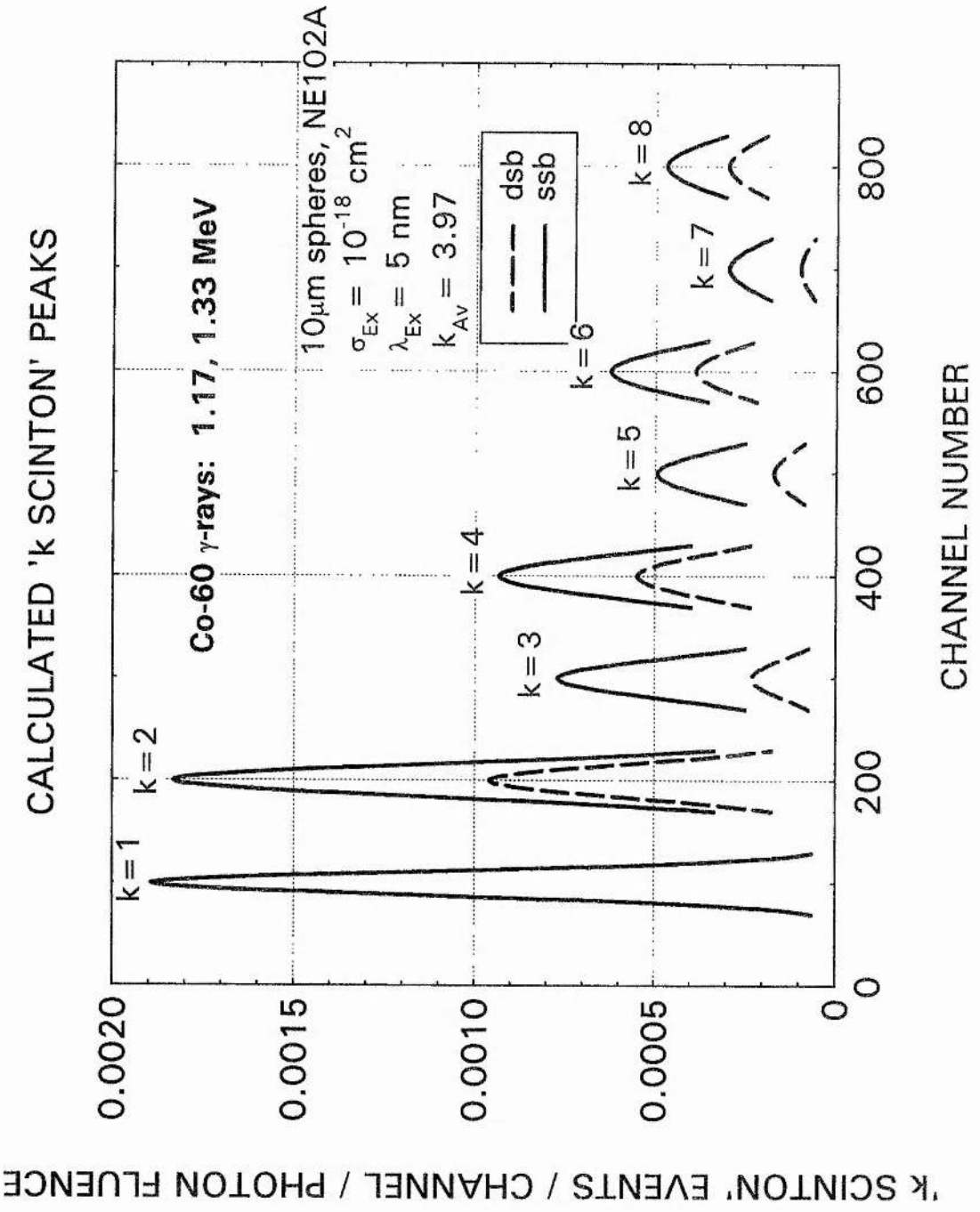

Figure 2.5 Theoretical scinton yield for cobalt-60

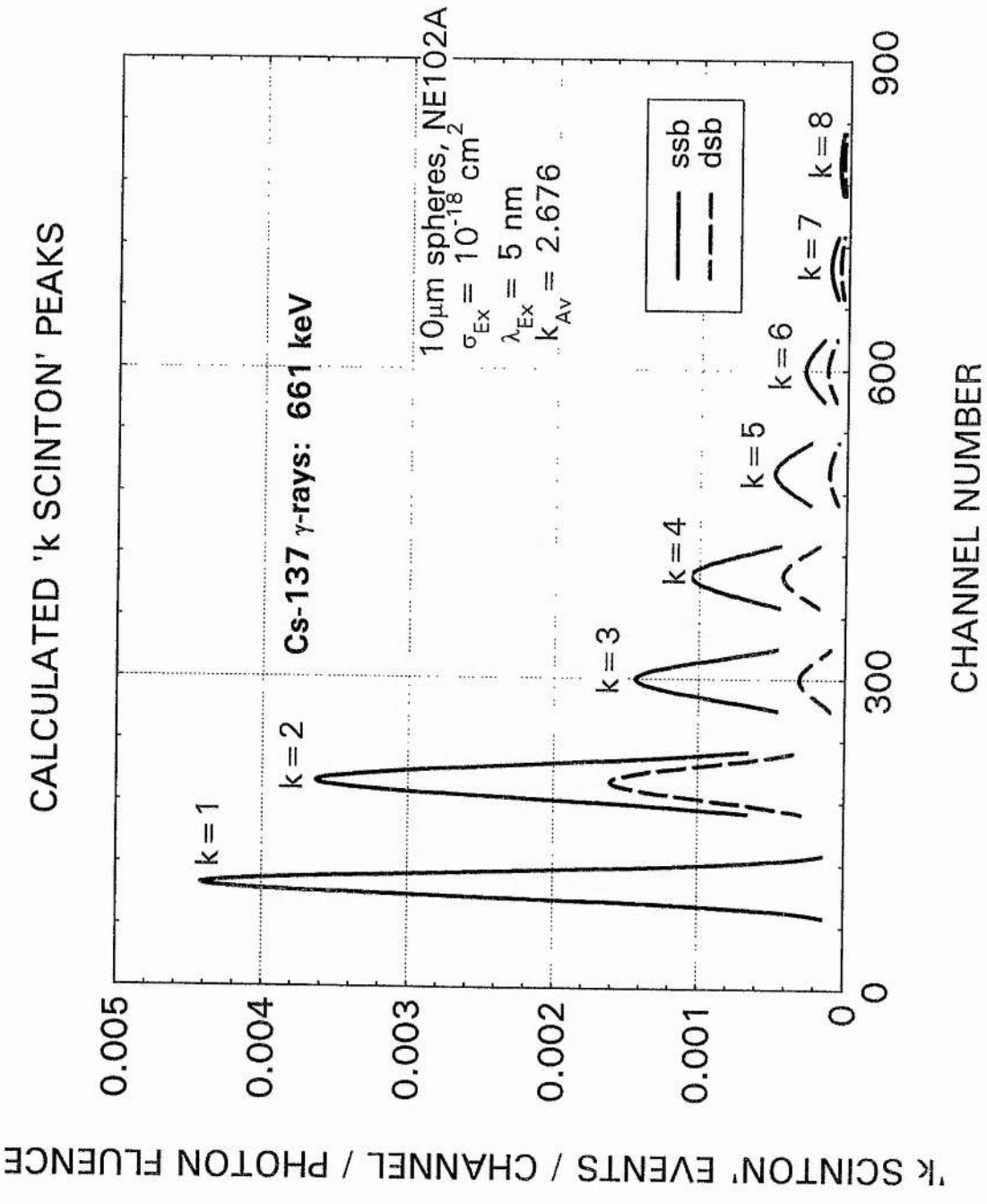

Figure 2.6 Theoretical scinton yield for caesium-137

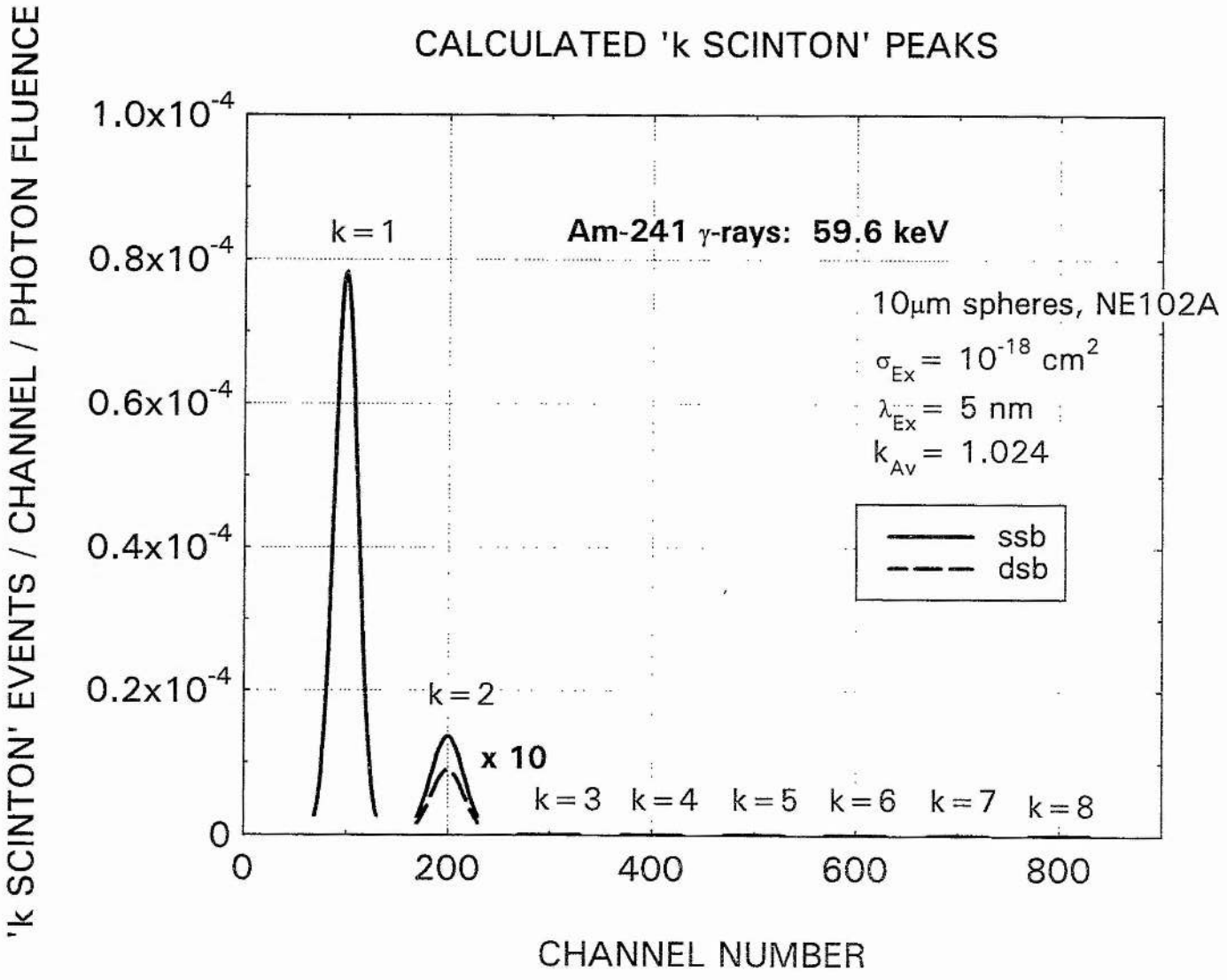

Figure 2.7 Theoretical scinton yield for americium-241

Chapter III

Design

3.1 Introduction

In this chapter the design and operation of the single photon counting apparatus is discussed in detail. The majority of the electronics used were general purpose units that did not require any internal electronic or external structural modifications to enable their integration into the experimental arrangement. Prior to the inclusion of each piece of equipment in the setup, it was individually and rigorously tested for electronic noise emissions, the effectiveness of its RF shielding and the conductivity of all BNC sockets. This ensured that a consistent level of equipment performance was maintained throughout each stage of the experiment. For measurements made in the coincidence mode, identical electronics were used in post-detection amplification stages on both signal and gating circuits to ensure a uniform performance.

All leads were carefully selected to ensure their shielding and conductivity were intact. A lead that displayed a less than optimum performance was removed and replaced with a newly made lead. The positioning of leads relative to RF-emitting equipment, such as PCs and oscilloscopes, was also monitored to ensure that leads were not exposed to significant RF-fields. During PMT calibration experiments, it

was found that fully-shielded leads were still susceptible to RF-noise generated by a standalone MCA leading to the swamping of weak signals.

One of the most critical parts of the apparatus was the light-tight housing which contained the scintillation film, light-pipe arrangement and coupling for both photon detectors. It was originally thought that a light-tight enclosure could be constructed of simple black plastic piping, but this proved difficult to couple to the the photon detectors resulting in light leakage which swamped the weak scintillation signals.

The main components of the equipment were: the DEP PP0275A Hybrid Photodiode, an EMI 9835 Photomultiplier, the EG&G Ortec 113 Scintillation preamplifier and Tennelec 243 Spectroscopy Amplifier, and the ORTEC Maestro MCA Card and PC.

3.2 Photon Detectors

The primary aim of these experiments was to detect and distinguish between single and plural photon events produced in a thin scintillation film located in a γ-ray field. Although many conventionally constructed photomultipliers have a sensitivity which allows the integral detection of single photon events, the use of multiple dynode chains in the charge amplification stage sufficiently distorts the statistical electron population to prevent the resolution of a single photoelectron peak from the continuum. If the multiplication factor of each dynode, δ, were fixed, then all output pulses produced by a single photoelectron would have the same amplification. However, δ is a mean value of multiplication with a standard deviation of $\sqrt{\delta}$ (Knoll, 1986). Such conditions lead to a statistic spreading of photoelectron pulses such that individual peaks cannot be resolved.

Studies surrounding the gain enhancement of the first dynode by RCA led to the development of the RCA8850 (Houtermans, 1973). By introducing a Caesiated Gallium-Phosphide [GaP(Cs)] first dynode with a typical multiplication factor of ~30, in series with a conventional dynode chain, the relative variance, $(\sqrt{\delta}/\delta)^2$, is reduced from 0.562 to 0.033. These developments, however, at best allow the resolution of up to three photopeaks.

Adopting a revolutionary approach to photoelectron detection is the Hybrid Photodiode (HPD) produced by BV Delft Electronische Producten (DEP), in the Netherlands. By removing the conventional dynode chain and replacing it with a single high voltage acceleration stage followed by a diode detector, individual photoelectrons can be detected with the sacrifice of reduced gain. Since the photoelectron statistics of the HPD can be approximated to that of a high gain first dynode in a conventional photomultiplier, peak spread is found to be dramatically reduced.

3.2.1 DEP Hybrid Photodiode

The PP0275A Hybrid Photodiode (HPD) is a revolutionary new photon detector that allows the resolution of peaks containing up to 15 simultaneous photoelectrons (DEP, 1995).

Light incident upon the bialkali photocathode releases a proportionate number of photoelectrons. These are accelerated through two potentials of -11 kV and -13kV respectively while being focused onto a single T-type Silicon PIN diode operated at a positive voltage bias of approximately 70V. Each photoelectron hitting the diode creates some 275 electron-hole pairs per keV electron energy within its depleted

volume. Photoelectrons accelerated to 13 keV by the corresponding potential difference between photocathode and diode, give rise to 3575 electron-hole pairs. This is more than two orders of magnitude higher than the secondary electron yield at the first dynode stage of a conventional photomultiplier (D'Ambrosio *et al.*, 1993).

The HPD is constructed in a metal case inside a high density polymer housing, and is of a compact construction with a 25.4mm fused silica end-window with an active diameter of 18mm. It also offers very good time and temperature stability and high stability gain of 3500 at 15kV. A low dark current of 30 counts per second at 20°C produces low background for single photon counting.

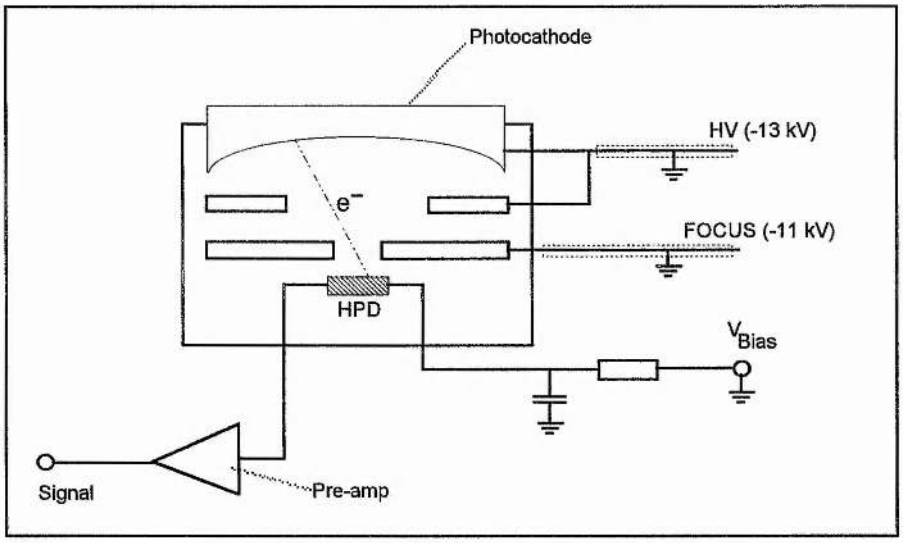

Figure 3.1 Internal schematic of HPD

The diode bias voltage, V_{bias}, was provided by a Farnell Instruments Ltd E350 Stabilised Voltage Supply. Incorporated into the base of the HPD is an integrated low noise pre-amplifier with a non-inverting intrinsic gain of 1. The positioning of the

preamplifier inside the HPD housing provides a minimum capacitive loading on the detector.

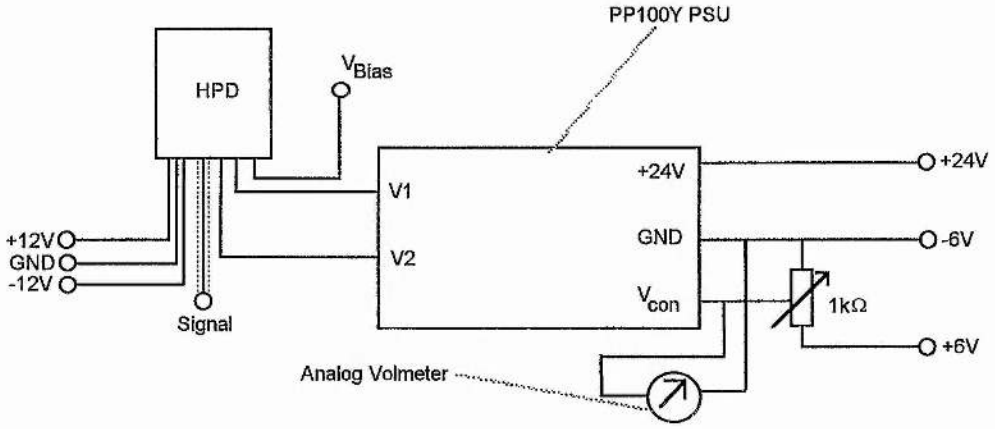

Figure 3.2 Wiring diagram of Voltage Control Unit and HPD

The HPD is powered by the PP0100Y High Voltage Supply, which itself is powered by a 24V dc supply. The high voltage output is controlled by a 0-6V potentiometer providing HT outputs of between 0 and 15kV. The HT PSU control voltage was monitored by a 0-10V analog voltmeter connected in circuit. Additional and more accurate voltage monitoring was provided by a digital multimeter.

Original evaluation experiments of the performance of the new DEP hybrid photodiode (HPD) design carried out by D'Ambrosio *et al* (1993) provided many valuable details of the most suitable experimental arrangement.

3.2.2 EMI 9789 Photomultiplier

The EMI 9789 photomultiplier, built by Thorn EMI Electron Tubes, was chosen as the coincidence gating detector for its high gain, low dark current and suitability for use in low light level applications.

The phototube was housed inside a standard flanged 52mm B2F/RFI light-tight housing with integral mu-metal shield which provided additional RF shielding. The flange arrangement allowed the photomultiplier to be easily coupled onto the experimental arrangement, ensuring a light-tight seal enhanced by the inclusion of a rubber 'O' ring in the joint. To achieve its low dark current, the original 45mm diameter bialkali photocathode was stopped down by a factory installed shutter to provide an effective photocathode diameter of only 10mm. Secondary electron amplification was provided by a 13 stage venetian blind dynode system of caesiated antimony (CsSb) coated dynodes, providing a typical gain of 25×10^6.

The EMI 9789 was powered by an EG&G Ortec 556 High Voltage Supply and operated at a nominal voltage of 1700V. This provided a typical output signal voltage of 5 mV.

3.2.3 Electronics

The electronics consisted of an Ortec pre-amplifier and a set of two Tennelec main amplifiers feeding into an EG&G Ortec T100 Coincidence MCA card. Every effort was made to operate the detectors with identical electronics. The amplifiers were mounted in and powered by a Tennelec MiniBin with TC909 power supply unit. Amplified signal outputs were monitored by two oscilloscopes, a Tennelec model 2210 and a Gould DM3010, which drew their signal from the rear unipolar output terminals.

3.2.3.1 Ortec 113 Scintillation Preamplifier

An EG&G Ortec 113 Scintillation preamplifier was used in the pre-amplification stage of the EMI 9789 photomultiplier. The preamp consisted of a non-inverting amplifier with unit gain, and drew 24V directly from the main amplifiers into which its signals were fed. As short as possible a cable was used to connect the photomultiplier output to the preamp to minimize capacitive loading in the circuit. With a nominal input capacitance of 45pF, the preamp was provided with a switchable input capacitance, however, this feature was not used.

3.2.3.2 Tennelec 243 Linear Main Amplifiers

Main signal amplification was provided by two Tennelec 243 Spectroscopy Amplifiers designed for use with high resolution germanium and silicon semiconductor detectors, silicon charged particle detectors and scintillation detectors. The amplifiers provided both unipolar and bipolar outputs. However, unipolar connections were used on both circuits to match the 0-12V input signals desired by the MCA.

3.2.4 Ortec Coincidence MCA Card

The integrated coincidence detector and multi-channel analyser (MCA) 100T card, produced by EG&G Ortec, was installed in a dedicated 486-SX 33MHz PC which ran the Ortec Maestro MCA software.

The MCA was designed to operate over a signal input range of 0-12V which was displayed in 2048 channels such that each channel width represents ~5.8mV.

Amplified photomultiplier signals were fed into the ADC port on the card, where signals were digitised prior to being displayed on screen.

In the coincidence counting mode, gating signals from a second photomultiplier (EMI 9789) are fed into the gate port. A coincidence was registered if the gating pulse occurs prior to the signal pulse and extends 0.5μs beyond the time of the signal pulse detection. The input gate voltage was set to initiate a pulse of 5ms duration within the 2-10V range.

Localised heating by the card located inside the enclosed environment of the PC could not originally be controlled by the PC's own cooling fan and this eventually led to the development of current leakage on the reset circuitry causing intermittent operation. Subsequently, when the MCA was in use, the top cover of the PC casing was completely removed to allow the free circulation of air and prevent further overheating.

The MCA card was originally housed in the ADCAM ANALYST Model 100T stand-alone MCA.

3.3 Light-Pipe Housing

In the original arrangement of the apparatus, which operated solely with the Hybrid Photodiode and not in the coincidence mode, a Polymethyl Methacrylate (PMMA, Perspex) light-pipe, of length 40mm and width 25mm, was used to couple the scintillation detector to the photocathode window. The light-pipe was covered with a 12μm aluminum reflector. Surrounding the arrangement was a 60mm diameter metal pipe which covered both the HPD and the light-pipe. By introducing an opaque fabric material into the metal pipe's aperture, completely covering the scintillator,

background light pollution was markedly reduced. However, a small light-leak persisted. This problem was solved by housing the entire arrangement inside a sealed lead-castle. This arrangement also offered some protection from any source that was being monitored.

Early on in the operation of this arrangement, collected spectra were noted as still having a poor signal-to-noise ratio. This was characterised by a broadening of photoelectron peaks coupled with a marked increase in inter-peak background counts. Two possible sources of this extra noise were identified. The sources being used, ^{60}Co and ^{137}Cs, are high energy γ-ray emitters with sufficient energy to give rise to Cerenkov radiation by Compton backscattering of electrons in the light-pipe. This interference mode had previously been reported as a source of considerable levels of spectral noise in fibre optics under γ-ray irradiation [(Crossman, 1996), Private Communication], and by Beddar *et al.* (1992). Additionally, in the absence of a light-pipe, a significant increase in the number of detectable events was noted when γ-ray sources were placed at a distance of 40mm from the detector. From this evidence, it was concluded that a significant number of γ-ray events from ^{60}Co and ^{137}Cs were interacting directly with the HPD's photocathode, and possibly with the depleted layer of the photodiode itself.

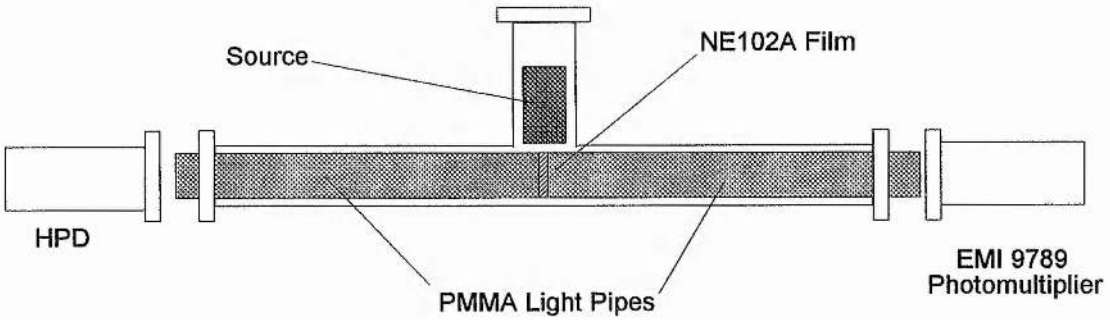

Figure 3.3 Design of light-pipe housing, which allowed easy insertion and removal of sources without the introduction of light into the system.

By comparing the relative intensities of Cerenkov noise and direct γ-ray interactions, the latter were found to be several orders of magnitude greater. It was therefore more beneficial to shield against direct interactions at the expense of slightly increased Cerenkov noise. The classical solution would have been to completely remove the photocathode from the γ-ray field. This approach, however, was soon rejected as the procedures for the bending of PMMA light-pipes was judged to be too complex. The alternative was to reduce the fluence of γ-rays reaching the photocathode by introducing a γ-ray absorber that appeared relatively translucent to the photon fluence. The PMMA light-pipe did not provide any significant γ-ray absorption over its short length. However, by increasing the length, the solid angle subtended by the photocathode would be reduced, and thus γ-ray interactions would also be reduced.

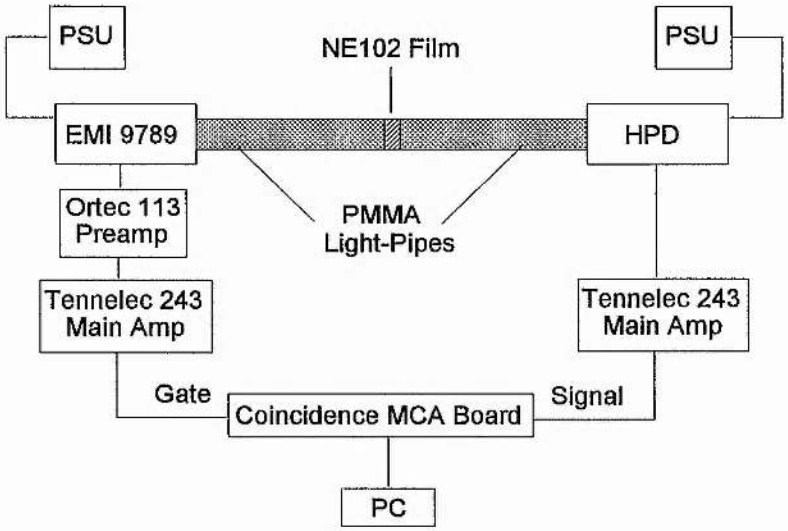

Figure 3.4 Schematic of Experimental Arrangement

In the final series of experiments, which focused on the response of a single detector, the EMI9789 was removed from the arrangement, and only the DEP Hybrid Photodiode was used. On theoretical considerations, interpretation of a coincidence-acquired spectrum was potentially more complex, and therefore added no overall benefit to the collection process. Although removing coincidence techniques may have resulted in a poorer signal-to-noise ratio, software tools were developed to extract data from the spectrum. Removal of the second light-pipe caused the scintillation film to be exposed. This was overcome by covering the film with a 12μm aluminium reflector film, ensuring a light-tight seal and near 2π collection of photons. A schematic of this arrangement is shown in figure 3.5.

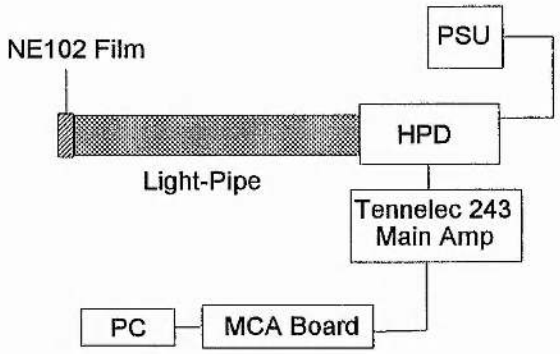

Figure 3.5 Final Experimental Arrangement

3.4 Organic Scintillators

The organic scintillator selected for these experiments was a 20μm film of the plastic scintillator NE102A. The tissue equivalence of organic scintillators is achieved by their similarities of chemical and molecular composition to that of tissue, and thus their response to ionising radiations.

3.4.1 Bio-Equivalent Scintillators

In the proposed system of absolute biological effectiveness (ABE) dosimetry, a new family of specifically engineered organic scintillators are required that are not only tissue equivalent in molecular terms but also in terms of their physical biological equivalence. The key to the success of ABE dosimetry is the ability to position molecular excitation detectors of sub-nanometre dimensions at a mean inter-molecular spacing of approximately 2 nm, matching the mean chord of the DNA helix. Excitation events, which in tissue would produce a double strand break, would in the ABE scintillator produce two spatially correlated paired scintons. Each nanodetector functions as an excitation sensitive site which is capable of signalling its activation with the emission of a single scinton.

Over the past forty years or so, numerous investigations into the efficiencies of organic scintillators (Furst and Kallmann, 1951, Brown *et al.*, 1957) have focused on achieving the optimum concentrations of primary and/or secondary solutes to obtain maximum scinton yields per unit incident radiation fluence. These studies have provided the basis for a wide range of condensed phase and gaseous organic scintillators, many of which are now commercial products.

The design of the ABE family of scintillators, although concerned with high scinton yields to aid in the ease of detection, focuses primarily upon the intermolecular spacing between primary solute molecules. By altering the concentration of fluor molecules dissolved in a solvent, the mean isotropic fluor spacing can be made to match that of the DNA helix.

An alternative approach to the use of an ultra-thin scintillator layer is the use of 5μm spheres of plastic scintillator to mimic the physical inter-cellular spacing found in an in-vitro mammalian cell volume. Such micro-dimensional spheres are already available and are principally constructed of NE102 or similar polymerised scintillators. By further adapting the fluor concentrations in these spheres, fluor spacing could be made to mimic the DNA. The spheres were however unavailable for this series of experiments.

3.4.2 Plastic or Liquid Scintillators

Traditionally, plastic scintillators have always been favoured for thin film applications due to their ease of fabrication and use, and high structural integrity. In ABE applications, where the principle parameter is fluor spacing, traditional benefits may

be disregarded in favour of a medium that supports the desired inter-molecular distribution.

From the complete spatial randomness (CSR) supported by liquid, there is strong reason for selecting liquid scintillators in ABE scintillator design. However, the use of liquid scintillators introduces a number of problems. Low liquid viscosity and high evaporation coefficient of solvents lead to poor structural integrity, while their construction into ultra-thin layers is extremely difficult to achieve. The most appropriate solution is found in the use of Langmuir-Blodgett films which can be fabricated into layers of sub-micron thickness. No equipment for production of LB-films was available in the laboratory so this option could not be further investigated.

3.4.2.1 High Viscosity Liquid Scintillators

A possible solution to the problems encountered when using the ultra-small volumes of liquid scintillators outlined above may be the use of silicone oil as a secondary pseudo-solvent.

In most organic liquid scintillator applications, large solvent volumes are used, and absorbed instrument heating, which would otherwise lead to rapid solvent evaporation, is generally not considered a serious problem. In smaller volumes, the use of customised sealed cells with built-in vapour expansion chambers again ensures that solvent evaporation does not lead to a degradation in detection quality.

While these processes work well when the depth of liquid is not critical, ABE films of a few microns thickness cannot generally be achieved in sealed cells because of the complexities of cell manufacture at these dimensions. Such films are ordinarily produced by sandwiching a liquid droplet between two flat, optically transparent

surfaces, and allowing the liquid to uniformly propagate over the surfaces. The two surfaces are held together by the surface tension of the liquid and any excess solvent drains off at the edges. One surface may then be optically coupled to the PMT and measurements may be made. Using this method, films of NE224 have been produced with a mean thickness of 8μm.

The high volatility of the organic solvents used in liquid scintillators means that such films have a limited life-time, and the 8μm NE224 film can survive the PMT operating environment for approximately two hours before the onset of evaporation leads to localised damage of the film. Cryogenic cooling with liquid nitrogen may have appreciably lengthened this life-time as well as ensuring an inert operating atmosphere for the liquid. However, this option was not seriously investigated as a viable alternative as cryogenic cooling in a future radiation dosimeter would limit its intrinsic portability.

An alternative process to using pure liquid scintillator for film production is to combine the liquid scintillator with a viscous fluid of suitable optical qualities. The most suitable fluid is silicone oil which is optically transparent at scinton wavelengths and therefore does not compound the efficiency losses associated with solvent absorption. The addition of equal parts of silicone oil (12,500 cS) and NE224, which uses pseudo-cumene (1,2,4-trimethylbenzene) as its solvent, produces a scintillation oil that can be used in thin film production while providing in-built optical coupling. The solvent-oil mix in these proportions does not produce an appreciable reduction in the viscosity of the oil, however, there is some evidence that primary and secondary solute re-crystallisation occurs in samples after a few months. This is thought to be due to the loss of primary solvent through evaporation, however, the rate of solvent loss is much reduced.

3.5 Scinton Losses and Collection Efficiencies

Determination of the actual number of events occurring in the scintillator is largely dependent upon not only the photomultiplier's ability to record such events, but also on the accuracy with which losses throughout the system are known. There are various stages in the detector at which photons can be lost, either through inefficiencies or by other physical processes. In order to make an accurate assessment of absolute scinton activity, each loss process must be identified and the magnitude of loss calculated.

The following parts of the system are identified as potential mechanisms by which scintons may be lost:

1. The use of silicone oil to optically couple the plastic scintillator to the light-pipe. Since the scintillator has a higher refractive index (1.58) than silicone oil (1.5), total internal reflections are possible. Similarly, the refractive index of the Perspex light-pipe (1.495) is slightly less than silicone oil and again some total internal reflections are possible. Both prevent some scintons from entering the light-pipe.
2. The Perspex light-pipe is known to attenuate light with a net attenuation coefficient of 0.734 m^{-1} (Tove, 1956) over a typical range of scintillation wavelengths, ~380-450nm.
3. The quantum efficiency of the photocathode.

3.5.1 Scintillator Emission Spectrum

Scintillation molecules are chosen specifically for their radiative response to ionising radiations. High scinton yielding molecules, however, emit most of their light at near-UV wavelengths (330-400nm), which are outside the detecting capabilities of most photocathodes. In order to allow detection with conventional non-quartz windows, a secondary *wavelength-shifting* solute is added to most liquid and plastic scintillators. These molecules readily absorb photons in the 330-400nm range and re-radiate them at wavelengths of typically 410-450nm.

3.5.2 Quantum Efficiency of Photocathode

Deposited on the inner surface of the photomultiplier window is a thin layer of photosensitive material, composed of a mixture of alkali metals. Under illumination by photons of appropriate energy, the photocathode gives rise to the release of photoelectrons with a quantum efficiency, $\eta(\lambda)$.

In most practical situations, the quantum efficiency is expressed as an average value over its entire wavelength window. The efficiency is strongly wavelength dependent. It is therefore essential that the emission spectrum of the scintillator closely matches the response spectrum of the photocathode. The NE102A organic scintillator strongly radiates at a wavelength at 423nm corresponding to an energy of 3eV. At the same wavelength, the quantum response of the DEP Hybrid Photodiode is approximately 25% (DEP, 1996), and thus, four scintons are required to release a single photoelectron.

3.5.3 Light Transmittance

The detection of a scinton yield is heavily dependant on the scinton reaching the photocathode. The main method of transporting scintons from the scintillator to the photocathode is by a light-pipe arrangement.

3.5.3.1 Light-Pipes

It is not always possible or indeed desirable to couple a scintillator directly onto the face of a photocathode. Quartz and high transparency organic polymer light-pipes are used to transport light over reasonably short distances from the scintillator to the photomultiplier. Although light-pipes have many uses, and undoubtedly overcome many of the problems associated with radiation detection, they also introduce a substantial amount of light loss through various loss processes.

In this experiment, the use of light-pipes was necessitated by the high yield of direct γ-ray interactions with the photocathode, producing a significant number of spurious counts which could not be distinguished from true scinton events. By introducing a length of light-pipe into the experimental arrangement, each γ-ray source could be moved to a distance at which the number of direct interactions would fall below acceptable limits.

The length of the light-pipe selected was based upon three related considerations: the solid angle subtended by the photocathode, the attenuation of γ-rays and the attenuation of the scinton yield. Data on the attenuation of γ-rays in polymethyl methacrylate (PMMA) (Hubbell, 1981) indicated that no significant attenuation could be achieved by lengthening the light-pipe. Based upon the exponential photon absorption law and the attenuation coefficient for optical photons in PMMA of 0.734

m^{-1} (Tove, 1956), lengthening the light-pipe to 220mm caused a 15% loss of photons. At that length, the solid angle subtended by the detector reduced the γ-ray fluence by 90% at the photocathode.

In the final experimental design, a 20μm film of NE102 plastic scintillator, of diameter 25.4mm, was sandwiched between the ends of two Perspex light pipes, each measuring 25.4mm in diameter and 220mm in length. Good optical coupling between the NE102 and light pipes was provided by a thin coating of Hallison 12,500cS silicone fluid.

Although the scintillator diameter matched that of the light pipe, which has been suggested as a possible source of photon loss (Birks, 1956), this arrangement effectively provided 2π collection of the emitted scinton yield on both sides of the scintillator and therefore losses due to the choice of scintillator diameter were assumed to be negligible in comparison to the overall collection efficiency of the design.

Chapter IV

Monte Carlo Photon Transport Code

4.1 Introduction

It is often necessary that a light-pipe be introduced into an experiment to provide separation between the scintillator and photon detector. In this series of experiments, it was desirable for just such a separation to ensure that the hybrid photodiode was positioned outside the immediate γ-ray field of the sources in use.

By introducing a light-pipe into an experiment, an additional mechanism by which photons are lost is also introduced since some photon attenuation will occur along its length. The optical properties of light-pipes are now well established (Knoll, 1986) and the fractions of incident light transmitted by a number of suitable transparent materials has been investigated (Tove, 1956). However, in the absence of a precise quantitative measurement of the transmission probability of a known fluence of optical photons through a system of arbitrary length, the intrinsic photon transmission probability is conventionally estimated by the exponential attenuation law, $I=I_0e^{-\mu l}$. While this method is adequate for some applications, a more rigorous approach is required here.

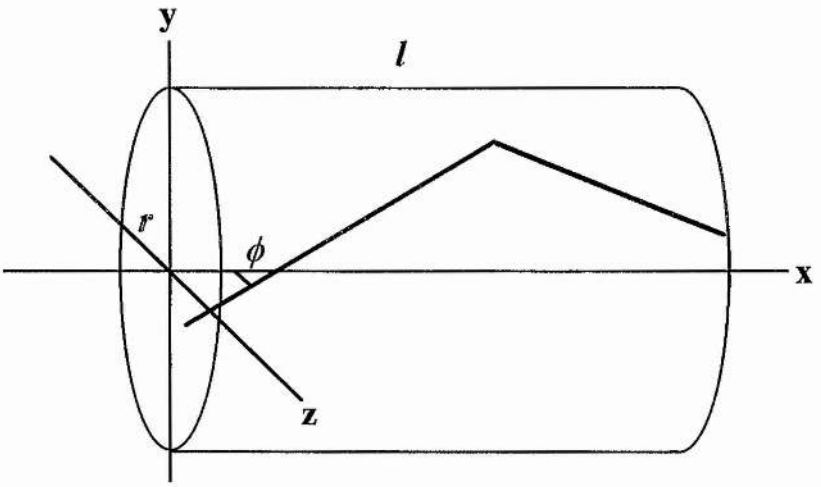

Figure 4.1 Schematic of the critical dimensions of a light-pipe

The use of exponential attenuation in light-pipe applications is well documented (Birks, 1964), however, experimentally obtained measurements (Kilvington *et al*, 1970) in Perspex have established a significant divergence of the theoretically predicted attenuation from that observed in practice. It was therefore necessary to provide a more rigorous model of photon attenuation to account for all the losses in such arrangements. The most suitable method of providing such a model for determining transmission probability is by Monte Carlo simulation.

To construct a Monte Carlo code of photon propagation, the principal mechanisms of loss must be identified. These are: photon absorption due to molecular excitations in the medium; reflection inefficiencies at external reflectors; and photon transmission due to non-total internal reflection events.

To a first approximation, it is assumed that the bulk of photon losses can be accounted for by the inefficiencies of Fresnel reflections, by the transmission of photons through the walls of the light pipe during these reflections, and by molecular

absorption and chemical impurities. This latter loss mechanism is strongly wavelength dependent, however, in the absence of adequate data, a single loss coefficient for all wavelengths was assumed. From these basic assumptions, a Monte Carlo code is constructed to simulate the propagation of photons in any linearly constructed transparent medium.

A further source of transmission inefficiency but not included in the Code is the scattering of light at both optical boundaries and by impurities. Light scattering is caused by optical aberrations in the medium which, by their nature, cannot support the law of specular reflection or total internal reflection. The resulting photon is scattered through some arbitrary angle and has a high probability of being scattered out of the light pipe and thus lost. Even with perfectly polished surfaces, aberrations are still present and cause photon loss along the entire length of the pipe (Tove, 1956).

Previous experimental investigations of the transmission probability of light (Jelley, 1956, Tove, 1956, Timmerhaus *et al*, 1950) have provided good data on the transmission probability of light as it propagates through a perspex (polymethyl methacrylate or PMMA) light-pipe, however, no precise relationship between light-pipe dimensions and total transmission probability has been presented. For this reason, the Monte Carlo code was constructed to allow accurate estimates to be made of photon losses in this and other light propagating systems.

4.2 The Monte Carlo Code

The Monte Carlo code was constructed around a cylindrical light-pipe of length, l, radius, r, and refractive index, n. To a first approximation, the material was assumed to have unit transparency at all wavelengths such that UV absorption may be neglected. Photons are assumed to enter the light-pipe at a random point in yz-space, (y_i, z_i), such that

$$\sqrt{y_i^2 + z_i^2} < r \qquad (4.1)$$

Forward propagation of photons along the x-axis is described in terms of two random orientations expressed relative to the major light-pipe axis; ϕ, the angular orientation in the xz-plane, and, θ, the angular orientation is the xy-plane. Both orientations exist within the limits of $-\pi/2$ and $\pi/2$, such that when both ϕ and θ are equal to zero, the photon will propagate parallel to the major axis, x. This propagational angle is denoted in three dimensional space as Ω.

By repeated iterations, each photon is allowed to propagate through the light-pipe. At points where the photon intercepts the light-pipe wall, the new reflected orientation is calculated and the photon allowed to continue propagating. At light-pipe walls, two reflection options are available: total internal reflection if the angle of incident is less that the critical angle at the interface, or a less efficient reflection by a reflector for photons which have crossed the light pipe - air interface. Total internal reflection is assumed to have an efficiency of 100%, while the reflector is assumed to be approximately 86% efficient.

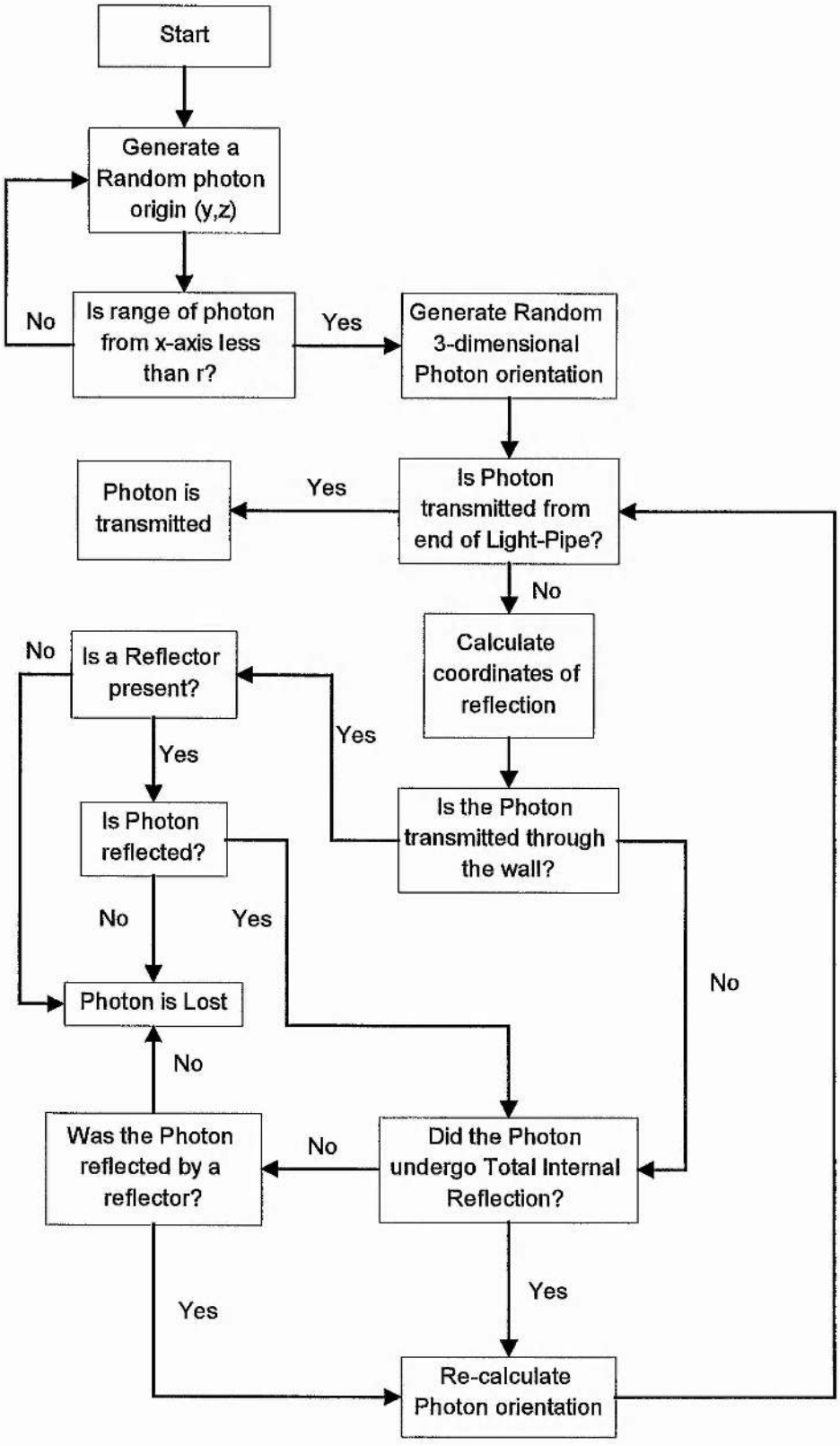

Figure 4.2 Flow Chart of the steps in the Monte Carlo code.

Each history was terminated when the photon path was determined to have left the light-pipe at $x = l$ within the limits of $-r$ and r, or if the photon has been transmitted through the wall without subsequent reflection.

Photon transport efficiencies are determined by the type and number of reflections undergone by each photon, as well as the total distance travelled through the light pipe. Under conditions of total internal reflections, the photon transport efficiency due to reflections only is unity. With an external reflector, and in the absence of total internal reflections, the photon transport efficiency, T, is given by

$$T = \sigma^R \qquad (4.2)$$

where σ is the reflectivity of the reflector, typically 0.86, and

R is the total number of reflections undergone by the photon.

Under realistic conditions, losses due to absorption are also present. The magnitude of absorption is a function of the photon's linear track length and may be expressed by the exponential absorption law. By incorporating an exponential term into Eqn 4.3, the photon transport efficiency can be written as:

$$T = \sigma^R.exp(-\mu l) \qquad (4.3)$$

where μ is the photon absorption coefficient of the light-pipe material, and

l is the photon track length.

In the case of total internal reflections where $\sigma = 1$, Eqn 4.3 would reduce to the exponential form.

The original Monte Carlo code was written in QBASIC and run on a 33 MHz 486DX PC. The code required approximately 100 hours to run 50,000 random events at various lengths of light-pipe between 10mm and 1m at a radius of 12.7mm. This version of the Code incorporated individual reflection and propagation length calculations, significantly adding to the run time. The impracticalities of running such a lengthy code for only minor adjustments in parameters prompted the derivation of the equations of geometry that support photon propagation. These equations formed the basis for a second generation Monte Carlo code that provided results in a much shorter time. Of particular interest were the two parameters which appear critical to photon loss: photon track length, λ_p, and the number of reflections undergone by a photon, R.

4.2.1 Photon Track Length

The transmission efficiency of a light-pipe is generally expressed in terms of the exponential optical absorption coefficient of the transparent medium. Such an exponential absorption relationship describes the attenuation of a given fluence of photons as it propagates radially through the medium over a known distance. However, the radial propagation model of photons propagation through a light-pipe does not account for the constraints are imposed on the photon track by the geometry of the propagating medium.

Propagating photons are essentially trapped in the light-pipe for the duration of their flight and undergo many reflections, thus lengthening their track through the

medium. In this highly anisotropic environment, photon propagation can no longer be described in terms of isotropic propagation, and as such, a simple exponential absorption model will over-estimate transmission probability, since the physical length of the light-pipe is always less than the mean distance travelled by a photon.

Analysis of a series of light-pipes of various lengths confirmed the predicted lengthening of photon track length, and revealed a functional dependency on photon orientation but not on the number of reflections as might be expected. Photon track length, λ_p, is related to the longitudinal dimension of the light-pipe and photon orientation, but is independent of photon origin, light-pipe radius and the number of reflections. In a two-dimensional model, total photon track length is given by:

$$\lambda_p(\theta) = \frac{l}{\cos\theta_i} \qquad (4.4)$$

where l is the physical length of the light-pipe, and

θ_i is the initial orientation of the photon in the xy-plane

In three-dimensional space, the total photon track length travelled may be written as:

$$\lambda_p(\theta,\phi) = \frac{l}{\cos\theta_i . \cos\phi_i} \qquad (4.5)$$

or

$$\lambda_p(\Omega) = \frac{l}{\cos\Omega_i} \qquad (4.6)$$

where l is the length of the light-pipe,

θ_i is the initial orientation of the photon in the xy-plane,

ϕ_i is the initial orientation of the photon in the xz-plane, and

Ω_i is the initial orientation of the photon in 3D space.

In figure 4.3, the three-dimensional solution to equation 4.6 is shown for a light-pipe of length 1m and radius 12.7mm, illustrating the relationship between photon track length and photon orientation. The photon track length, λ_p, is expressed as the natural logarithm of the function in order to reveal structure. Photon track length is expressed in metres.

4.2.2 Photon Reflections

The number of reflections a photon undergoes is a critical parameter for overall loss determination. If it is assumed that photon scattering predominantly occurs at optical boundaries, then the probability of losing a photon through scattering is proportional to the number of boundary reflections made by the propagating photon.

A simple routine was written to investigate the number of reflections undergone by photons with respect to their initial orientation to the major axis. From analysis of the geometrical configuration of the light-pipe, and comparing this with calculated data, a fundamental geometrical relationship was derived. Since fractional reflections are not possible, the function appears as a function with integer results. In a two-dimensional approximation, the total integral number of reflections, R_{max}, a propagating photon can undergo in a light-pipe of length l and radius r is therefore given by

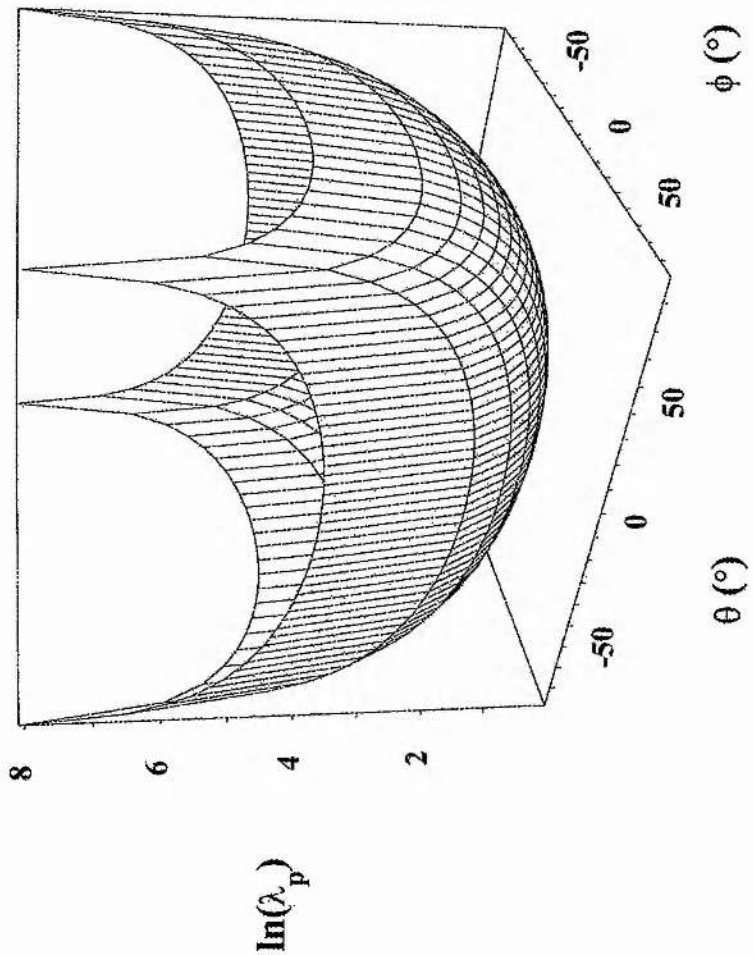

Figure 4.3 The three-dimensional solution to Equation 4.6 for a light-pipe of length 1m and radius 12.7 mm.

$$\left[R_{\max}\right] = 0.5 + \frac{y_i}{2r} + \frac{l}{2r.\tan\left(\frac{\pi}{2} - \theta_i\right)} \qquad (4.7)$$

where θ_i is the initial photon orientation in the *yx*-plane , and

y_i is the initial photon lateral *y*-coordinate relative to the major axis.

As θ_i tends towards $-\pi/2$ or $\pi/2$, the number of reflections rapidly increase towards infinity. It is assumed that photons with such orientations would be lost through multiply reflections. This allows a limiting orientation to be imposed on any subsequent calculation thus avoiding infinities in the calculation.

In three-dimensional space, Equation 4.7 may be written as

$$\left[R_{\max}(\Omega)\right] = 0.5 + \frac{\sqrt{y_i^2 + z_i^2}}{2r} + \frac{l}{2r.\tan\left(\frac{\pi}{2} - \Omega_i\right)} \qquad (4.8)$$

where Ω_i is the initial photon orientation in the *xyz*-plane

y_i is the initial photon lateral *y*-coordinate relative to the major axis.

z_i is the initial photon lateral *z*-coordinate relative to the major axis.

The three-dimensional solution to Equation 4.8 is illustrated in Figure 4.4. The light-pipe is of length 1m and radius 12.7mm. The magnitude of reflections is expressed as the natural logarithm of the function in order to reveal structure.

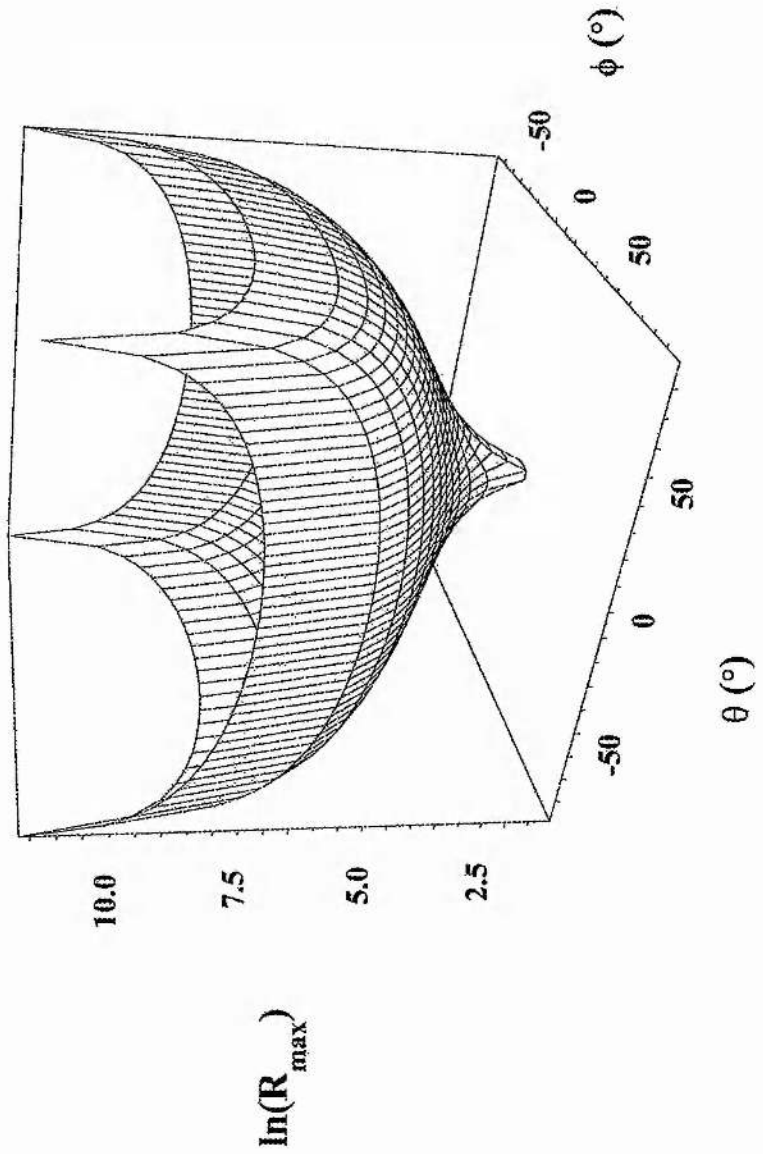

Figure 4.4 The three-dimensional solution to Equation 4.8 for a light-pipe of length 1m and radius 12.7 mm.

4.2.3 Photon Loss Model

A successful alternative model describing photon losses in a light-pipe must take several loss processes into account, such as absorption and inefficient reflections.

The conditions under which propagation occurs are determined by a series of boundary conditions principally relating to the behaviour of photons incident on the edge of the light-pipe at angles greater that the critical angle, θ_C, of the optical interface. These rules relate to the addition of reflective materials around the light-pipe and represent all likely configurations in which a light-pipe is likely to be used. The configurations and associated boundary conditions are:

(a) No Reflector

i. Photons incident upon the edge of the light-pipe at an angle $\geq \theta_C$ are reflected with unit efficiency.

ii. Photons incident at an angle $< \theta_C$ are lost.

(b) Reflector loosely coupled to the light-pipe

i. Photons incident upon the edge of the light-pipe at an angle $\geq \theta_C$ are reflected with unit efficiency.

ii. Photons incident at an angle $< \theta_C$ are reflected back into the light-pipe with an efficiency determined by the reflectivity of the reflector. Longitudinal displacement is assumed to be negligible.

(c) Reflector optically coupled to the light-pipe

i. Photons incident upon the edge of the light-pipe at an angle $\geq \theta_C$ are reflected with an efficiency determined by reflectivity of the reflector and the refractive index of optical coupling material.

ii. Photons incident at an angle $< \theta_C$ are reflected back into the light-pipe with an efficiency determined by the reflectivity of the reflector and the refractive index of optical coupling material. Longitudinal displacement is assumed to be negligible.

By introducing a scattering probability to account for non-specular reflections and an absorption function, an photon loss model may be constructed.

Let σ_r be the reflection probability at the boundary and σ_s be the scattering probability at the boundary, then the final probability of a photon surviving, T, following losses by reflections and scattering after R boundary reflections is

$$T = \left[(\sigma_r.(1-\sigma_s)\right]^R \qquad (4.12)$$

Let μ be the photon absorption coefficient of the medium, then the probability of light being transmitted from the absorbing medium, A, is

$$A = \exp\left(-\frac{\mu.l}{\cos\theta_i.\cos\phi_i}\right) \qquad (4.13)$$

The total reduction in photon fluence within the light-pipe, L, is therefore given by the product of equations 4.12 and 4.13, such that

$$L = \left[\sigma_r.(1-\sigma_s)\right]^R \exp\left(-\frac{\mu.l}{\cos\theta_i.\cos\phi_i}\right) \qquad (4.14)$$

A much simplified Monte Carlo code incorporating Equations 4.7 and 4.14 was written and the results are shown in Figure 4.5. The values of σ_R and σ_S were determined by the propagation angle Ω. For $\Omega \leq \theta_C$, $\sigma_R = 1$ and $\sigma_S = 0$ and for $\Omega > \theta_C$, $\sigma_R = 0.86$ and $\sigma_S = 0.003$. For comparison purposes, the theoretical exponential absorption and data from Kilvington *et al.* (1970) have been added.

In each case, the exponential absorption law greatly over-estimates the efficiency with which light-pipes transport photons. Data on such efficiencies are rare, but the Kilvington *et al.*(1970) data, obtained under practical conditions, illustrates the significant discrepancy between experimental practice and accepted theory. The suggested Monte Carlo model offers a promising alternative though tends to over-estimate efficiencies at larger values of l. Further development of this model together with a more accurate knowledge of the scattering probability, σ_s, and the absorption coefficient, μ, and the inclusion of a wavelength dependence would significantly enhance its reliability.

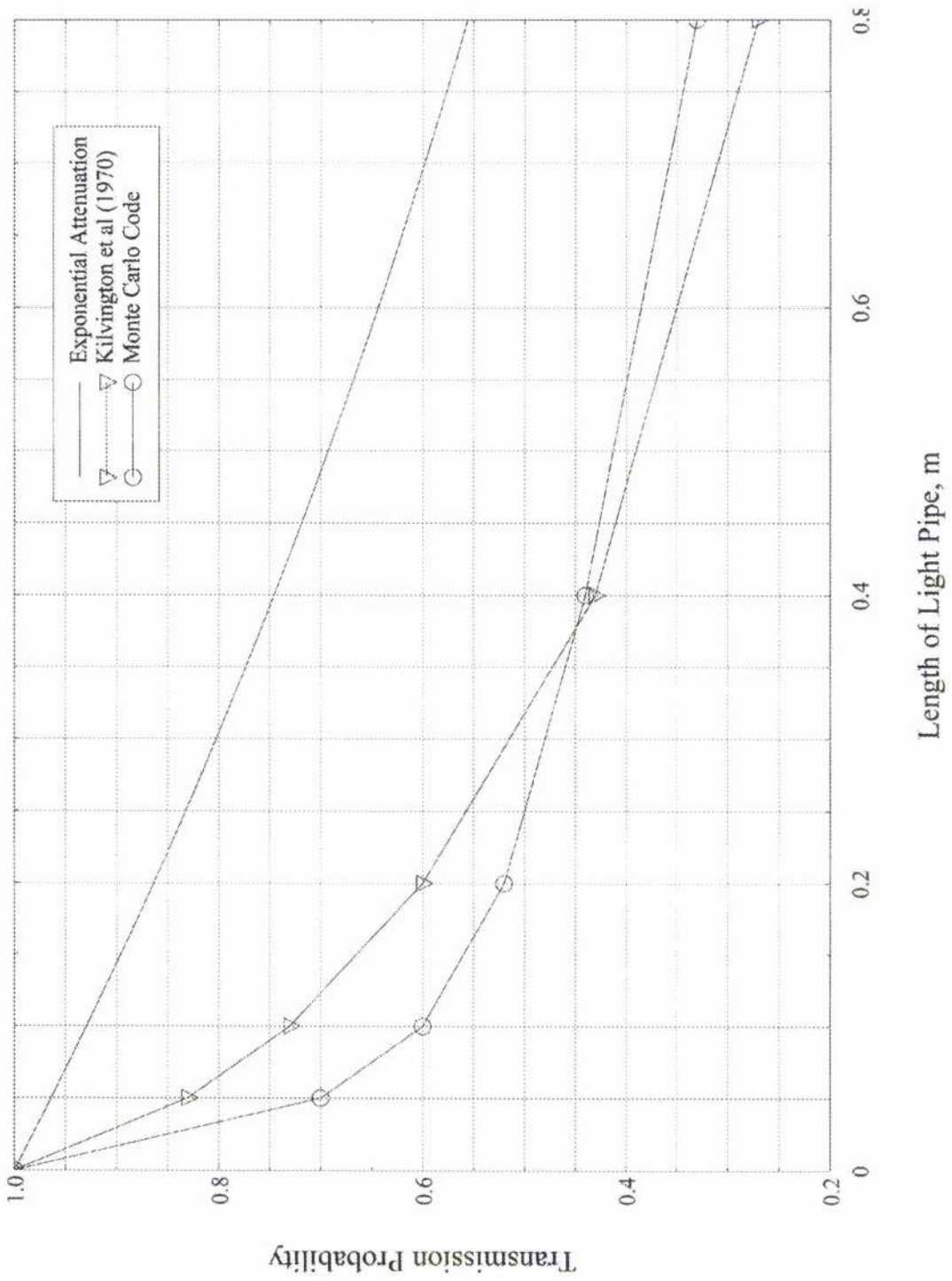

Figure 4.5 Results of the Monte Carlo model ($\sigma_R = 0.86$, $\sigma_S = 0.003$ and $\mu = 0.012$) with the exponential law ($\mu = 0.734$) and Kilvington *et al* data added for comparison. The light-pipe is assumed to be surrounded by a reflective covering which reflects 86% of photons.

Chapter V

Experimental Results

5.1 Introduction

In this chapter, experimental procedures, data collection and reduction routines, and the interpretation of spectra with respect to simulated radiobiological damage will be discussed in detail.

Initial experiments were carried out with a coincidence mode to enhance the signal-to-noise ratio. While this approach provided good results with hot (>1MBq) high energy γ-ray sources (^{60}Co and ^{137}Cs), it proved to be unsatisfactory when used to collect lower energy X- and γ-ray spectra such as ^{55}Fe and ^{241}Am. The principal benefit of coincidence counting was the substantial reduction of unwanted background counts. However, spectra collected by this method proved inherently difficult to interpret and evaluate. These analytical complexities prompted later experiments to be carried out in the photon counting mode.

Final trial experiments concentrated on the response of fluor sites under conditions of charged-particle equilibrium, and it is these data which are discussed.

5.2 Collection of γ-Ray Scinton Spectra

The collection of each spectrum was carried out in an identical manner to ensure a good experimental consistency. The detector was operated in the pulse height analysis (PHA) mode without coincidence gating. After initial switch on, the detector was allowed to reach stable ambient thermal equilibrium. No cryogenic or temperature control was imposed on the detector. Dark counts during this period were significantly higher than at any other time, but diminished rapidly over a period of ten to fifteen minutes. A nominal warm-up period of approximately twenty minutes was used. After this time period, dark counts reduced to a workable level of typically between 500 and 650 counts per second. Various unsuccessful attempts were made to reduce this level further.

Two separate approaches to the positioning of sources were adopted. Firstly, a source could be positioned immediately prior to a run, or secondly, it could be inserted some twelve to twenty-four hours prior. Both methods were examined, but no overall benefit from either method was found.

Three γ-ray sources were used in this series of experiments; ^{55}Fe, ^{60}Co and ^{137}Cs. Each was of a thin disk construction, allowing unrestricted insertion into the detector. Once the source was in place and the light shielding materials replaced, a spectrum was taken. Collection times were solely determined by the statistical appearance of each collected spectrum. Runs of ten to twenty minutes were generally adequate for the sources used, where the source activity was greater than 1MBq. Only ^{241}Am, with an source activity of 74 kBq, required a longer collection time of approximately 50 minutes.

A 220mm light-guide was fitted between the DEP hybrid photodiode and scintillator. This was originally included to reduce the probability of direct photon interactions with the photodiode and proved to be successful. Including a light-pipe in the arrangement introduced the probability of spectral contamination from Cerenkov radiation. Both ^{55}Fe and ^{241}Am γ-rays (5.9 and 59.6 keV respectively) are below the Cerenkov energy threshold in perspex (178 keV) and both source spectra were unaffected. Cobalt-60 and ^{137}Cs γ-rays (1.173 & 1.332 MeV, and 661.66 keV respectively) are energetic enough to generate Cerenkov emitting electrons. Cerenkov contamination has been reported in such experiments (Crossman, 1997 and Belcher, 1953). However, with the low source activities used, of typically less than 37 MBq, production of Cerenkov radiation was minimal and did not make detectable contributions to each spectrum.

For the low energy γ-rays of ^{55}Fe and ^{241}Am, a 3 mm perspex build-up layer was used. For ^{60}Co and ^{137}Cs γ-rays, this was replaced with a 6 mm perspex build-up layer. Sources were placed tightly against the build-up layer to ensure 2π geometric irradiation of the scintillator, as shown in figure 5.0.

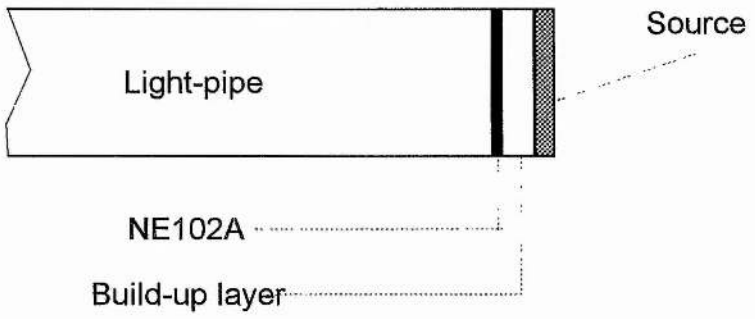

Figure 5.0 Arrangement of perspex build-up layer, NE102A scintillator and source.

5.3 Data Processing

Raw spectral data were collected with an EG&G Ortec 2048-channel 100T MCA and were stored on hard disk. A specially written data algorithm was then used to convert spectrum data from the 8-bit encoded Ortec format into a usable digital format.

5.3.1 Source Geometry

In most cases, the precise geometry of the source, and the radiation field it emits, must be calculated. In this series of experiments, each isotope was in the form of a disk source. These could easily be placed against the face of detector ensuring almost 2π counting. Slight losses were assumed to occur where the field radiated parallel to the face of the disk, however, these losses were assumed to be less than 1% and a 2π approximation was used.

5.3.2 Shielding Out Associated Radiations

Of primary interest in these experiments were the effects of γ-rays on the thin film detector. However, most sources had accompanying α- or β- particle emissions. Normally, these higher LET radiations would loose most of their energy before reaching the detector, however, the close proximity of the source disks to the scintillator would have allowed both α- or β- particles to enter the scintillator.

In the case of associated β-particle emissions, a 2mm nickel disk absorber was inserted between the source disk and detector to ensure they did not add to the spectrum. Gamma-ray emissions from these sources were of sufficiently high energies

that the absorber had a negligible effect on photon fluence. With α-particle sources, a 75 μm thick cellulose-based absorber was used. While effectively absorbing the α-particles, it imposed no appreciably attenuation of the associated lower energy X- and γ-rays.

Under α- or β-particle irradiation in the absence of any absorber medium, the collected spectrum appears as though superimposed upon a typical energy distribution spectrum. This became particularly evident when the spectrum continuum was investigated as a by-product of the data extraction process. Figure 5.1 shows the β-particle contribution to a collected ^{137}Cs spectrum, illustrating the need for shielding.

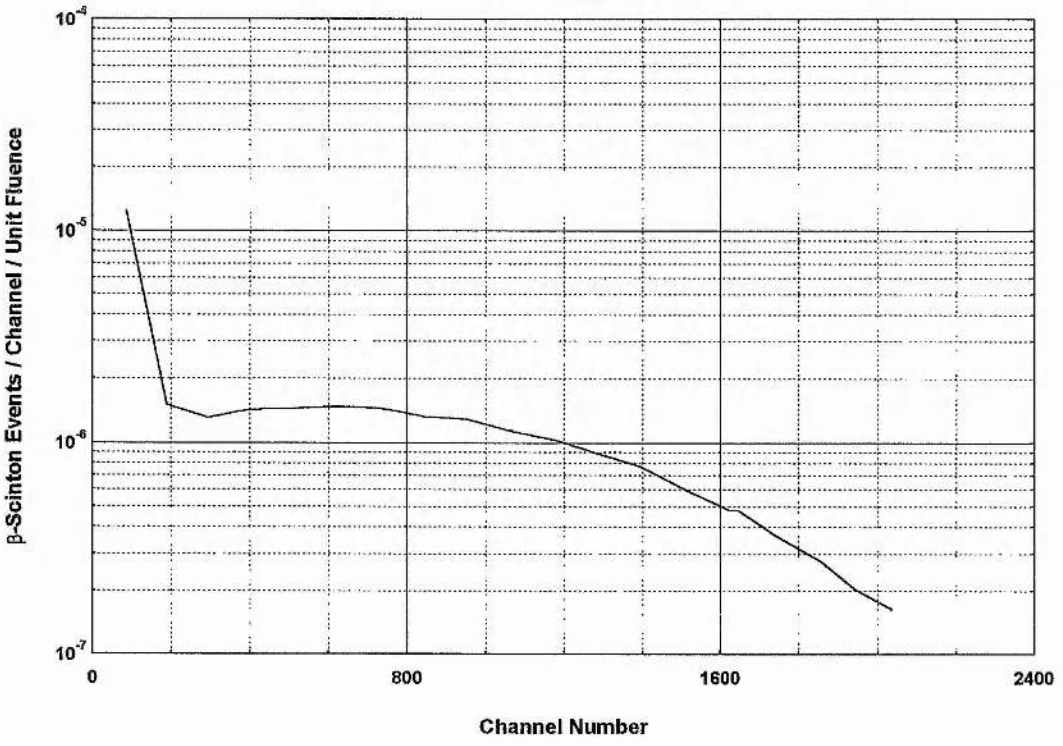

Figure 5.1 β-particle contribution to a ^{137}Cs scinton spectrum.

5.3.3 Background Stripping

In conventional spectroscopy applications, the removal of the background continuum is generally the preferred background stripping method. Knoll (1986) suggests that for multi-peak spectra, the background continuum must be fully subtracted before any evaluation can be made. Unlike the simple subtractive background stripping method, which accounts only for the removal of spurious radiation effects from the surrounding environment, subtracting the continuum also accounts for a series of complex interactions in both the phosphor and the light-pipe, and in the detector itself. This approach generally offers much greater flexibility and only one run per source is required.

This approach is unsuitable when dealing with DEP hybrid photodiode spectra, since the continuum method assumes that the continuum is of a predictive exponential or quadratic form. However, the Hybrid background spectrum is superimposed with several photon peaks. The more conventional background subtraction method is therefore required.

By removing the scintillator from the experimental arrangement and running the detector with the source in place, all likely spurious-photon causing events would be collected in the spectrum but without any contribution from the scintillator. By then replacing the scintillator and repeating the run, a spectrum containing all unwanted counts and the wanted scinton events would be collected. Scaling both spectra to ensure live-time parity, and subtracting the former from the latter then gives a spectrum containing only scinton events.

However, in practice, the subtraction of a background spectra often resulted in the scinton spectrum containing negative peak areas. This anomalous behaviour was

related to an unstable noise characteristic of the DEP hybrid photodiode which became evident when the system was powered down to insert or remove sources and the scintillator. When power was re-established, unpredictable electronic noise was present. Taking a background spectrum prior to the source run merely shifted the noise uncertainty from the background to the scinton spectrum. Taking two background and two source spectra in alternate order, then averaging the data sets, provided the best solution and was the principal method used throughout.

5.3.4 Data Reduction Processes

As the proposed model of nanoscintometry derives fundamental biological damage data from the numbers of plural scinton events, it is essential that the maximum number of photo-electron peaks be resolved. This allows the extraction of uncorrelated scinton data, in the $k > 2$ peaks, which can be used to test the validity of the model. In most cases, up to five peaks can be readily resolved without the need for signal processing. However, with application of various statistical smoothing algorithms, such as the *5-point kernel* in equation 5.1, up to twelve peaks could be resolved.

$$x_n = \frac{1}{5}\sum_{i=n-2}^{n+2} x_i \qquad (5.1)$$

A detailed discussion of the statistical models applied to the data is given in Appendix A. Generally, employing such kernels for signal processing will cause minor alterations in total peak areas. These change haves been estimated at less than 0.001% and are considered to be insignificant.

5.4 Detection Efficiencies

As a numerical measure of induced biological damage is extracted from theory from the number of paired spatially correlated scinton events, it is essential that an accurate count of these events be made. Event sizes are subject to the inefficiencies of the detector. To obtain accurate scinton yields for individual irradiations, all loss mechanisms in the detector must be identified and taken into account. Accounting for the various efficiencies and losses within the system is therefore critical.

Intrinsic overall detector efficiency is determined by three properties: the quantum efficiency of the photocathode, the photon transport efficiency of the light-pipe and the scinton production probability in the scintillator.

5.4.1 Quantum Efficiency

The quantum efficiency, η, of a photocathode is an energy response function and defines the efficiency with which incident photons are converted into photoelectrons. The function is wavelength dependent and is optimised when matched with the incident photon spectrum. Quantum efficiency may be expressed as a single mean probability over a specific range of wavelengths, or as a wavelength-efficiency plot. The quantum efficiency of the PP0275A bialkali DEP hybrid photodiode photocathode is 25% at 400nm and 20% at 440nm (DEP, 1996). The wavelength quantum efficiency function for the detector is shown in Figure 5.2.

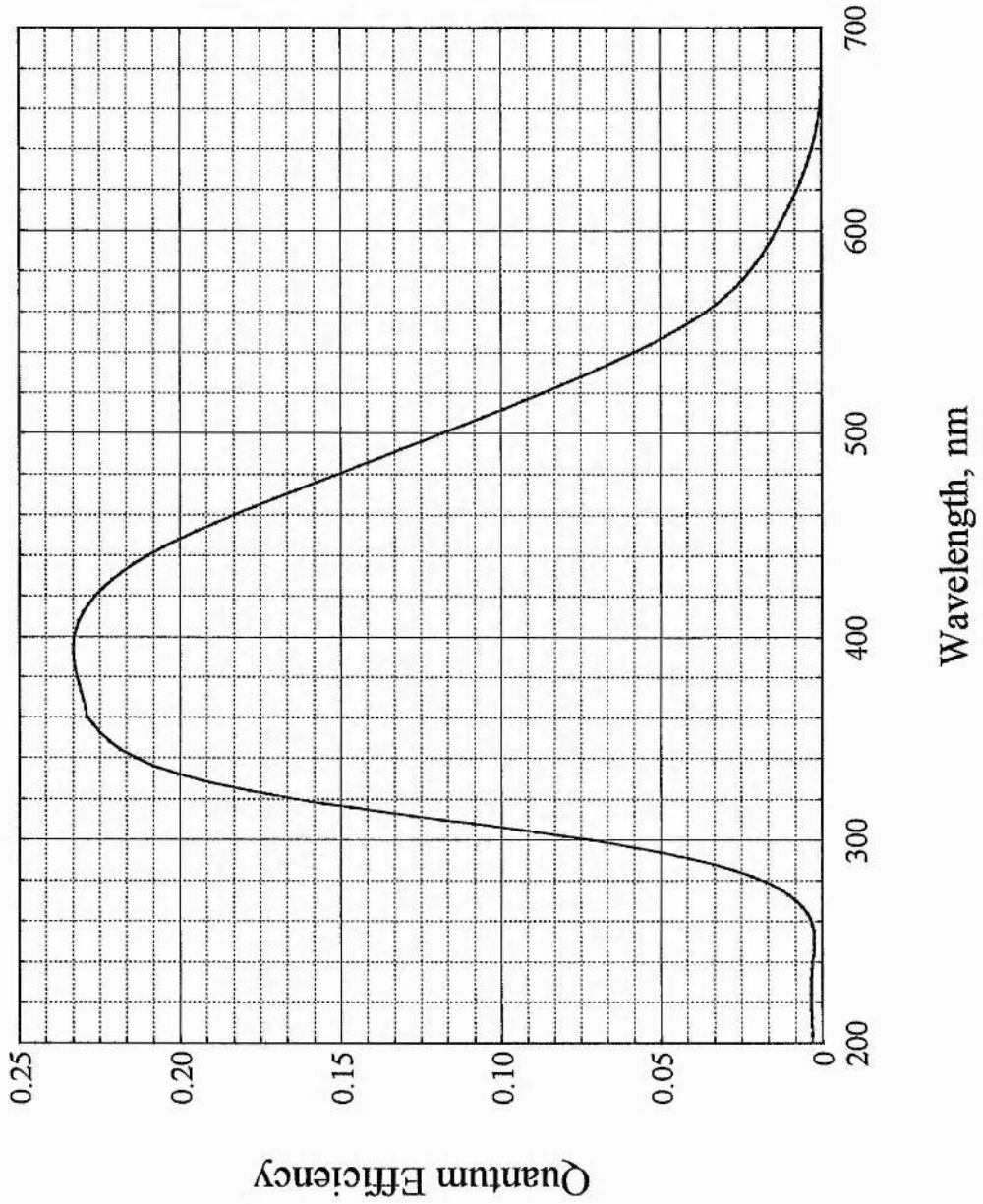

Figure 5.2 Quantum Efficiency of the DEP HPD Photocathode (DEP, 1996)

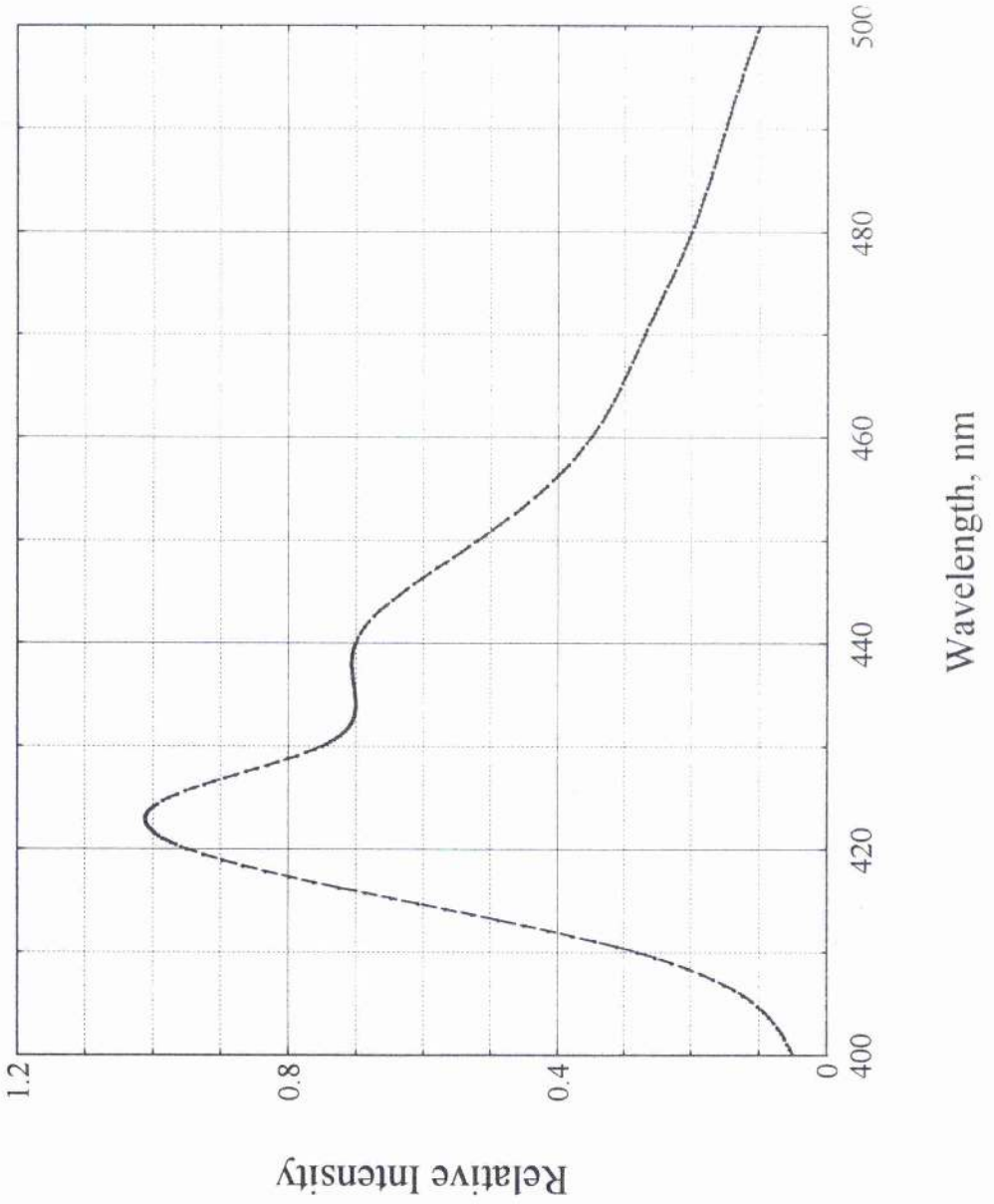

Figure 5.3 NE102A Emission Spectrum (NE Technology, 1995)

The emission spectrum of NE102A is not in a form that can be used directly. It must first be normalised such that the net probability of emission over the entire wavelength range is unity. This may be done by dividing each point by the integral of the spectrum.

The mean quantum response of the photocathode, ε, to the incident spectrum is given by

$$\varepsilon = \int_{\lambda_{min}}^{\lambda_{max}} \frac{p(\lambda)}{k} . \eta(\lambda) . d\lambda \qquad (5.2)$$

where $\eta(\lambda)$ is the quantum efficiency at wavelength, λ,

$p(\lambda)$ is the relative emission intensity of the scintillator at wavelength, λ, and

k is the photon fluence normalisation constant given by

$$k = \int_{\lambda_{min}}^{\lambda_{max}} p(\lambda) . d\lambda \qquad (5.3)$$

From Equation 5.2, the mean quantum response of the DEP hybrid photodiode photocathode under illumination by the NE102A plastic scintillator was found to be 0.207 photoelectrons per incident scinton.

5.4.2 Photon Transport Efficiency

The efficiency with which photons are transported from the scintillator to the photocathode through a Perspex light-pipe is conventionally estimated by the exponential absorption law, using the photon attenuation coefficient for Perspex of $0.734m^{-1}$ (Tove, 1964). However, the validity of this method is contradicted by experimental findings (Kilvington *et al.*, 1970)

These data suggest that by using exponential attenuation, the calculated fraction of the photons transmitted from the light-pipe of length 1 m is over-estimated by a factor of 1.47. Hence, an alternative method of calculating attenuation of an optical photon fluence is suggested. The method makes use of a Monte Carlo simulation which is discussed in Chapter 4. Results from the Monte Carlo Photon Transport code are in reasonable agreement with experimental photon attenuation data observed by Kilvington *et al.* (1970).

From exponential attenuation law, it is found that the mean probability of a photon being transmitted from a light-pipe of length, l, be given by

$$\alpha = \exp(-\mu.l) \qquad (5.4)$$

where μ is the attenuation coefficient of the medium.

Equation 5.4 predicts that for a Perspex light-pipe of length 0.22m, the transmission probability is 0.85. However, from the Kilvington *et al.* data, this same probability is measured in experiment as 0.58. The Monte Carlo model predicts a probability of 0.51. Both values differ significantly from the value predicted by exponential attenuation.

5.4.3 Intrinsic Detection Efficiency

The intrinsic detection efficiency may be defined as the probability with which a single scinton is detected. Numerically, this is equivalent to the product of photocathode quantum efficiency and mean attenuation of photons in the light-pipe. For this detector configuration, the intrinsic detection efficiency is 0.12.

5.5 Scinton Production Probability

A method of expressing the experimental γ-ray interaction probability with the nanodetector sites in the phosphor is to express absolute scinton yield in terms of the scinton production probability. This parameter is a direct measure of the effectiveness of the incident radiation on the phosphor. The overall scinton production probability is calculated from Nanoscintometry theory, discussed in Chapter 2, and is the integral of the predicted scinton yield.

In conventional spectroscopy, the scinton yield is directly proportional to the integral of the photoelectron spectrum, taking system losses into account. However, in an DEP hybrid photodiode spectrum each consecutive peak contains the number of peak events multiplied by the peak number, i. Therefore, total number of detected events can not be described by the integral of the spectrum. Instead the absolute number of photoelectron events detected, N, in a DEP hybrid photodiode spectrum of k peaks is given by

$$N = \sum_{i=1}^{k} i.n_i \qquad (5.5)$$

where i is peak number, and n_i is the number of detected events in peak i.

And hence, the absolute number of scinton events produced in the phosphor, N_S, is given by

$$N_S = \frac{1}{\alpha.\varepsilon}.\sum_{i=1}^{k} i.n_i \qquad (5.6)$$

where α is the mean transmission probability of scintons from the light-pipe, and

ε is the mean quantum response of the photocathode.

5.5.1 Event Probabilities

In a given radiation field, a source of γ-activity A_0, will produce N_S scinton events per unit time. Correcting the radiation field for the geometry of the source and the geometry of the plastic scintillator, the source γ-activity can be written as

$$A = \frac{dN}{dt}.d\Omega \qquad (5.7)$$

where $d\Omega$ is the solid angle subtended by the plastic scintillator, assuming a point source of radiation, and dN/dt is the γ-activity of the source in 4π per unit time.

From Equation 5.6, we can find the absolute number of uncorrelated scinton events, N_S, in the recorded spectrum. Hence, the total event probability, σ_S, is given by

$$\sigma_S = \frac{dN_S}{dt} \cdot \frac{dt}{dN.d\Omega} \qquad (5.8)$$

Values of total scinton event probability for the various sources used were calculated using Equation 5.8 and are given in Table 5.1 below.

Table 5.1 Scinton event probabilities corrected for intrinsic detector efficiency.

Source	Total Event Probability
^{55}Fe	3.921×10^{-2}
^{60}Co	9.267×10^{-2}
^{137}Cs	3.922×10^{-2}
^{241}Am	6.728×10^{-1}

The unusually high production probability of ^{241}Am was not an anomalous result and reproducibility was possible. However, since the γ-activity of this source was significantly less than that of the other isotopes used, it is suggested that statistical inaccuracies may have led to this high value. From emission data in table 5.3, it is also suggested that the increased probability may be due to the presence of a large gamma-activity of low energy photons between 13 and 17 keV, since the data in Table 5.1 assumed only a contribution from the 59.6 keV emission.

5.6 Direct γ-Photocathode Interactions

Direct photon interactions with the light-pipe, photocathode, photoelectron focusing electrodes and the charge sensitive layer of the collecting diode are all processes which can lead to the production of spurious counts. Lower energy, less penetrating γ-rays, such as ^{55}Fe, were not expected to add significant counts. Higher energy γ-rays from ^{60}Co and ^{137}Cs, however, were observed as having a small effect on collected spectra, typically only 25 - 50 counts per second for a 2.68 MBq ^{137}Cs source. In the experimental arrangement that was used, these events could not be shielded out. In a potential dosimeter, such events could not be protected against.

5.7 Experimental Results

Four main X- and γ-ray sources were used in this series of experiments, giving a wide range of photon energies. Details of these sources are given in Table 5.2 below.

Table 5.2. Physical details of isotopes used. Data from Browne *et al.*, (1986)

Isotope	Source Activity	Half-Life	Branching Ratio	Photon Energy
^{55}Fe	1.37 MBq	2.73 years	0.162	5.9 keV
^{60}Co	970 kBq	5.721 years	0.999	1173 keV
	970 kBq		0.9998	1332 keV
^{137}Cs	2.68 MBq	30.0 years	0.8521	661.66 keV
^{241}Am	74 kBq	432.7 years	0.357	59.6 keV

Table 5.3. Principal X- and γ-ray emissions of isotopes used. Data from Browne *et al.*, (1986) and ICRP 38 (1983)

Isotope	Emission	Energy	γ-Activity
^{55}Fe	Mn $K_{\alpha 2}$	5.888 keV	8.36%
	Mn $K_{\alpha 1}$	5.899 keV	16.6%
	Mn $K_{\beta 1}$	6.490 keV	2.22%
	Mn $K_{\beta 3}$	6.490 keV	1.13%
^{60}Co	γ	1173.237 keV	99.90%
	γ	1332.501 keV	99.9824%
^{137}Cs	Ba $K_{\alpha 2}$	31.817 keV	2.05%
	Ba $K_{\alpha 1}$	32.194 keV	3.77%
	Ba $K_{\beta 1}$	36.357 keV	1.04%
	γ	661.660 keV	85.21%
^{241}Am	Np L_{α}	13.927 keV	24.4%
	Np L_{β}	17.51 keV	30.5%
	Np L_{γ}	20.98 keV	7.31%
	γ	26.3445 keV	2.4%
	γ	59.5364 keV	35.7%

Using the single detector arrangement discussed in Chapter 3.3, the four scinton spectra, shown in Figures 5.4 to 5.7, were collected. These figures illustrate unprocessed raw data. In Figures 5.8 to 5.11 the same data are show with the background having been removed. Subsequently, in Figures 5.12 to 5.15, the same spectra have been processed by statistical smoothing with Gaussian distributions fitted to each scinton peak. Extracted data from each of the fitted spectra are tabulated in Tables 5.4 to 5.7, and are plotted in figure 5.16.

Table 5.4 ^{55}Fe. Irradiation of 20μm NE102A film with a 3mm build-up layer. Collection time 847 seconds.

Peak No.	Peak Centroid	Peak Height	Peak Width	Count/ Fluence	Peak Ratio
1	126.657	4.057E-04	112	1.744E-02	1
2	240.611	1.429E-06	102	5.742E-05	3.292E-03
3	349.802	2.177E-07	107	9.658E-06	5.538E-04
4	461.725	7.266E-08	127	3.597E-06	2.063E-05
5	568.963	2.595E-08	98	1.005E-06	5.763E-05
6	677.015	2.644E-08	145	1.156E-06	6.628E-05
7	783.198	1.231E-09	109	7.343E-08	4.210E-06
8	899.315	3.404E-09	113	1.102E-07	6.319E-06

Table 5.5 ^{60}Co. Irradiation of 20μm NE102A film with a 6mm build-up layer. Collection time 727.5 seconds.

Peak No.	Peak Centroid	Peak Height	Peak Width	Count/ Fluence	Peak Ratio
1	127.346	1.694E-04	103	7.268E-03	1
2	239.108	2.910E-05	112	1.258E-03	1.731E-01
3	349.292	6.235E-06	111	2.711E-04	3.730E-02
4	459.497	1.509E-06	111	6.718E-05	9.243E-03
5	569.982	4.845E-07	108	2.258E-05	3.107E-03
6	679.998	2.151E-07	112	1.027E-05	1.413E-03
7	791.534	9.937E-08	111	5.080E-06	6.990E-04
8	905.064	6.067E-08	119	3.219E-06	4.429E-04
9	1018.968	2.503E-08	116	1.194E-06	1.643E-04
10	1127.159	1.487E-08	102	8.209E-07	1.129E-04
11	1235.166	1.290E-08	128	6.687E-07	9.201E-05

Table 5.6 ^{137}Cs. Irradiation of 20μm NE102A film with a 6mm build-up layer. Collection time 663 seconds.

Peak No.	Peak Centroid	Peak Height	Peak Width	Count/ Fluence	Peak Ratio
1	126.755	7.817E-05	103	3.321E-03	1
2	239.167	7.795E-06	111	3.378E-04	1.017E-01
3	349.579	2.155E-06	110	9.592E-05	2.888E-01
4	459.767	8.992E-07	109	4.071E-05	1.266E-02
5	569.772	4.248E-07	114	1.998E-05	6.016E-03
6	680.865	2.356E-07	108	1.097E-05	3.303E-03
7	790.072	1.199E-07	117	5.765E-06	1.736E-03
8	900.967	7.013E-08	109	3.274E-06	9.858E-04
9	1011.717	3.130E-08	121	1.308E-06	3.939E-04
10	1120.604	2.140E-08	107	8.074E-07	2.431E-04
11	1236.866	1.194E-08	139	5.192E-07	1.563E-04

Table 5.7 ^{241}Am. Irradiation of 20μm NE102A film with a 3mm build-up layer. Collection time 2815.6 seconds.

Peak No.	Peak Centroid	Peak Height	Peak Width	Count/ Fluence	Peak Ratio
1	125.216	1.506E-03	104	6.317E-02	1
2	239.120	3.811E-05	103	1.662E-03	2.631E-02
3	347.848	2.097E-05	107	9.425E-04	1.492E-02
4	457.652	1.311E-05	113	6.148E-04	9.732E-03
5	567.710	8.262E-06	114	4.037E-04	6.391E-03
6	679.039	5.524E-06	112	2.834E-04	4.486E-03
7	787.586	4.615E-06	106	2.200E-04	3.483E-03
8	895.938	2.632E-06	108	1.323E-04	2.094E-03
9	1006.245	1.564E-06	115	9.111E-05	1.442E-03
10	1122.860	1.103E-06	114	7.328E-05	1.160E-03
11	1228.752	1.033E-06	107	6.446E-05	1.020E-03
12	1325.501	6.730E-07	109	3.200E-05	5.066E-04

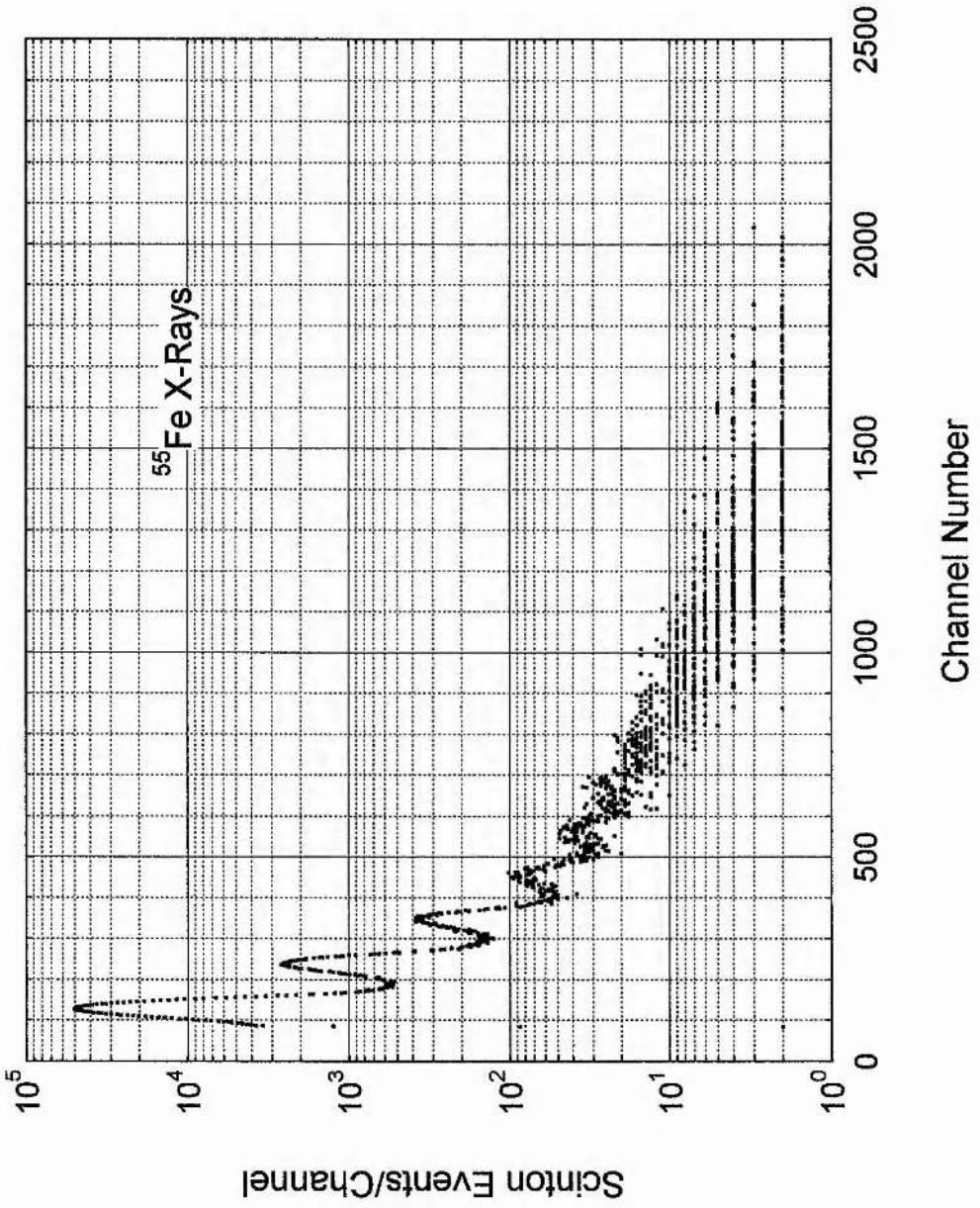

Figure 5.4 Raw ^{55}Fe scinton spectrum.

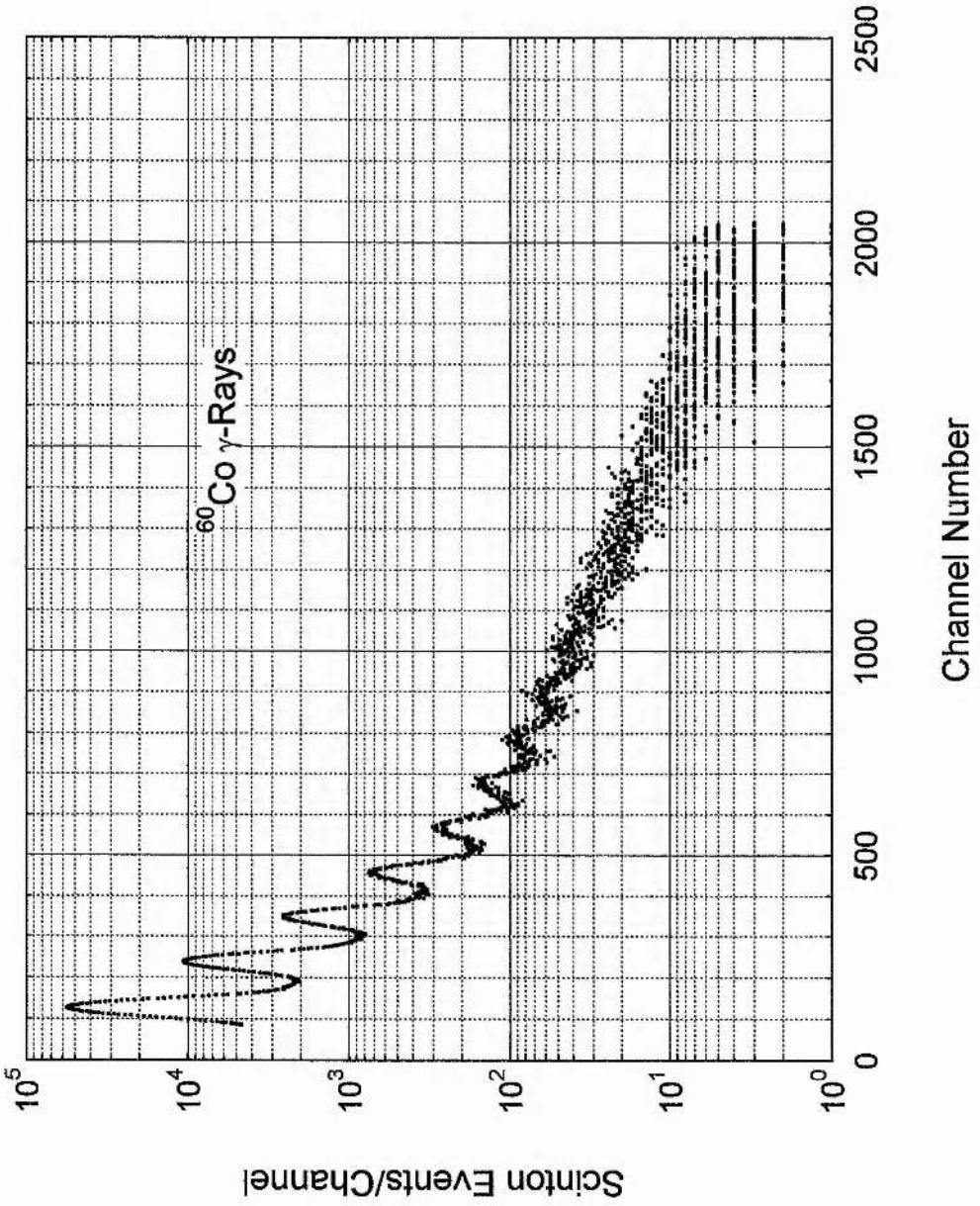

Figure 5.5 Raw ^{60}Co scinton spectrum.

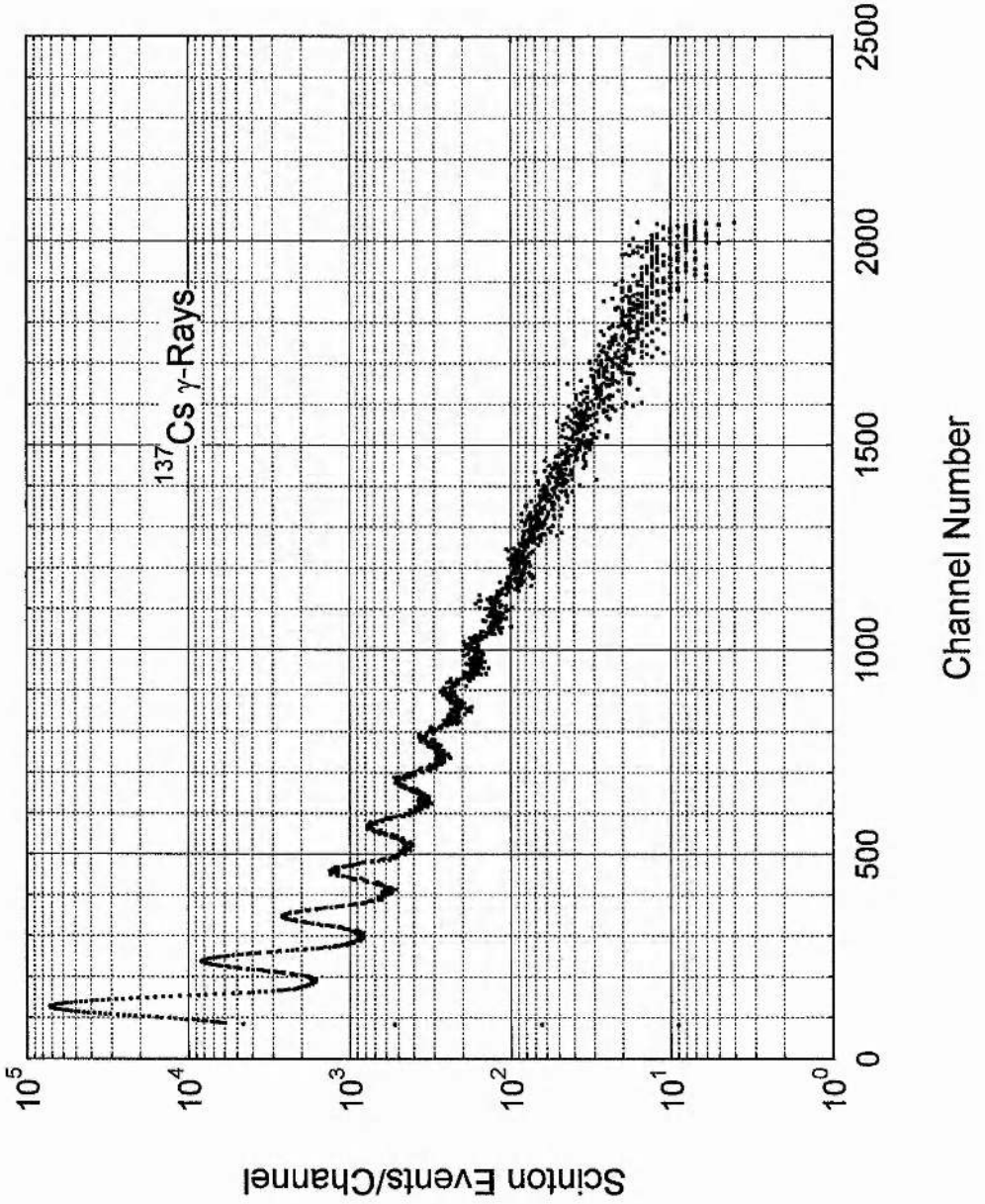

Figure 5.6 Raw ^{137}Cs scinton spectrum.

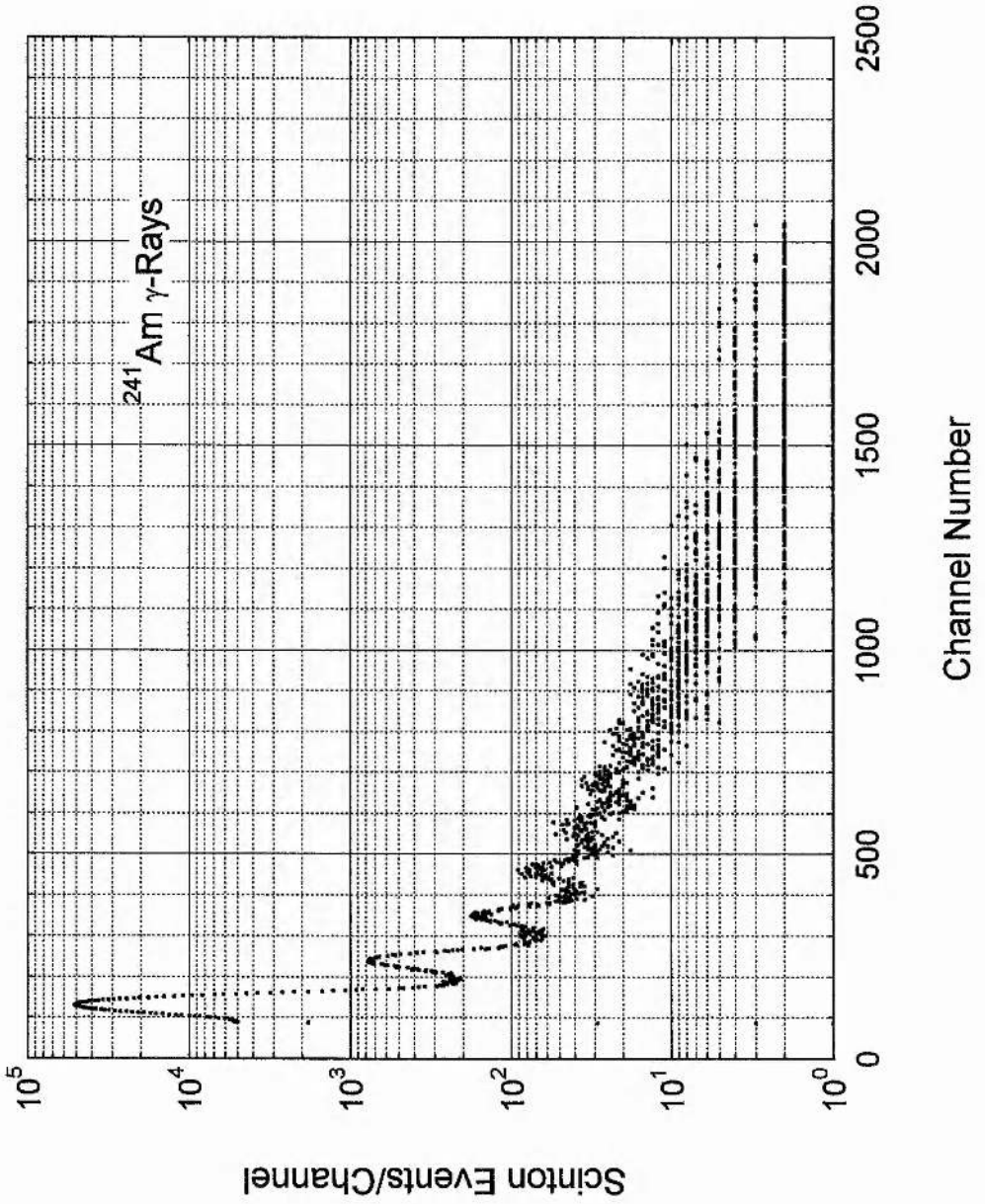

Figure 5.7 Raw ^{241}Am scinton spectrum.

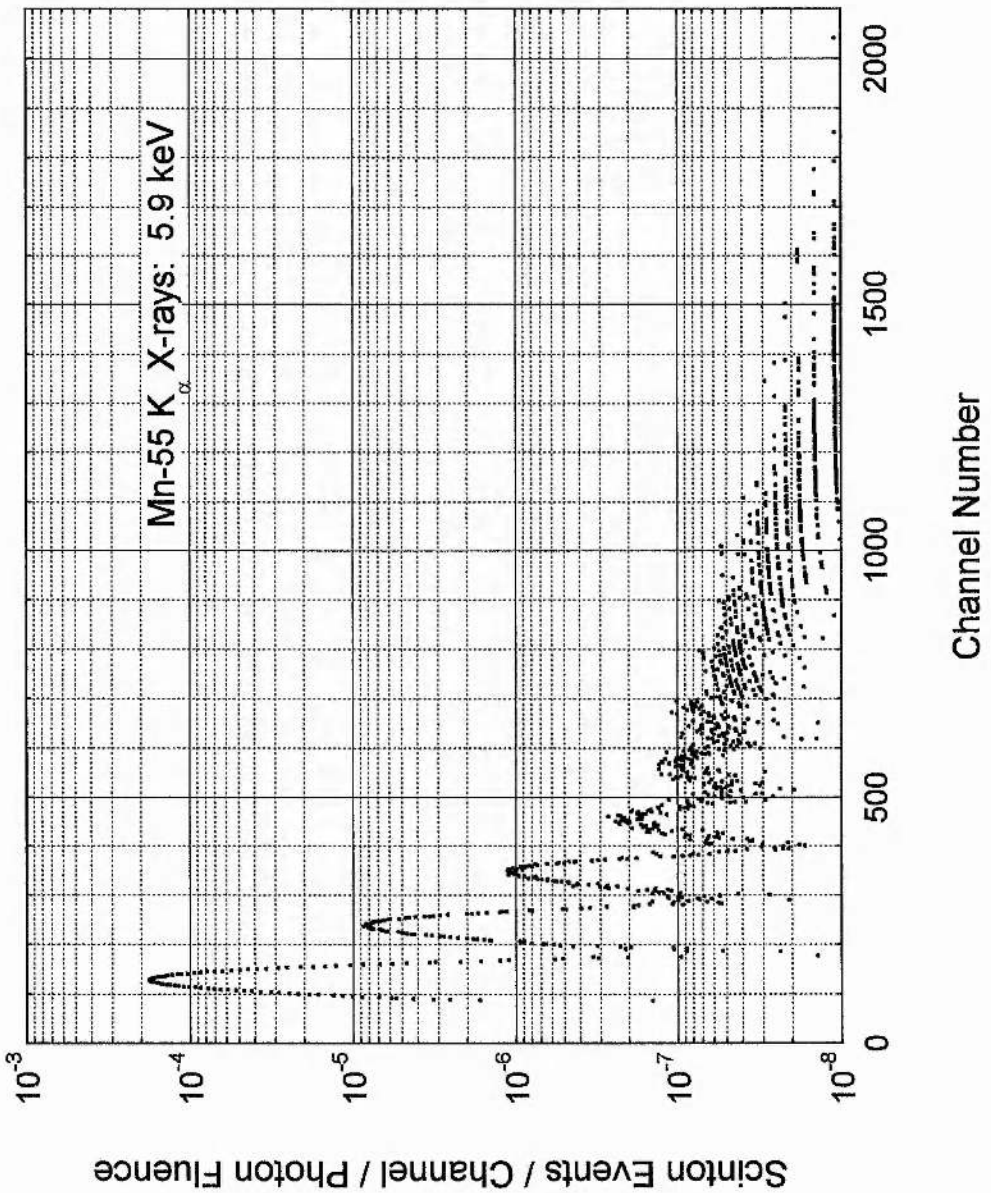

Figure 5.8 ^{55}Fe scinton spectrum with background removed.

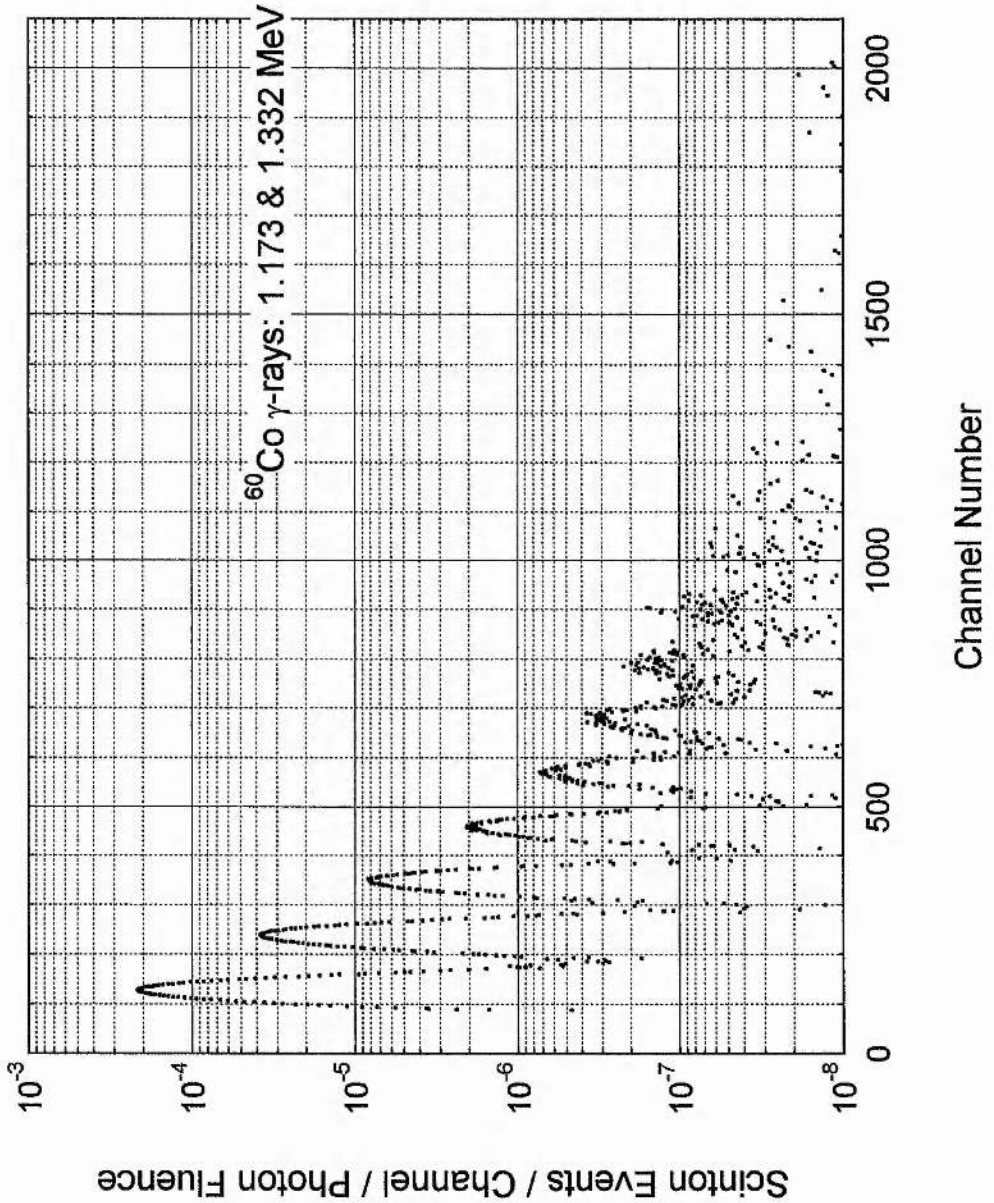

Figure 5.9 ^{60}Co scinton spectrum with background removed.

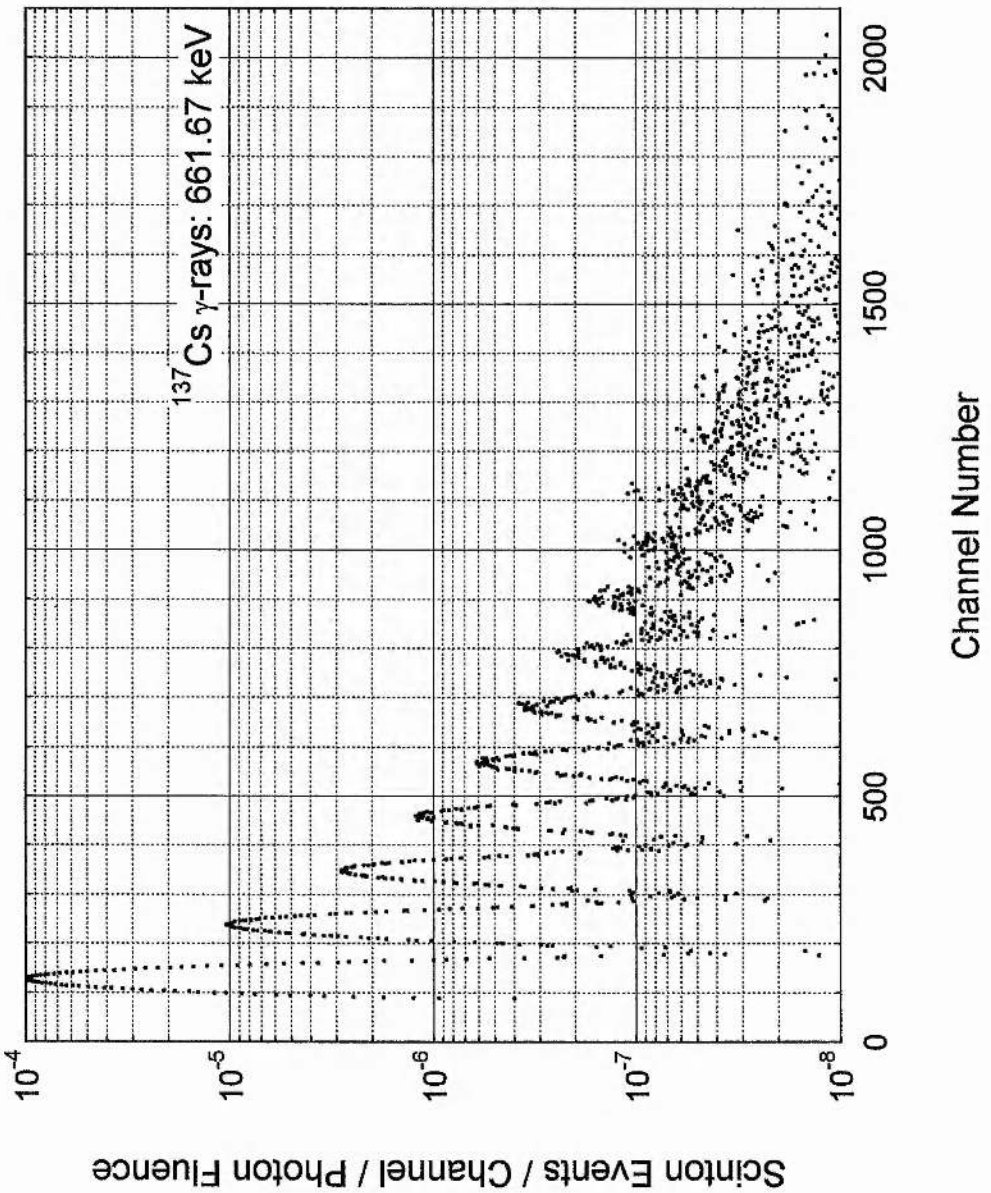

Figure 5.10 ^{137}Cs scinton spectrum with background removed.

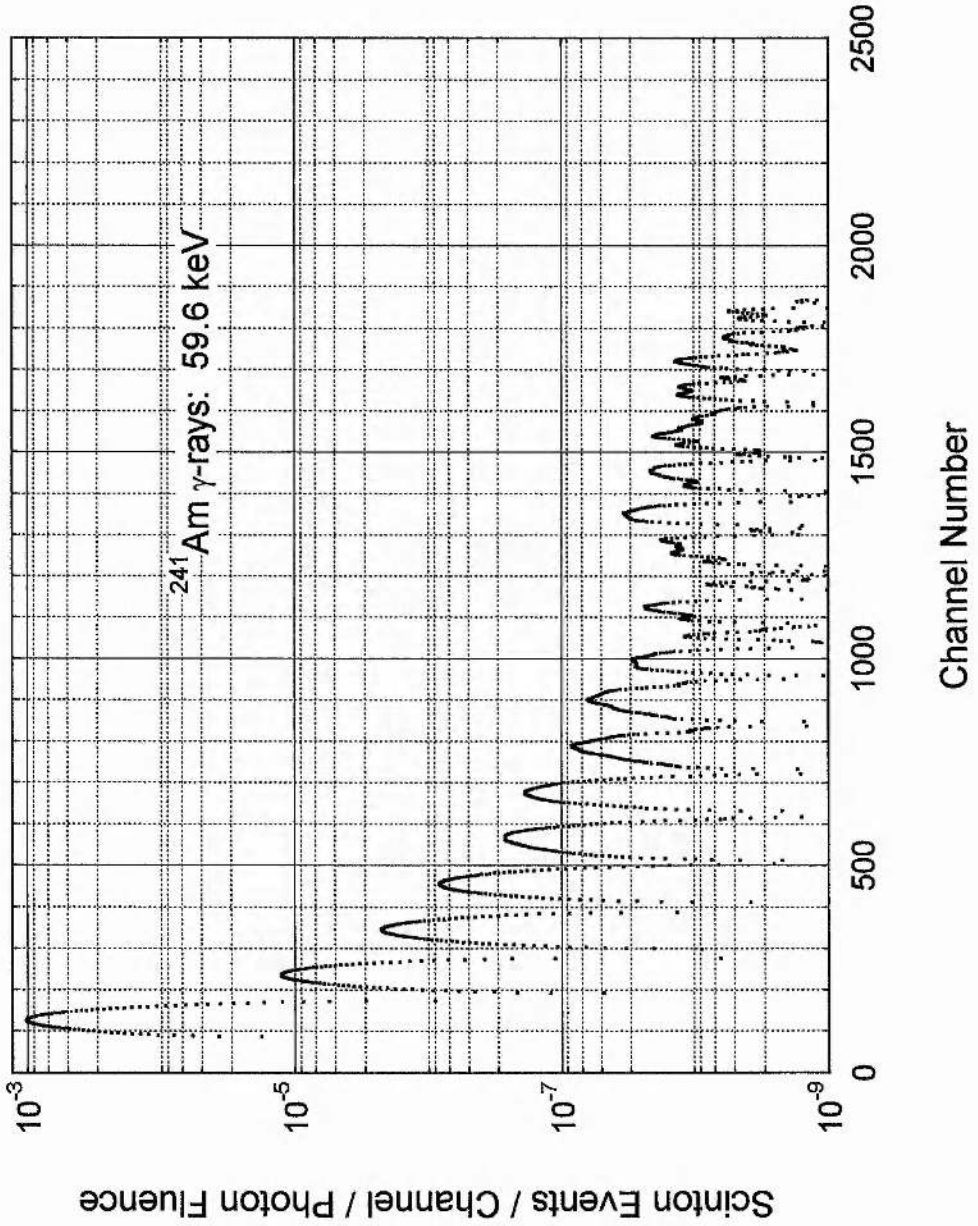

Figure 5.11 ^{241}Am scinton spectrum with background removed.

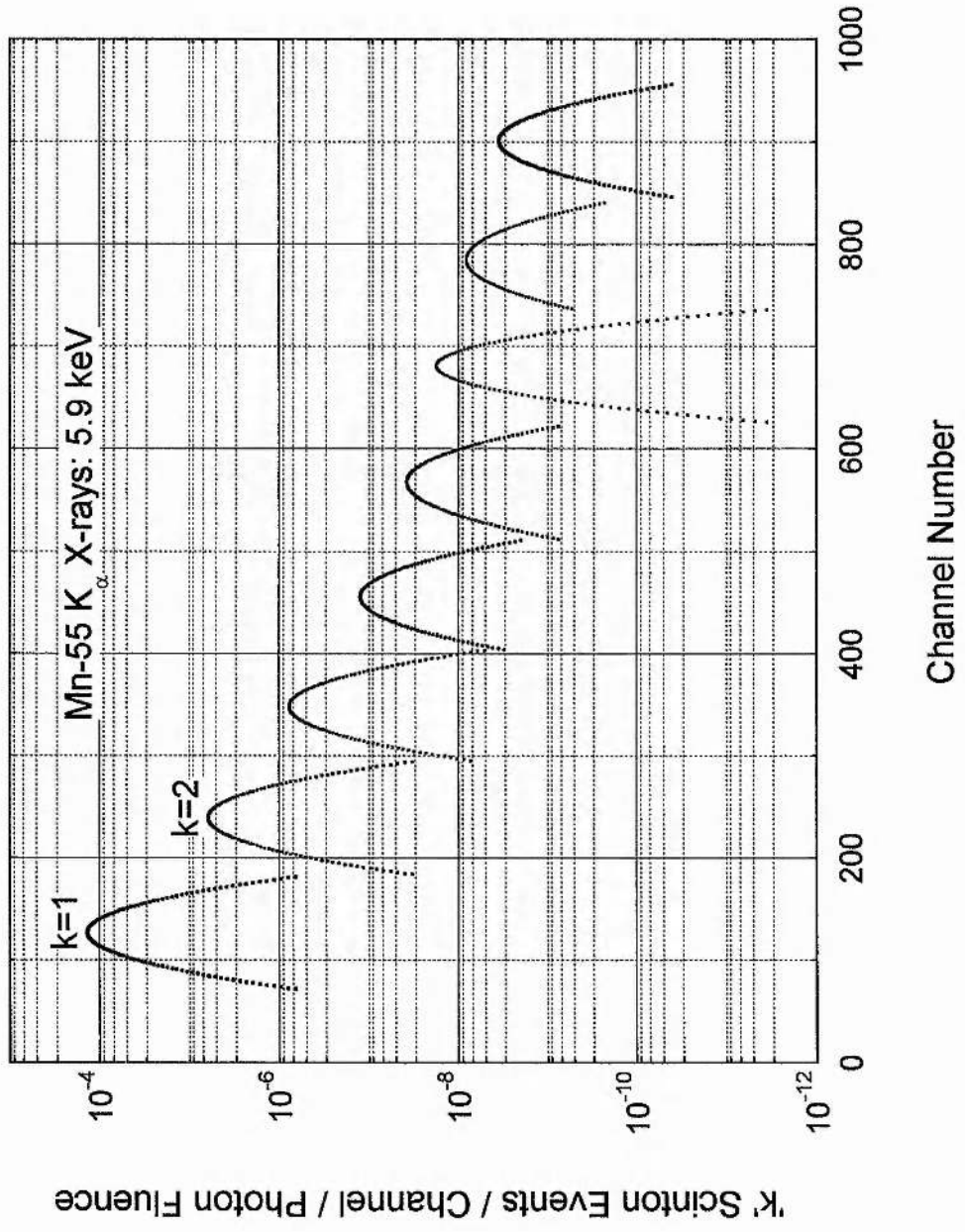

Figure 5.12 Processed ^{55}Fe scinton spectrum with fitted Gaussian curves.

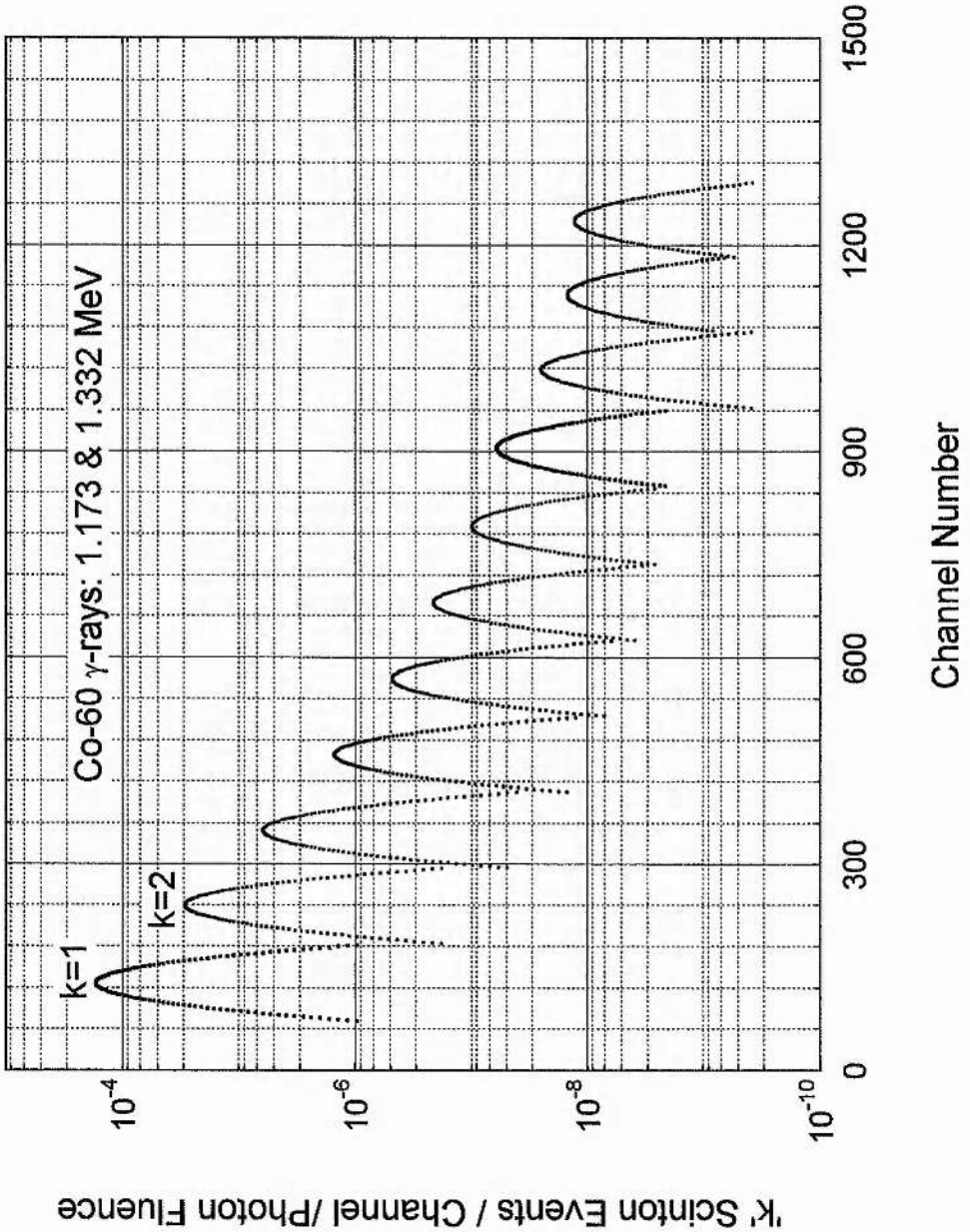

Figure 5.13 Processed ^{60}Co scinton spectrum with fitted Gaussian curves.

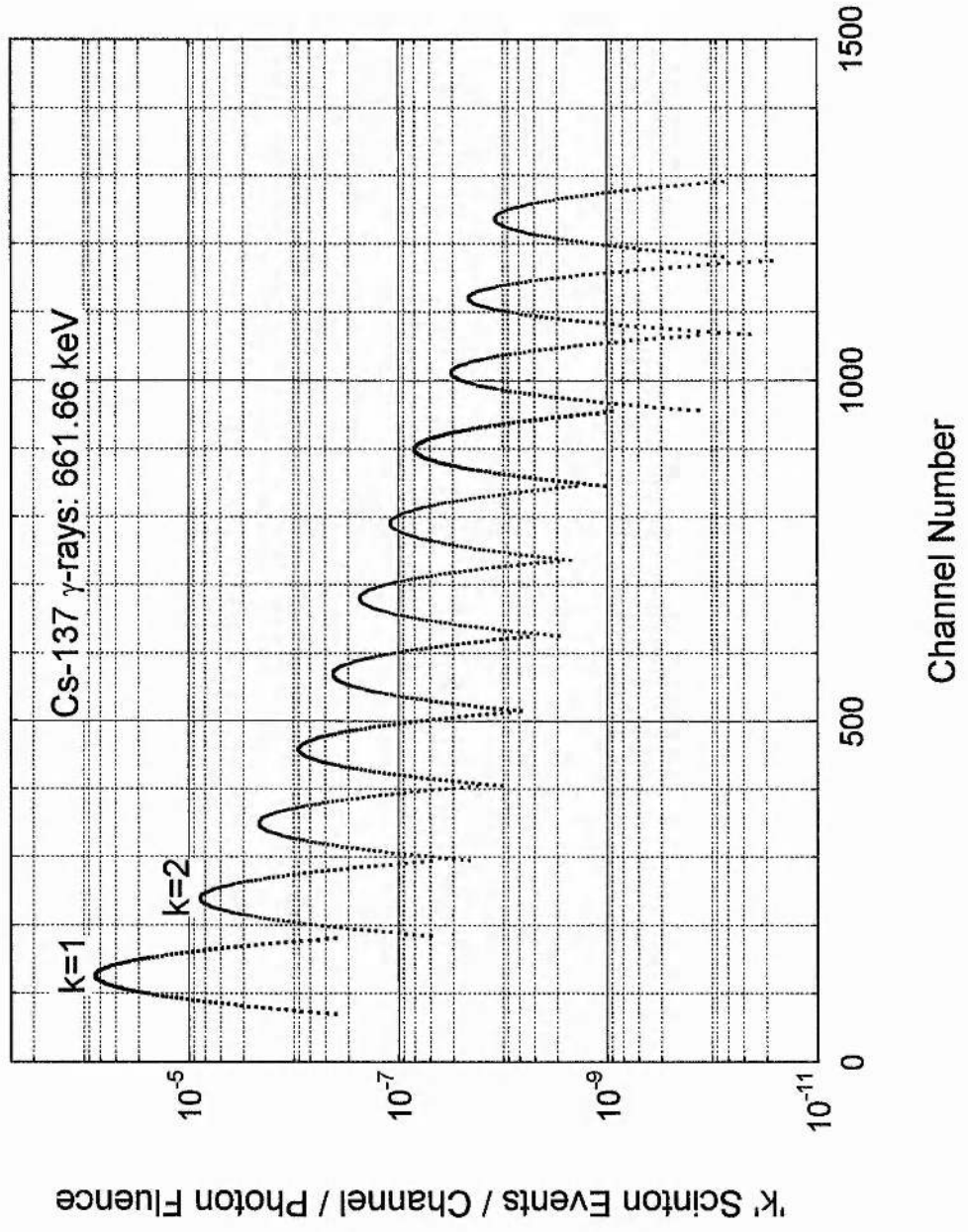

Figure 5.14 Processed ^{137}Cs scinton spectrum with fitted Gaussian curves.

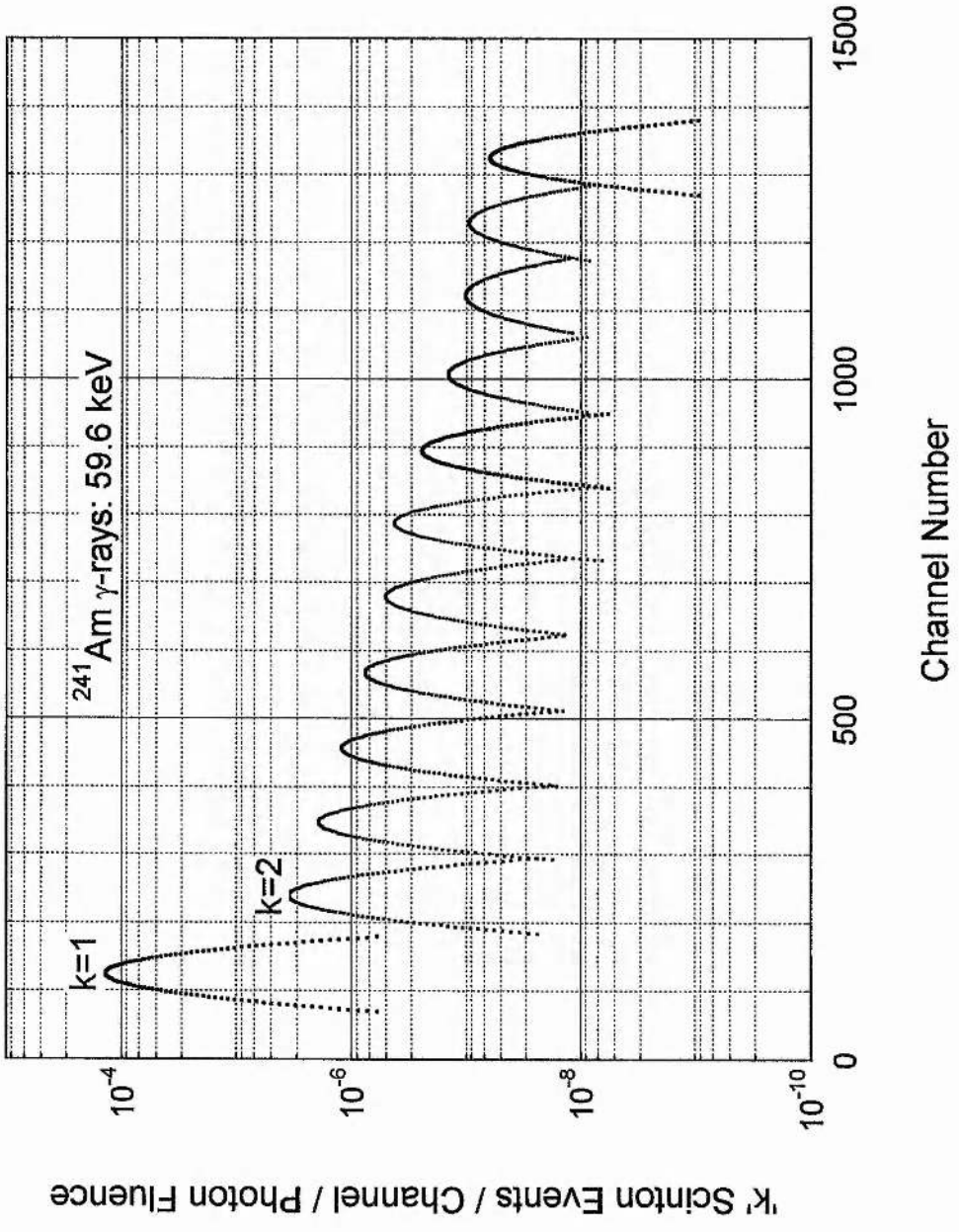

Figure 5.15 Processed ^{241}Am scinton spectrum with fitted Gaussian curves.

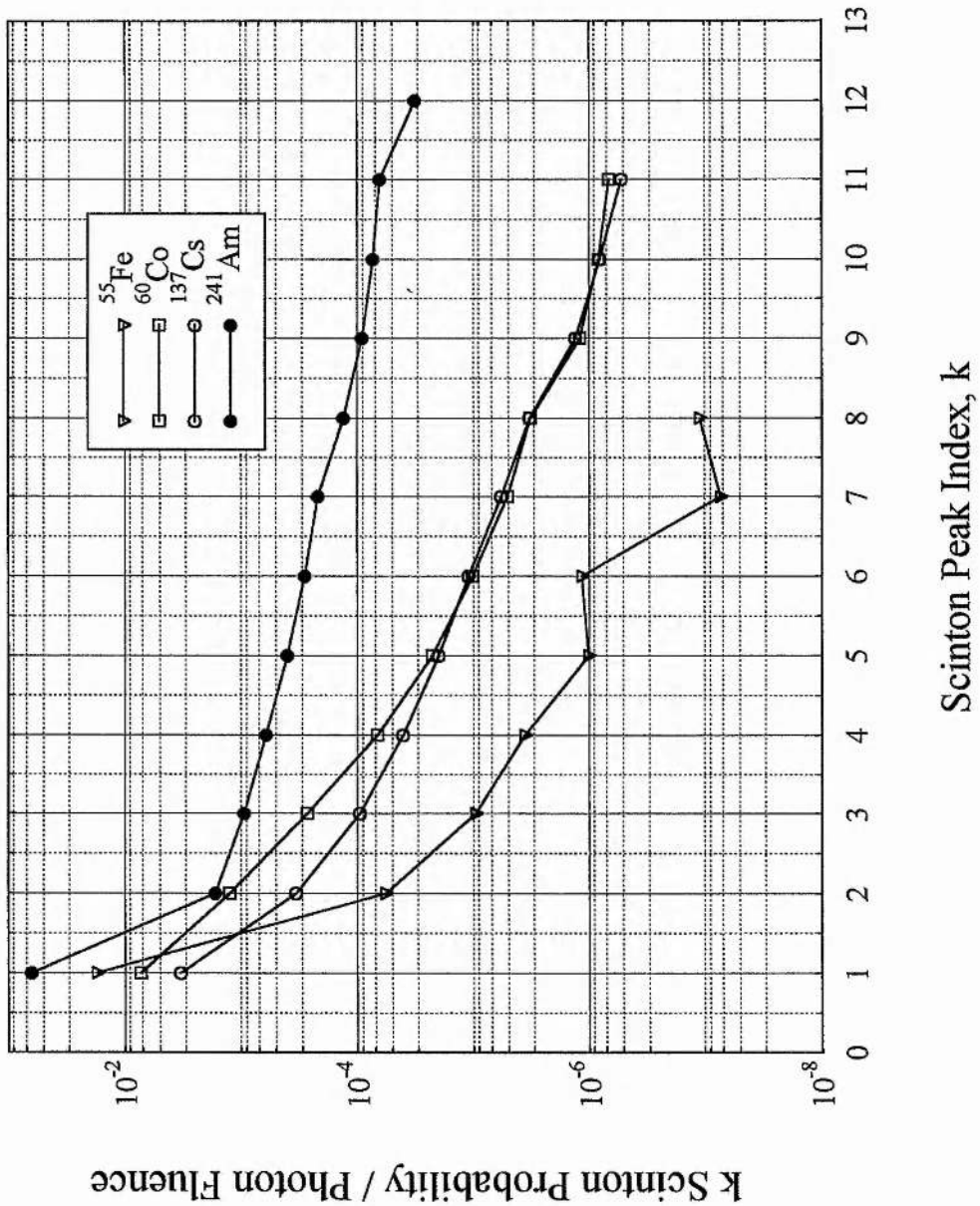

Figure 5.16 Combined scinton event probabilities.

5.8 Interpretation of Results

If the scinton production cross-section, σ_S, for scinton events k = 1, 2, 3,....n, can be deduced from scinton spectra then it is suggested that this data can provide an indirect measure of the response of mammalian cells to irradiation in the same radiation field.

Using the scintillation model discussed in Chapter 2 and applying the associated probability model, it is possible to calculate the scinton response function of the scintillator, and from this, the likely number of single and double events at the requisite 2 nm spacing. To obtain the bio-effectiveness, it is necessary to measure the number of equivalent double-strand breaks. Extraction of paired events is not straightforward as there are co-variant effects in the statistical analyses. Consequently techniques must be developed to accomplish this. However, at this stage, no technique has been developed to allow this extraction to be made.

5.8.1 Collected Spectra

The collected spectra in figures 5.4 to 5.7 illustrate the unique response of a 20μm thin film NE102 scintillator to sparsely ionising radiations. At this thickness of film, the spectrum is no longer composed on the classical energy-deposition profile of γ-ray spectroscopy spectra, but rather is a measure of the yield of individual photon interactions with fluor molecules.

From the Nanoscintometry model discussed in Chapter 2, it is found that each individual scinton peak is constructed of a variety of multiple events. For example, the $k = 3$ scinton peak will contain contributions of three singles, a single and a double, or a triple event. Similarly, the key $k = 2$ peak will contain contributions

from a double or two single events. Therefore, for an accurate interpretation of the biological-effectiveness of these spectra to be made, the correlated double event contribution must be extracted primarily from the $k = 2$ peak for double strand break data, and from other peaks ($k > 2$) as a numerical check of the validity of the model and the collection process.

In equation 2.51, the probabilities of paired spatially correlated events contributing to scinton peaks $k \geq 2$ are given. The probability function is strongly dependent upon the factor products, $g_1 h_0$ and subsequent g_n (double event) and h_n (single event) probability coefficients. In its current form, this product cannot be evaluated without further development of the model, and as such no, significant bio-effectiveness can be reliably extracted from collected spectra.

5.9 Detection Difficulties

Various detection difficulties were noted during this series of experiments. Principal of these was the difficulty in obtaining repeatable results with a high degree of statistical consistency. Most experiments carried out fell within the acceptable margins of expected experimental errors, but several areas were identified that made accurate reproducibility difficult.

The major cause of this inconsistency was the need to remove and replace the scintillator in order to obtain background spectra containing all non-scinton events, such as Cerenkov production in the light-pipe and direct photon interactions with the photodiode and photocathode.. This process involved switching off the power supply and opening the detector, which caused the photocathode to be unavoidably exposed to the ambient level of laboratory lighting. Although great care was taken to

ensure that the laboratory was in almost total darkness when this was done, the photocathode was nevertheless activated resulting in spurious counts. When the power was switched on again, the detector displayed a period of high noise which decreased with time. The product of both effects led to difficulties in reproducibility.

It is suggested that the apparatus would benefit from an electronic LCD shutter mechanism which would allow non-scintillation backgrounds to be taken without the need to remove the scintillator.

This problem was further compounded by inherent noise problems within the detector which became progressively more prevalent over time, and ultimately led to the cessation of experiments while a replacement device was found. This problem was never resolved.

Chapter VI

Photomultiplier Calibration Using Cerenkov Radiation

6.1 Introduction

In this chapter, an alternative method of gain calibration of a photomultiplier tube (PMT) is suggested. The method is based upon the detection of a known intensity of the Cerenkov continuous spectrum. Rigorous theoretical treatments of Cerenkov production allow photon yields to be calculated with high accuracy and thus provide an effective method of precise gain determination

To use a photomultiplier in quantitative photon counting applications it is essential that the number of primary photons incident on the photocathode be accurately known. For this to be made possible, the intrinsic electronic gain of the photomultiplier tube must be known with sufficient accuracy. While PMTs are supplied by manufacturers with documentation indicating approximate gain data at different operating voltages, confirmation of this data and precise calibration by the end user in a laboratory setting have never been readily accessible. A review of a wide range of literature on both scintillation detection methods and photomultipliers and their design failed to reveal any procedure for PMT calibration other than those dedicated systems, such as white light tungsten filament illumination (EMI Electron

Tubes, 1995) used by manufacturers. It was therefore necessary to derive a suitable method and design appropriate equipment to enable this calibration to be carried out.

Photomultiplier gain calibration requires a weak light source of known intensity to be directed onto the photocathode to liberate a proportionate number of photoelectrons. If the individual gains of all other in-line equipment are known and the final amplified output signal is measurable, it is theoretically possible to obtain the internal PMT multiplication factor and therefore the operating gain.

In the associated experiments for the detection of very low yield or even single photon events, experimentally obtainable light levels were anticipated to be at least two orders of magnitude lower than those levels generally available in scintillation experiments. It was therefore desirable that some experience be obtained in operating at such low light levels as well as in the gathering of low yield events. The sensitivity and published gain values (EMI Electron Tubes, 1995) confirmed that indeed a low intensity light source would be experimentally beneficial and would prevent any saturation damage to the photocathode or dynode chain. The high photo-sensitivity of the photocathode precluded the use of any standard light source due to the likelihood of saturation and the inherent dangers to the equipment of overexposure, and with energy requirements of less than 1 pW, the use of a laser was also ruled out. To meet the extremely low light intensity requirements of the calibration, it was determined that the most appropriate light source would be a source of Cerenkov light. Cerenkov light is particularly well suited to this type of calibration as it can be produced with relative ease, has a radiant power and photon yield that can be theoretically calculated with considerable accuracy (Jelley, 1958), has a well-defined spectral distribution and is of constant intensity, though generally a factor of between ten and one hundred times weaker than scintillation events.

Cerenkov light also has the benefit of emitting the highest proportion of its light in the blue region of the spectrum.

The PMT to be calibrated was the EMI model 9235QB, a high performance PMT designed for use in low light level applications such as photon counting and liquid scintillation counting (EMI Electron Tubes, 1995). The PMT was fitted with a 52mm diameter fused Quartz window which extended wavelength sensitivity into the ultraviolet region (down to 160nm) of the spectrum and because of low concentrations of naturally occurring ^{40}K, ^{232}Th and ^{238}U in the quartz, also provided low radioactive background counts. Electronic multiplication was provided by thirteen caesiated antimony (Cs-Sb) bialkali dynodes arranged in the linear focus configuration.

Two separate calibration methods were suggested and used. The first involved the collection of several event spectra produced by the Cerenkov source using a Multi-Channel Analyser (MCA), operating the PMT at various voltages over its optimum operating range. The collected spectra were then converted into voltage spectra by the simple relationship between MCA channel number and input signal voltage. The resultant voltage spectra were then numerically integrated to obtain the total collected voltage over the duration of each experiment. A derived model of the PMT gain function predicted that PMT gain should be calculable from this numerical quantity, however this method proved inherently difficult to interpret and was finally abandoned in favour of a more reliable method that provided easier access to calibration data.

The alternative method was to remove all in-line amplification electronics and isolate the PMT so that PMT anode current could be measured directly using an electrometer while the PMT was under Cerenkov illumination. The anode current,

generally of the order of 10^{-9}A, provided accurate indications of system gain and was the favoured calibration method.

6.2 Cerenkov Radiation

Cerenkov light or radiation was first observed by Pierre and Marie Curie in 1910 as a faint blue light being emitted from concentrated solutions of aqueous Radium (Smith, 1965). However it was not until 1934 that Russian physicist Pavel Aleksejevic Cerenkov investigated the causes of this radiation. Three years later in 1937, fellow countrymen Ilya Michajlovic Frank and Igor Jevgenevic Tamm developed a classical electromagnetic theory to explain the phenomenon, and all three were later to receive the 1958 Nobel Prize for Physics for their work.

Cerenkov light is emitted by high energy charged particles travelling through a transparent dielectric medium faster than the phase velocity of light in that medium (Knoll, 1986). For Cerenkov light to be produced the following condition must therefore be satisfied

$$\beta n > 1 \qquad (6.1)$$

where n is the refractive index of the transparent medium and β is the ratio of the velocity of the charged particle to the velocity of light in a vacuum. Cerenkov light is emitted by the charged particle in a cone subtended by the solid angle, θ_C, given by

$$\theta_C = \cos^{-1}(1/n\beta) \qquad (6.2)$$

Since it is generally the case that only particles with high kinetic energy satisfy equation 6.1, it is therefore necessary to describe the particle's velocity in relativistic terms, and the value of β must be corrected accordingly. This correction can be made using the relativistic correction

$$\beta_i^2 = 1 - \frac{1}{(1+\tau)^2} = \frac{2m_0c^2T + T^2}{(m_0c^2T)^2} \qquad (6.3)$$

where T is the kinetic energy of the particle,

m_0 is the rest mass of the particle, and

$\tau = T/m_0c^2$ is the reduced kinetic energy in units of rest mass of the particle.

By substituting equation 6.3 into equation 6.1, we find that the threshold condition for emission of Cerenkov radiation can be expressed relativistically in terms of the particle's kinetic energy. This quantity, known as the Cerenkov Threshold, E_{th}, defines the energy below which all Cerenkov emission ceases.

$$E_{th} = m_0c^2\left(-1 + \sqrt{1 + \frac{1}{n^2+1}}\right) \qquad (6.4)$$

where m_0c^2 is the rest-mass of the charged particle.

The number of Cerenkov quanta, N, emitted within a narrow spectral range λ_1 to λ_2 by a particle passing through a length l of medium is given by

$$N = \frac{4\pi^2 z^2 e^2}{hc} . l . \left(1 - \frac{1}{\beta^2 n^2}\right)\left(\frac{1}{\lambda_1^2} - \frac{1}{\lambda_2^2}\right) \qquad (6.5)$$

This gives typically about 10 photons per mm between 400nm and 600nm for a relativistic electron passing through water (n_D=1.333) (Smith, 1976).

6.3 Cerenkov Source

To satisfy equation 6.1, a source of energetic electrons with a maximum kinetic energy well above the Cerenkov threshold in perspex of 176 keV is required. The source should also be free from associated γ-rays which may lead to the production of secondary high energy electrons by Compton backscattering within the perspex and photocathode. It should have a relatively high specific activity to provide a good yield of photons, and to ensure constant intensity, should have a relatively long half-life (Jelley, 1958).

The most suitable source, which met all these criteria, was a 74 kBq mixed nuclide strontium-90/yttrium-90 source produced by Amersham International (Source Number BZ462). This nuclide combination is particularly suited to Cerenkov production applications as both strontium-90 and yttrium-90 decay essentially by pure β-disintegration. While a pure β-emitter would have been preferred, no such source of suitable activity and energy was available.

Table 6.1. Decay data on the strontium-90/yttrium-90 source (Data from Browne et al, 1986).

Isotope	Half life ($t_{1/2}$)	Decay Constant (λ)
Strontium-90	28.5 years	$7.7121238 \times 10^{-10}$ s^{-1}
Yttrium-90	2.671 days	3.0035705×10^{-6} s^{-1}

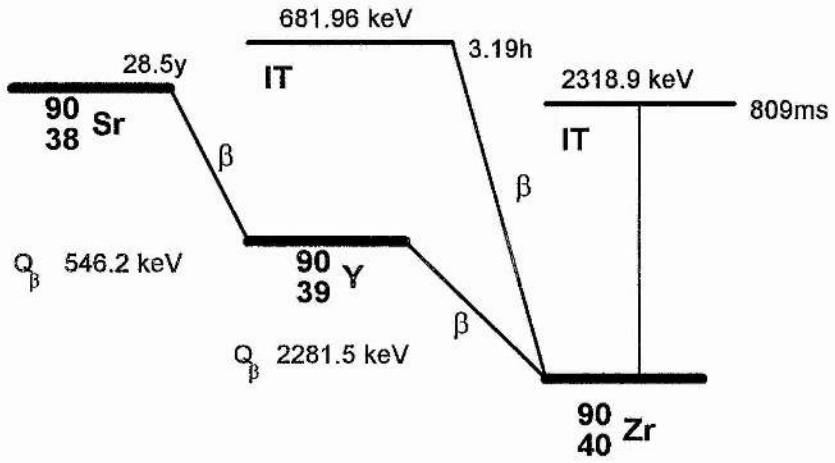

Figure 6.1. The strontium-90/yttrium-90 decay chains (Data from Browne et al. 1986).

6.3.1 $^{90}Sr/^{90}Y$ Secular Equilibrium

In the case of a mixed nuclide source where the half-life of the parent nuclide is far greater than that of the daughter, then the activities of individual daughter nuclides are described in terms of *radioactive* or *secular equilibrium* e.g., (Wehr *et al*, 1984). Under such circumstances, the decay of the shorter lived daughter is directly linked to the longer lived parent. In the case of the strontium-90/yttrium-90 mixed nuclide source, the shorter lived yttrium-90 is in equilibrium with the longer lived strontium-90 parent, and the activity of both nuclides has a ratio of 1:1.

6.4 Cerenkov Radiator

The Cerenkov radiator itself consisted of a solid perspex cylinder 100mm in length, 44mm in diameter and was designed to fit inside the light-tight aluminium shielding which was bolted onto the flange of the PMT housing. At its centre was a 80mm hole 15mm in diameter which allowed a standard Amersham International $^{90}Sr/^{90}Y$ β-particle tubular source to sit inside. This presented the emitted β-particles with 20mm of perspex in which to be absorbed and produce Cerenkov light. The geometry of the Cerenkov radiator was designed such that the emitted cone of Cerenkov light produced by β-particles travelling along the central axis of the radiator would be incident on the photocathode without undergoing any internal reflection from the PMT shielding. This design assumed a low beam divergence of β-particles, however, beam divergence was taken into account during photon yield calculations.

No reflective coating or silvering was applied to the outer surface of the perspex radiator to encourage back reflection. To a first approximation internal reflections were assumed to be negligible and radiated photons propagating outside the

boundaries of the β-particle transmission core were lost completely and played no further part in photocathode illumination.

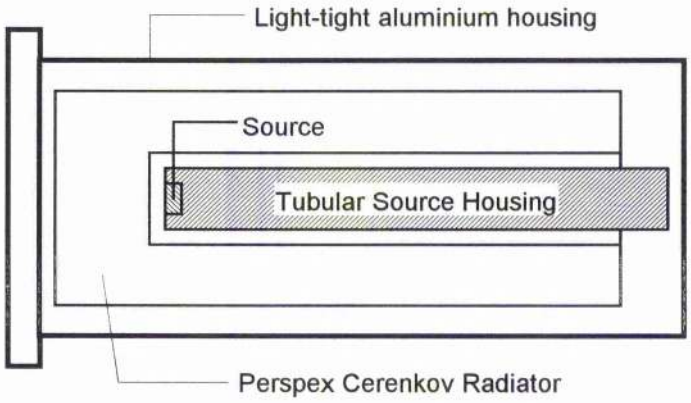

Figure 6.2. Details of the Cerenkov radiator medium and the positioning of the strontium-yttrium mixed nuclide tubular source.

6.5 Source Geometry

The standard Amersham International β-particle tubular source consists of a solid aluminium rod 84mm in length and 12mm in diameter. At one end of the source a 9mm diameter cavity is drilled along the source's central axis to a depth on 7mm. A 5mm diameter flat disk mixed nuclide strontium-90/yttrium-90 source was located at the base of this cavity. The activity of the $^{90}Sr/^{90}Y$ source, quoted as 74 kBq, was given in terms of 4π geometry and was therefore corrected for the restricted transmission angle that the geometry of the tubular source allows. From the geometry of the source, which can be seen in figure 6.3, the angle of emission of the β-particle beam, θ_β, is given by

$$\theta_\beta = tan^{-1}(x/y) \qquad (6.6)$$

where x is diameter of the source disk corrected for the geometry of the cavity and y is the depth of the source cavity.

Source disk diameter must be corrected to allow for the fact that the source disk is placed at the centre of the cavity floor, however it does not occupy the entire floor area of the cavity. For the purposes of geometric calculations of beam spread, it can be assumed that the source disk has an equivalent diameter of 7 mm.

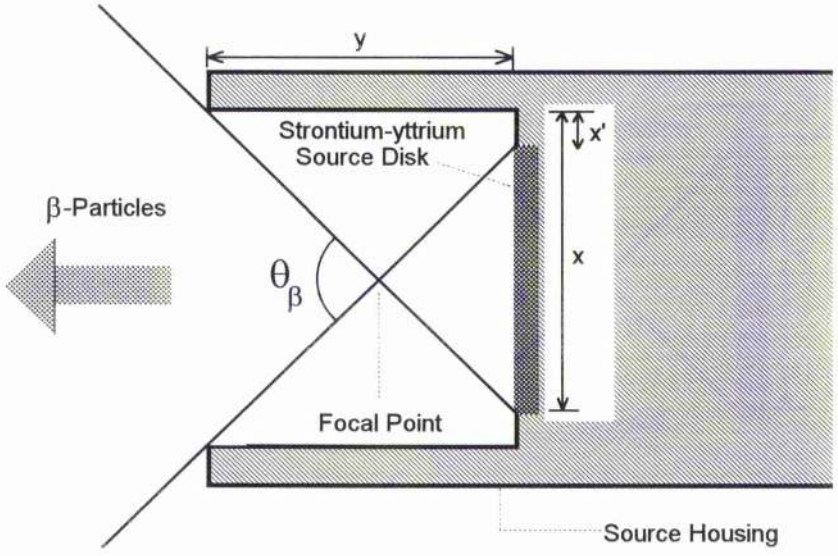

Figure 6.3. Details of the inner dimensions of the strontium-sttrium mixed nuclide tubular source and the extent of the β-particle emission cone.

The corrected source activity, A', within the restricted emission angle, θ_β, is therefore given by

$$A' = A/\pi \tan^{-1}(x/y) \qquad (6.7)$$

where A is the actual source activity quoted in 4π geometry. This geometric correction to activity in effect reduces the number of available β-particles likely to produce Cerenkov photons by a factor of 4 to 18.5kBq.

A further correction is needed to take into account the solid angle, θ_C, through which Cerenkov light is radiated. The solid angle, given in equation 6.2, describes the propagative angle of emitted Cerenkov photons relative to the track of the radiating charged particle. As $\beta \rightarrow 1$, equation 6.2 becomes

$$\theta_{C,max} = \cos^{-1}(1/n) \qquad (6.8)$$

The maximum solid angle through which Cerenkov light is radiated, $\theta_{C,max}$, is directly related to the refractive index of the radiating medium. With the β-particle beam the divergence angle defines the extent of Cerenkov propagation. The total angle of divergence from the normal, θ_{Total}, which represents the solid angle through which Cerenkov light is transmitted is therefore given by

$$\theta_{Total} = \theta_{\beta} + \theta_{C,max} \qquad (6.9)$$

The angle of divergence of the Cerenkov cone for the mixed nuclide strontium-90/yttrium-90 source in a perspex medium (n_D = 1.495) is approximately 93° from the normal.

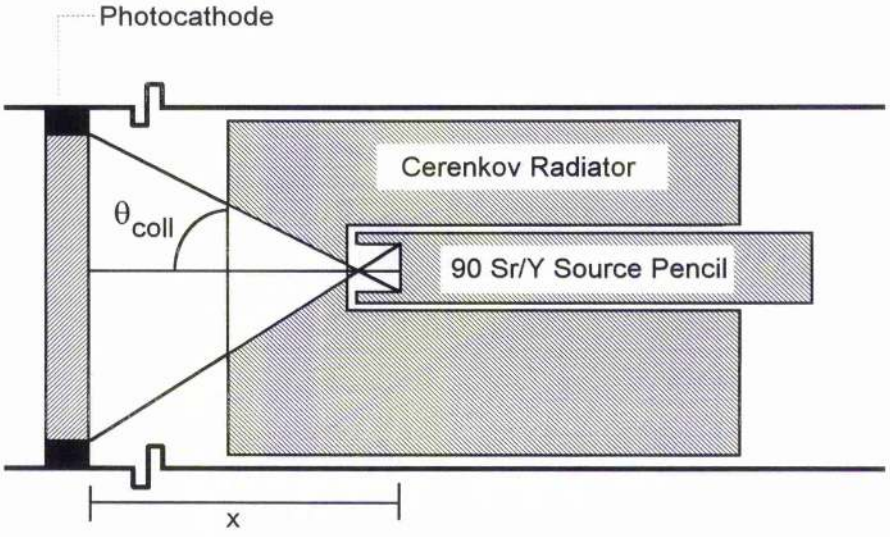

Figure 6.4. Details of the photocathode collection angle relative to the strontium-90/yttrium-90 source. Not to scale.

The Cerenkov radiator was mounted on the face of the photocathode. On the advice of EMI Electron Tubes, no optical coupling gels were used as this may have affected the optical response of the photocathode. Although the diameter of the photocathode was 52 mm, a plastic housing reduced its effective diameter to 44 mm, the same diameter as the Cerenkov radiator. The effective collection angle of the photocathode is given by

$$\tan \theta_{Coll} = r_e/x \qquad (6.10)$$

where r_e is the effective radius of the photocathode (22 mm) and x, described in figure 6.3, is the distance from the focal point of the source to the photocathode (24.5 mm). The photocathode photon collection angle is therefore 41.9°.

The ratio of the angle of collection to solid angle of Cerenkov emission, R, is given by

$$R = \theta_{Coll} / \theta_{C,max} + \theta_{\beta} \qquad (6.11)$$

These geometric considerations provide a method of assessing the overall probability and efficiency of Cerenkov photon yield collection. This factor further reduces the number of β-particles likely to produce Cerenkov photons to approximately 8338 β's per second, a total reduction in activity of some 89%. Only 11% of emitted β-particles contribute to Cerenkov production which leads to photoelectron production.

Table 6.2. Table of calculated data for $^{90}Sr/^{90}Y$ source.

Definition	**Symbol**	**Value**
4π Source Activity	A	74 kBq
Corrected Source Activity	A'	8338 Bq
Maximum Cerenkov emission angle	$\theta_{C,\,max}$	48.018°
Maximum β-particle Divergence	θ_{β}	45.000°
Total Cerenkov Cone	θ_{Total}	93.018°
Photocathode Collection Angle	θ_{Coll}	41.923°
Collection Ratio	R	0.451
Cerenkov Production Efficiency	ε	0.113

6.6 Defining the Cerenkov Spectral Region

The spectral region over which Cerenkov light may be observed and collected by the PMT, and thus lead to the production of photoelectrons, is precisely defined by two limiting factors: the spectral transmission function of perspex and the wavelength response of the photocathode.

From data on the transmission and absorption functions of perspex (Jelley, 1958), it was found that over the visible region of the electromagnetic spectrum, perspex has a low absorption coefficient, and this transparency continues into the near infrared up to around 2.4 μm. At shorter wavelengths below the visible spectrum, however, absorption increases rapidly and opacity becomes unity at approximately 295 nm.

Details of wavelength response, or quantum efficiency, of the photocathode (EMI Electron Tubes, 1995) revealed a relatively high efficiency over the entire visible spectrum, peaking in the ultraviolet at around 360 nm, then decreasing with wavelength up to 680 nm where the photocathode becomes insensitive to incoming photons. At wavelengths below the 360 nm peak, efficiency would normally decrease rapidly, however the fitted PMT quartz window extended this range down to 160 nm. From this data, it is estimated that the spectral range over which Cerenkov photons incident on the photocathode are detectable and lead to the production of photoelectrons is defined by the wavelengths 295 nm and 680 nm. The number of primary photoelectrons produced at the photocathode is determined by the product of the number of Cerenkov photons incident on the photocathode and the quantum efficiency of the photocathode.

Let $N_C(\lambda)$ be the number of Cerenkov photons of wavelength λ produced in the perspex radiator and $T(\lambda)$ be the transmission probability of a photon of wavelength λ travelling through the perspex medium. Therefore, the number of Cerenkov photons incident on the photocathode, $N'_C(\lambda)$, is given by

$$N'_C(\lambda) = N_C(\lambda).T(\lambda) \qquad (6.12)$$

$$N'_C(\lambda) = N_C(\lambda).T(\lambda) \qquad (6.12)$$

The number of primary photoelectrons produced at the photocathode, $N_e(\lambda)$, by incident photons of wavelength λ can therefore be defined as

$$N_e(\lambda) = N'_C(\lambda).\varphi(\lambda) \qquad (6.13)$$

where $\varphi(\lambda)$ is the quantum efficiency of the photocathode at wavelength λ. Substituting $N'_C(\lambda)$ in equation 6.12 gives the expression

$$N_e(\lambda) = N'_C(\lambda).T(\lambda).\varphi(\lambda) \qquad (6.14)$$

It can be seen that the relationship between the number of primary Cerenkov photons generated and final number of photoelectrons produced is dependent on the two independent functions, namely the transmission probability of the Cerenkov radiator and the quantum efficiency of the photocathode.

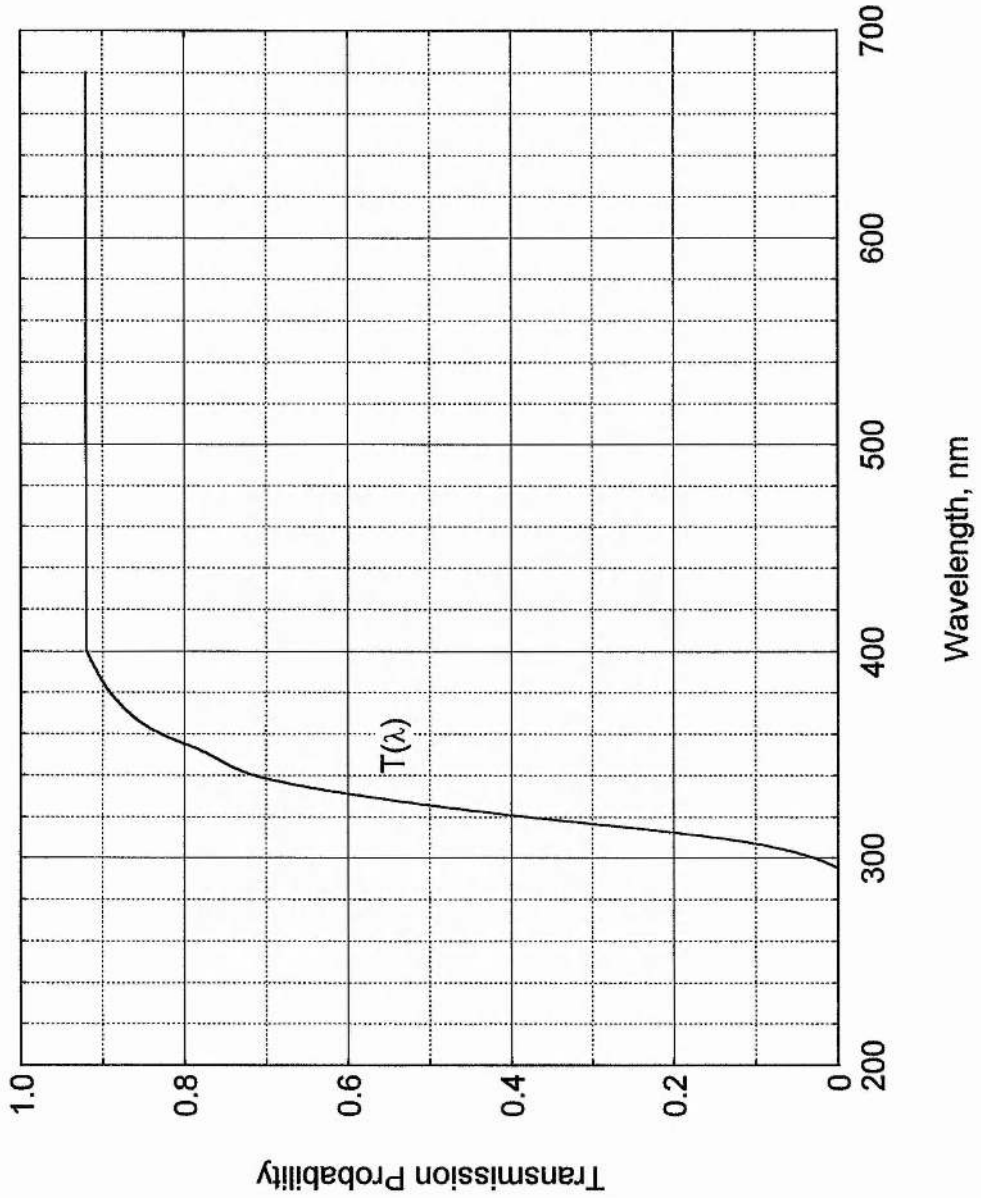

Figure 6.5. The transmission function of perspex, T(λ), (Jelly, 1958)

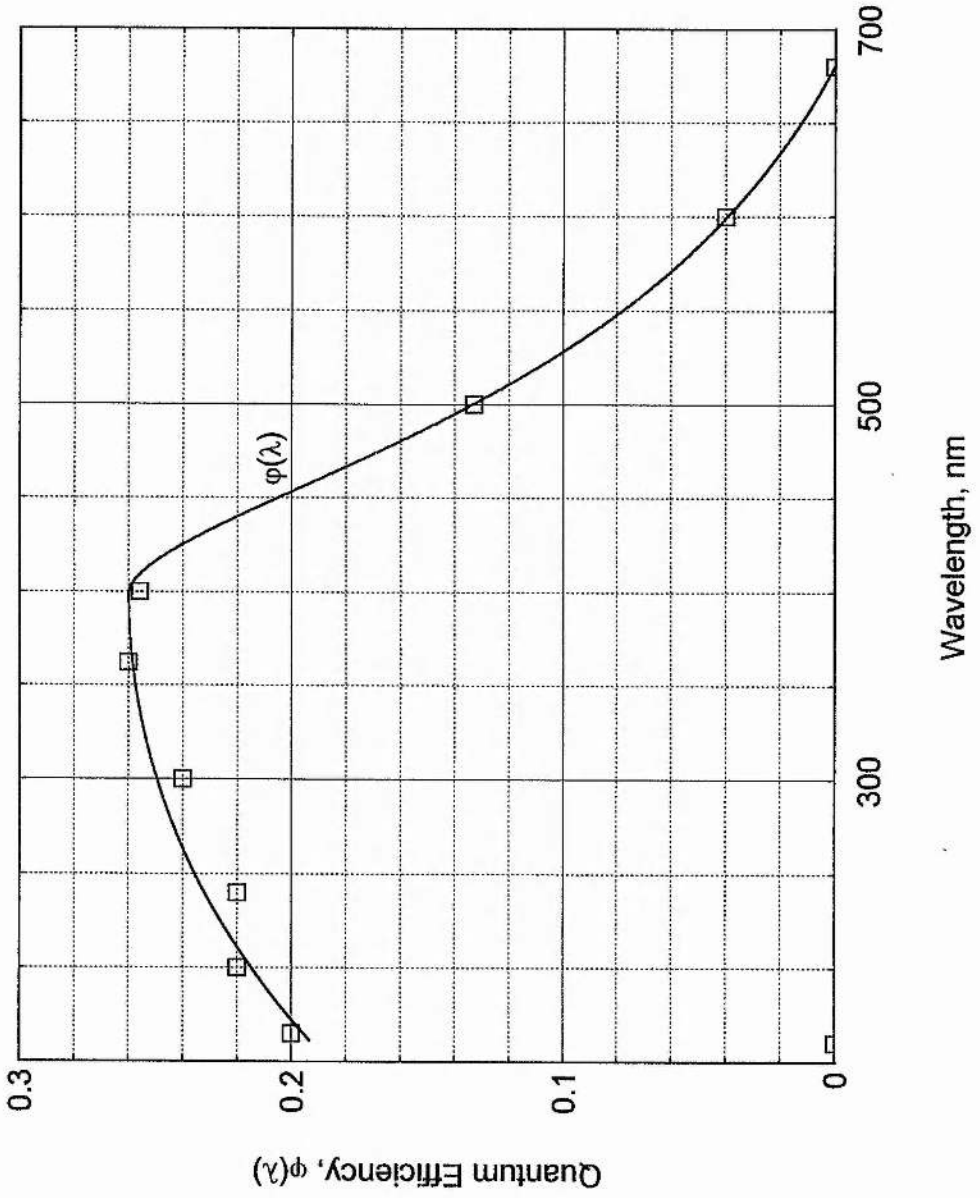

Figure 6.6. The quantum efficiency of the EMI 9235QB photomultiplier tube, $\varphi(\lambda)$.

The quantum efficiency, $\varphi(\lambda)$, can be expressed empirically with two functions; equation 6.15a which predicts efficiency over the spectral region 150 nm to 400 nm, and equation 6.15b which predicts efficiency between 400 nm to 680 nm.

$$\varphi(\lambda) = 0.26\,(\lambda/400)^{a}\,.\,(2.0 - (\lambda/400)^{a}) \qquad (6.15a)$$

$$\varphi(\lambda) = 0.26\,(\lambda/400)^{a}\,.\,(1.0 - a.ln(\lambda/400)) - b.ln(\lambda/400) \qquad (6.15b)$$

where λ is the wavelength expressed in nm and the proportionality constants a = 0.7765 in equation 6.15a, and a = -6.552 and b = 0.0673 in equation 6.15b.

The product of transmittance probability and quantum efficiency at wavelength λ, is the photoelectron production probability, $\Phi_{PE}(\lambda)$, and can therefore be defined as

$$\Phi_{PE}(\lambda) = T(\lambda).\varphi(\lambda) \qquad (6.16)$$

and therefore

$$\Phi_{PE} = \frac{1}{\Delta\lambda}\sum_{n=\lambda_{min}}^{\lambda_{max}}\left[T(\lambda_n).\varphi(\lambda_n)\right] \qquad (6.17)$$

This function, expressing both photon absorption losses and photon detection probability, defines the final wavelength boundaries within which the Cerenkov spectrum will be observable, and predicts the relative intensities of individual

Cerenkov spectrum within the defined spectral region, it provides the mean photoelectron production probability, Φ_{PE}, which numerically has a value of 0.141.

6.7 Generating the Cerenkov Spectrum

To a first approximation, the characteristics of a Cerenkov spectrum are adequately described by the general Cerenkov equation (Jelley, 1958), Eqn (6.6), however this equation assumed that a charged particle travelling a path length, r, will travel at constant speed in the medium, such that β^2 remains constant. In reality, however, ionisation and other radiative energy losses within the medium ensure that the charged particle velocity decreases with penetration depth. To take account of the continuous decrease in β^2, it is necessary to redefine the $(1\text{-}1/\beta^2 n^2)$ function with respect to the path length or range travelled. For ease of reference, this redefined function has been called the *Cerenkov Integral.*

6.8 The Cerenkov Integral

The Cerenkov Integral provides a Cerenkov photon yield function corrected for the continuous slowing down of the charged particle within the transit medium. Mathematically, the Cerenkov Integral can be expressed as

$$\int R_C . dx = \int_0^{R_C} \left(1 - \frac{1}{\beta_x^2 . n^2}\right) . dx \qquad (6.18)$$

where R_C is the Cerenkov range of the charged particle, and is defined as

$$R_C = R_{csda} - R_{threshold} \qquad (6.19)$$

The Cerenkov threshold range, $R_{threshold}$, is defined as the continuous slowing down approximation (csda) range of a charged particle with kinetic energy equal to the Cerenkov energy threshold, given in equation 6.3. The Cerenkov range, the path length along which Cerenkov photons will be radiated, can be defined as the range of a charged particle above the Cerenkov threshold range.

Continuous slowing down approximation range data was obtained from ICRU Report 37 and was plotted against respective particle velocity, β^2. By generating a spline data set for this graph, an accurate relationship between β^2 and R_{csda} was obtained. The R_{csda} corresponding to the Cerenkov energy threshold was then calculated and found to be 3.77 g/cm^2 in perspex. By then plotting R_C (R_{csda} - 3.77 g/cm^2) against $(1\text{-}1/\beta^2 n^2)$ and performing a numerical integration, numerical solutions to the Cerenkov Integral were produced.

To calculate photon yield, it is first necessary to establish the path length over which the particle will generate Cerenkov photons. Photons are only emitted when the particle possesses kinetic energy greater than the Cerenkov energy threshold, E_C. Below this energy, equation 6.2 is no longer satisfied and Cerenkov emissions cease.

6.9 The Cerenkov Photon Yield

Taking into account the redefinition of the Cerenkov Integral, the photon yield function for a single charged particle can now be expressed as

$$N_T = 2\pi\alpha . \int_0^{R_C} \left(1 - \frac{1}{\beta_x^2 . n^2}\right) . \int_{\lambda_{min}}^{\lambda_{max}} -\frac{1}{\lambda^2} . d\lambda . dx \qquad (6.20)$$

where α is the fine structure constant ($\mu e^2 c/2h$).

For a β-particle source of activity A Bq^{-1} emitting a spectral distribution defined by the probability, P_i, that a β-particle will be emitted with kinetic energy, T_i, the total yield of Cerenkov photons is given by

$$N_{T,sp} = 2\pi\alpha . A . \sum_{\beta_{min}}^{\beta_{max}} \left[P(\beta_i^2) . \Delta(\beta_i^2) . \int_0^{R_C} \left(1 - \frac{1}{\beta_x^2 . n^2}\right) . \int_{\lambda_{min}}^{\lambda_{max}} -\frac{1}{\lambda^2} . d\lambda . dx \right] \qquad (6.21)$$

where A is the source activity, $P(\beta^2_i)$ is the source spectral distribution, $\Delta(\beta^2_i)$ is the channel width, β^2_x is the velocity of the β-particle and n is the refractive index of the Cerenkov medium.

To obtain the number of photoelectrons produced at the photocathode, equation 6.21 must be multiplied by the mean photoelectron production probability, Φ_{PE}, given in equation 6.17, which takes in account the wavelength dependent transmittance of perspex and the quantum efficiency of the photocathode.

6.10 Calibration Using Integrated Energy

The original approach to PMT calibration was to collect several event spectra produced by the Cerenkov source using a Multi-Channel Analyser (MCA), operating the PMT at various voltages over its optimum operating range. The collected spectra were then converted into voltage spectra using the relationship between MCA channel number and input signal voltage. The resultant voltage spectra were then numerically integrated to obtain the integrated energy over the duration of each experiment.

This method took into account all other signal gains from the preamplifier and main amplifier, which were both calibrated using a research pulser, EG&G ORTEC 448. From the collected amplified voltage, V_{output}, the overall gain of the photomultiplier, G_{PMT}, can be calculated as

$$G_{PMT} = \frac{C_{PMT}.V_{output}}{N_e.e.G_{preamp}.G_{main}} \qquad (6.22)$$

where C_{PMT} is the capacitance of the photomultiplier tube (50×10^{-12}F),

V_{output} is the total final detected output voltage,

N_e is the number of electrons produced at the photocathode,

G_{preamp} is the gain of the preamplifier, and

G_{main} is the gain of the main amp. e is the charge of the electron.

From the derived equation 6.22, it was assumed that the integral of collected voltage would be directly proportional to PMT gain. In practice this was not the

case, and the correlation between the collected spectra and sensible gain values were not forthcoming. It was assumed that there does exist a relationship between collected voltage and PMT gain, however much more work and analysis would be required to derive a suitable method for extracting appropriate data from voltage spectra and subsequently this method was eventually abandoned.

The three gain curves in Figure 6.7 were obtained at operating voltages of -1100, -1150 and -1200 volts respectively, each over a period of 1800 seconds. The curves were then integrated to obtain the data given in Table 6.3. No correlation between this data and that collected by the method described in Section 6.11 was found.

Table 6.3. Integral Areas of Figure 6.7 gain curves.

Voltage	Integral Area (Volts)
-1100	25275.6
-1150	20856.5
-1200	15629.1

6.11 Calibration Using Anode Current

The alternative method of calibration was to measure the PMT anode current with an electrometer connected directly to the PMT anode while the photocathode was under Cerenkov illumination. This approach measured directly the results of current amplification and removed the need for any amplification electronics or indeed an MCA.

In principle, photoelectrons liberated at the photocathode are accelerated onto a chain of dynodes. The kinetic energy transferred during the collision between the accelerated photoelectron and the dynode liberates further secondary electrons,

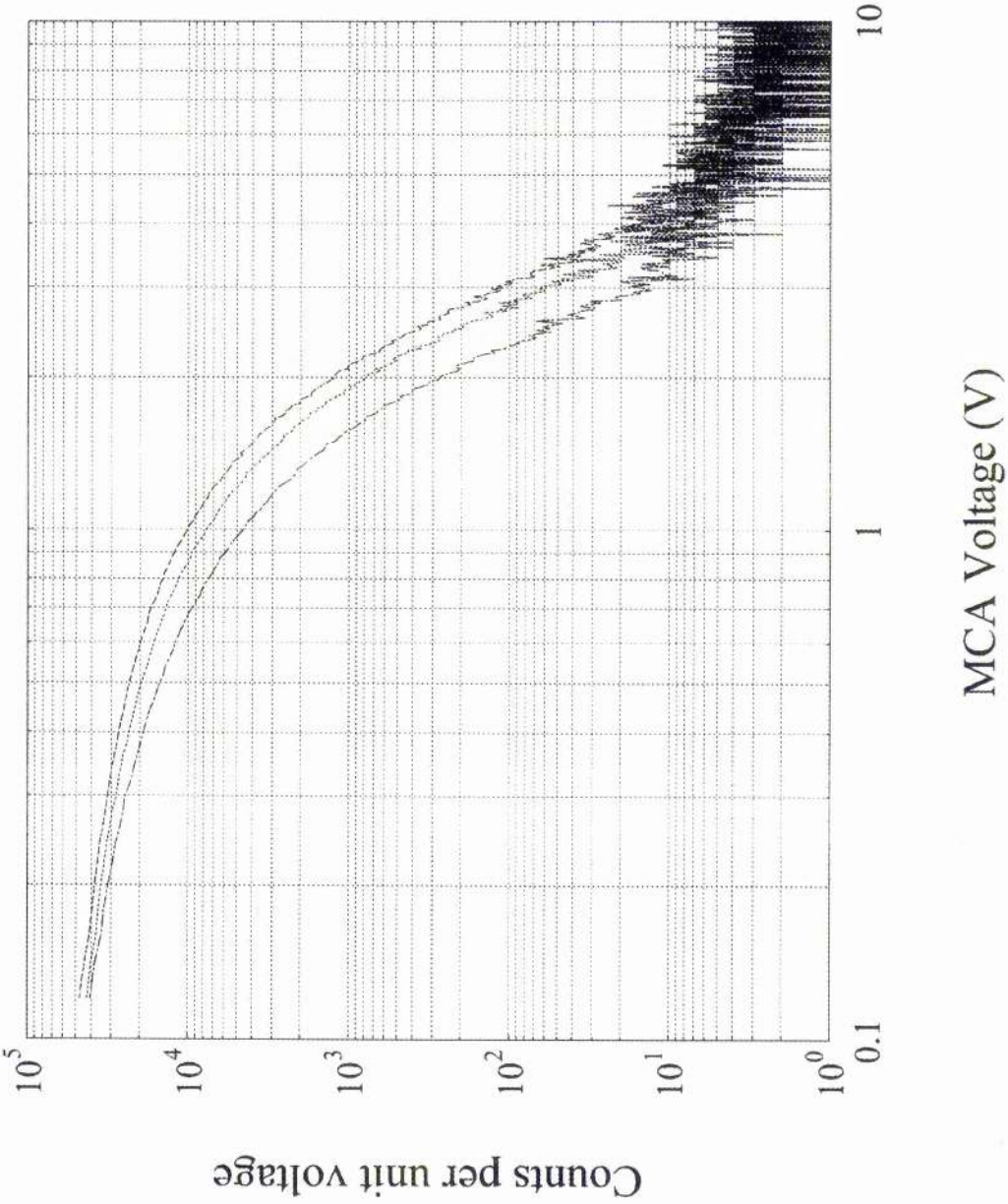

Figure 6.7 Gain curves obtained with the EMI 9235QB PMT operating at -1100, -1150 and -1200V respectively.

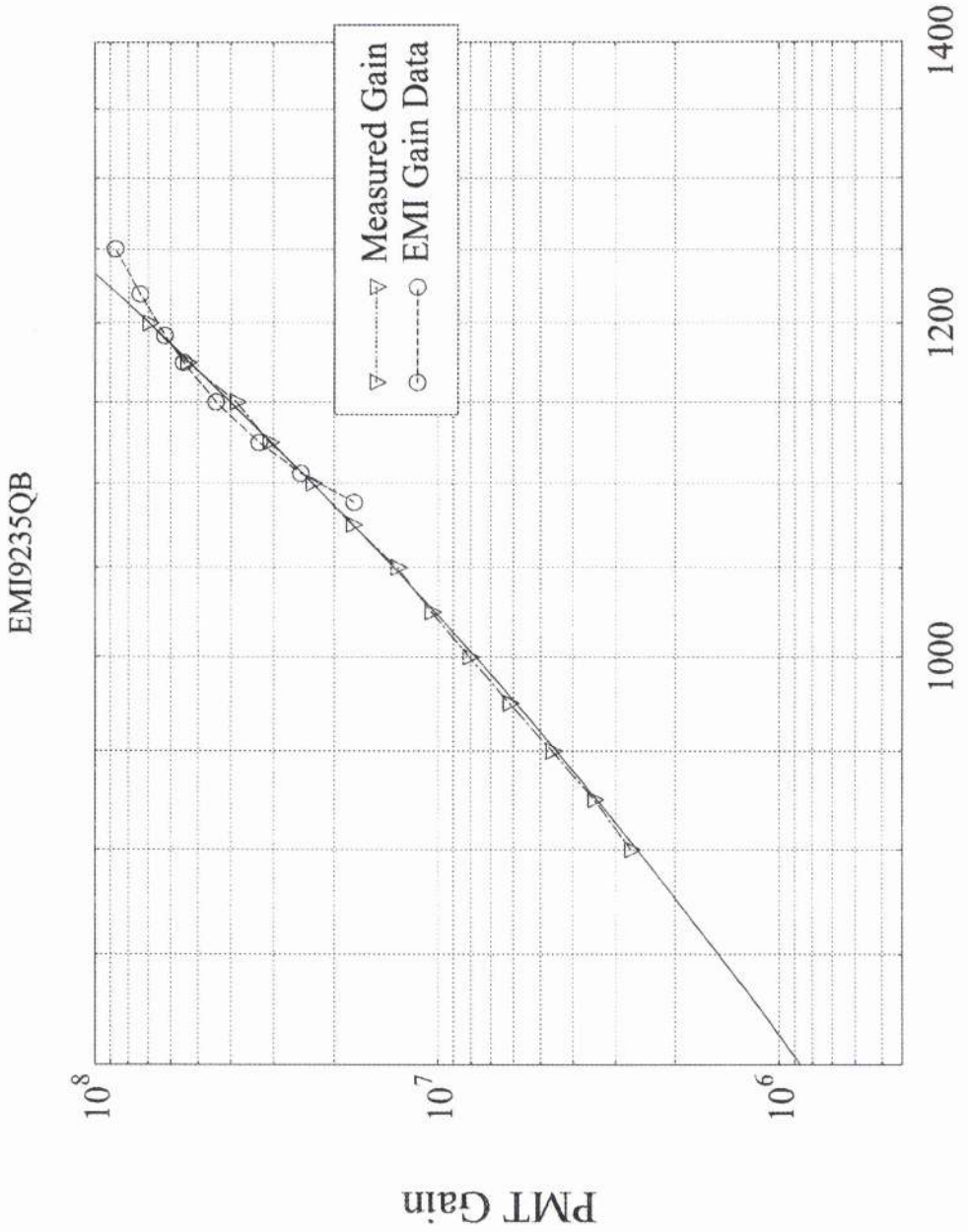

Figure 6.8 EMI PMT gain curves.

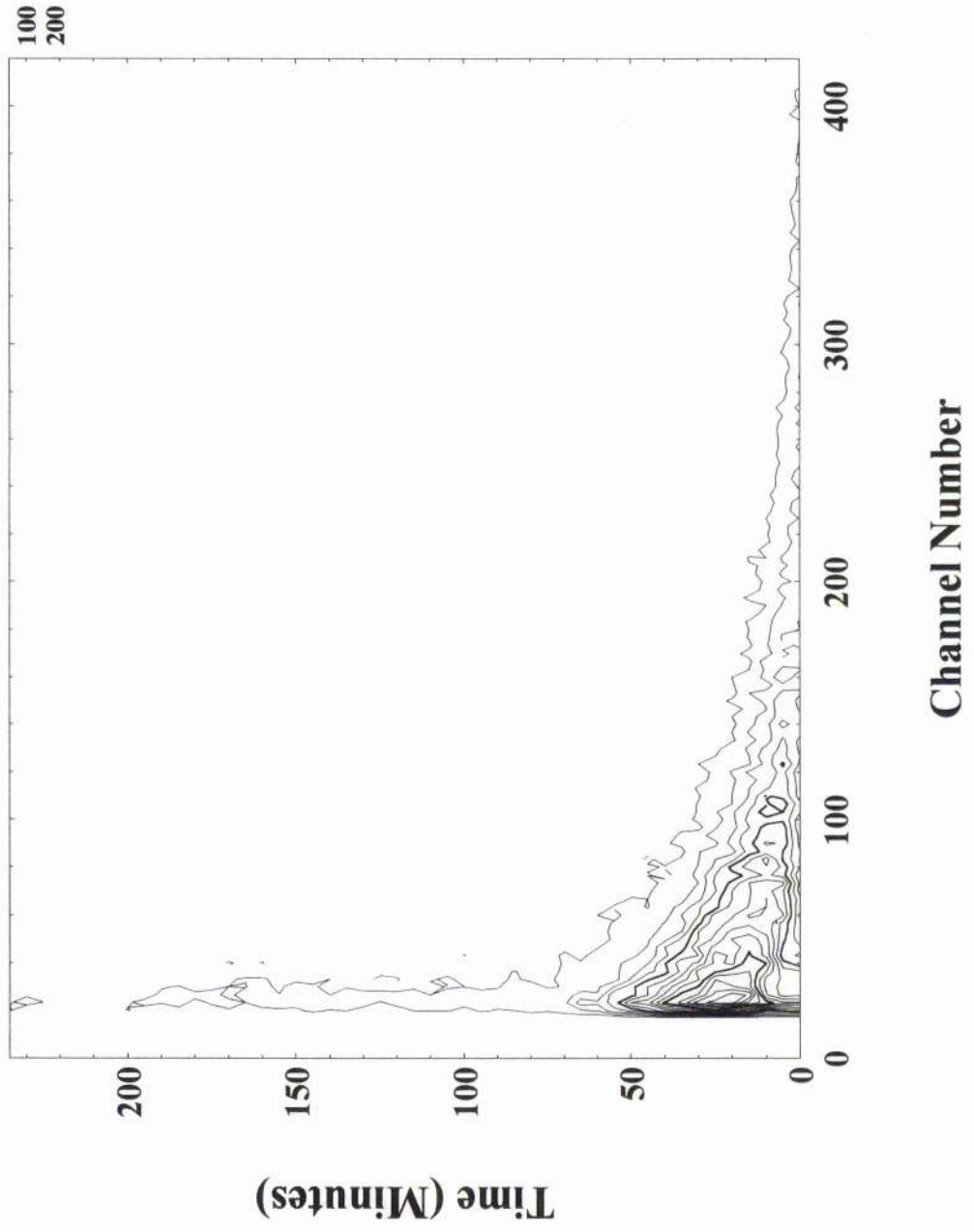

Figure 6.9 Contour map of observed reduction in dark current during EMI photomultiplier warm up period.

which in turn are accelerated and collide with the next dynode in the chain. This process of charge multiplication continues down to the end of the dynode chain where the amplified charge is fed to the anode output terminal. Once the theoretical photocathode current is calculated, PMT gain, G, is then simply the ratio of anode current to photocathode current, given as

$$G = I_A/I_{PC} \qquad (6.23)$$

where I_A is the collected anode current and I_{PC} is the theoretical photocathode current.

The photocathode current, I_{PC}, is directly proportional to the number of photons incident on the photocathode, N_C, and the quantum efficiency of photocathode, φ. Since both photon yield and quantum efficiency are strongly wavelength dependent, it is necessary to describe this relationship in terms of this wavelength dependency, so that

$$I_{PC} = \int e.A.N_{C,\beta}(\lambda).\ \varphi(\lambda).d\lambda \qquad (6.24)$$

where e is the charge of the electron, $N_{C,\beta}(\lambda)$ is the fluence of photons of wavelength λ incident on the photocathode and $\varphi(\lambda)$ is the quantum efficiency of the photocathode at wavelength λ. Integrating equation 6.24 over the spectral region gives the theoretical photocathode current for an incident photon intensity, $N_{C,\beta}$.

Therefore

$$I_{PC} = e.A.N_{C,\beta}\Phi_{PE} \qquad (6.25)$$

When calculated, the value for I_{PC} was typically 2.56 x 10^{-15} A. By operating the PMT over a wide range of operating voltages and collecting the anode current, good data were collected and are presented in the table below:

Table 6.4 Variation in PMT anode currents with operating voltage.

Operating Voltage (V)	Anode Current (A) Signal+BG	Background (A)	Signal (A)
900	7.0E-09	8.97E-11	6.91E-09
925	9.0E-09	1.19E-10	8.88E-09
950	1.2E-08	1.56E-10	1.18E-08
975	1.6E-08	2.05E-10	1.58E-08
1000	2.1E-08	2.70E-10	2.07E-08
1025	2.7E-08	3.44E-10	2.67E-08
1050	3.4E-08	4.34E-10	3.36E-08
1075	4.6E-08	5.37E-10	4.55E-08
1100	6.0E-08	6.78E-10	5.93E-08
1125	8.0E-08	8.97E-10	7.91E-08
1150	1.0E-07	1.19E-09	9.88E-08
1175	1.4E-07	1.59E-09	1.38E-07
1200	1.8E-07	2.11E-09	1.78E-07

By measuring the anode current, the gain calculation reduces to the simple ratio of anode to photocathode current once the theoretical photocathode current is calculated. This gain value can then be related to the post-detection amplification making the calibration much simpler.

Fitting an empirical best-fit curve to the data in table 6.4, gives

$$G_{PMT} = [a.exp(b.V/c)]/d \qquad (6.26)$$

where V is the operating voltage of the PMT, and a, b, c and d are constants of proportionality with values of 1.34 x 10^8, 2.78, 253 and 1.01 x 10^6 respectively.

This method proved to be by far the more successful, providing good data to allow PMT calibration. Comparison of the measured gain curve with that of the supplied EMI data, shown in figure 6.8, suggests that this method is a suitable procedure for determining the gain calibration of a photomultiplier tube. An additional advantage to this method of calibration was the low level of electronic noise detected during these experiment.

6.12 Electronic Noise

Initial experimental runs to detect and collect Cerenkov spectra were severely hampered by the presence of significant background noise, which often appeared to be several orders of magnitude greater than the Cerenkov spectrum being collected. These effects, for the most part, appeared to be time dependent and would decrease over a period of four to six hours. This supports Jelly's (1958) finding that PMTs should be left for a lengthy period to stabilise prior to any Cerenkov experiment.

The expected increased noise due to dark current excitation of the photocathode by the brief exposure to daylight during the installation and removal of the β-particle source was observable, but did not account for the noise. Dark current, which can double with every 5°C increase in ambient room temperature (EMI Electron Tubes, 1995), can be reduced by introducing refrigeration around the photomultiplier tube, however, this was not necessary.

The effects of both ambient room temperature and the increased temperature within the PMT itself due to self-heating were all be taken into account and were responsible for marked increases in background noise while working at low light levels. It has been found in repeated experiments that electronic noise within the first

hour precludes any useful measurements from being taken. It appears to be inversely related to the temperature of the apparatus. Investigations into the time and temperature dependency of this background noise indicate that the PMT requires a period of at least two hours in which to *warm up* and reach thermal equilibrium before any measurements may be carried out. Figure 6.9 shows the decrease in integral background counts over time and confirms the necessity for a three hour warm up period.

In practice, however, significant problems were encountered in recording a suitable Cerenkov spectrum. Due to the low intensity of Cerenkov light, it was expected that good spectra would be difficult to obtain, however, early experiments indicated that background noise was obscuring any collected signals. Lengthy investigations revealed that equipment temperature was the primary cause.

Initial effects of heating on the PMT cause a build-up of background noise which decays exponentially over a period of two to three hours. While this effect is repeatable, it generally precludes any experimental runs from being made during this time. Natural environmental background and cosmic ray events were ruled out as being a significant source of noise. By allowing the PMT to settle down over several hours (Jelley, 1958), noise no longer became a significant problem.

6.12.1 Reducing Electronic Noise

The systematic testing of each piece of equipment and connecting leads revealed a prominent 60msec pulse superimposed on the background noise, a timing that corresponded to a signal of 16.66 kHz. Investigations into the source of this noise revealed that the MCA VDU time-line oscillator was radiating a 16.66 kHz RF signal

from the chassis and more predominantly from the MCA input lead and power cable. The radiated signal was being detected by the preamplifier-to-main amplifier lead and to a lesser extent by both the high voltage supply cable to the PMT and by the signal output cable from the PMT to the preamplifier.

As the MCA was originally powered from the same extension as the rest of the equipment, the RF signal appears to have been propagated to the other equipment before going to earth. Initially, distancing the MCA from the PMT equipment did offer a marginal reduction in detected RF noise, however powering the MCA from a separate socket removed the signal completely, though the general broadband noise signal was still present. As a last resort, the MCA interface board was removed from the ADCAM MCA and installed in a desktop PC. This reduced all noise levels to acceptable values and it was assumed that the portable ADCAM MCA unit was the main source of the problem. Ortec ([Ortec, 1997] Private Communication) have not reported similar noise problems with this equipment.

Chapter VII

Conclusion and Further Research

7.1 Conclusion

The legal responsibility of the monitoring of radiation hazards in the workplace and the environment, and the effectiveness of radiotherapy in the clinical environment is based upon our basic understanding of biophysical interactions as they were described some 50 years ago. Current assessment of the bio-effectiveness of a radiation field is made in crude terms of absorbed dose, which by its very nature, is strongly dependent on radiation quality and therefore radiation type.

This project, at both practical and theoretical levels, has succeeded in proving that a detector with a response function capable of giving an absolute measure of the bio-effectiveness, independently of the radiation type, is achievable in the future. However, many practical and theoretical problems must be overcome before any further advances in this field of research can be made.

This study set out with the intention of investigating the feasibility of such a bio-effectiveness detector and whether it's response function would allow the detection of radiation quality. The experimental evidence presented confirms that the detector can

indeed respond to radiation quality and that sources of different photon energies can provide unique response spectra. The absolute bio-effectiveness approach to dosimetry through the use of scintillation nanodetectors is novel, and with such emerging technology, fundamental problems do exist.

Theoretically, the most fundamental problem was the extraction of the critical 'paired-events' from collected spectra. It is the yield of these events that provides a measure of absolute bio-effectiveness. Currently, there is no successful method of extracting biologically relevant data from collected spectra.

Experimentally, major difficulties were encountered in ensuring consistency of signal measurement. Inherent detector noise and the constant need to place and replace scintillators, build-up layers and reflectors for background collection produced high levels of ambient electronic noise which were generally indistinguishable from 'wanted' events.

7.2 Recommendations for Future Work

Significant developments are required to produce a more effective prototype detector, with special care being taken on the provision of adequate shielding from external light sources. This would allow sources to be placed and removed without the need to power-down the HPD, and would result in more stable operation and detection. An electronic liquid crystal optical shutter mechanism placed between scintillator and light-pipe would be a distinct advantage, allowing scintillation-free backgrounds to be

obtained without the need of removing the scintillator or switching off and on the detector.

The theoretical model, which provides the critical conceptual link between the experimental observed spectra and the associated biological damage in mammalian tissue requires further development and expansion to allow extraction of 'paired-events.'

The Monte Carlo modelling of photon transport in light-pipes, which was originally adopted to provide a more accurate measure of photon losses in the system, has provided good data. Preliminary results obtained from the model suggest that this may indeed by a more viable method of accurately estimating photon losses. However, a more developed model, encompassing a rigorous treatment of wavelength dependent absorption, surface scattering and reflection mechanism is required. Such a model would not only benefit this project, but would undoubtedly enhance other analytical methods which make use of light-pipes and other light-guides.

The potential of this project far outweighs any of the problems encountered. Experimentally, most problems would be overcome with a re-design of the detector such that all stray ambient light is prevented from reaching the photocathode, while theoretically, a technique must be developed to allow extraction of the yields of 'paired-events.'

Appendix A

Nanoscintometry Spectrum Analysis Software

A.1 Introduction

The experimental use and qualitative analysis of nanoscintometric spectra for the determination of radiation induced biological damage cross-sections has created a novel requirement for dedicated software that can automatically search for and identify significant spectral structures. Previously such spectral analysis operations have been performed by computer-based γ-ray spectroscopy systems and have proved to function to a high degree of reliability and accuracy.

The characteristic profile of a spectrum obtained by the DEP hybrid photodiode in the nanoscintometry mode differs both in shape and structure from the conventional γ-ray spectrum and currently available analysis packages do not meet the current requirements of this project. It became essential that an analytical code, unique to nanoscintometry, was developed process the data. The most suitable algorithm for this analysis was the second difference approach suggested by Mariscotti (1967) and which is now widely used throughout the spectroscopy field.

A.2 Data Extraction

Spectral data obtained by the 2048-channel Ortec 100T MCA was saved from the MCA buffer to disk, and was made possible by a decoding algorithm which converted it into a conventional digital form. Once in this form, the data could easily be manipulated and analysed.

A.3 Statistical Smooth

When irradiated with high fluence sources, the DEP hybrid photodiode was capable of readily discriminating up to eight photo-electron peaks with little or no difficulty. Higher k peaks ($k > 8$) were present in the data but statistical fluctuations made their appearance and nature difficult to determine. In the case of sources with a weaker photon fluence, of the order of a few 100 kBq, peaks $k = 1$ to $k = 5$ were still visible, but higher order peaks became difficult to determine. This otherwise unusable data could nevertheless be extracted with the implementation of a smoothing algorithm (averaging neighbouring points) which was applied to the entire array of raw data to reduce the effect of statistical fluctuation. The smoothing method adopted was a sliding window smoothing algorithm of the form:

$$x_i = \frac{1}{(2j+1)} \sum_{k=i-j}^{j} x_k \qquad \text{(A.1)}$$

where the summation is averaged over $2j + 1$ data channels.

This approach allowed a certain flexibility in the selection of width of the window, however, special care was taken to avoid a large window width that might lead to an appreciable distortion of the basic data structure. Various trials were carried out to obtain the most efficient window width. A two step approach finally proved to be the most useful. In the first smoothing algorithm, a window width of j = 33 was selected. This width provided good data smoothing without perceivable distortion to the data set and readily revealed up to k = 12 peaks. A second much narrower smoothing algorithm (j = 11) was then applied to remove minor spectral features from individual peaks. When these minor features were not removed, the subsequent peak search routine would falsely identify them as individual peak structures.

For the specific voltage, diode bias and final electronic amplification used, these values provided optimal data reduction, however, variations in the operating characteristics would require other values to be used. Window width, in general, is proportional to overall system gain. The first smoothing window width is approximately 1/3 of the total peak width at full width, with the second smoothing window width being set to 1/3 of the first window width.

A.4 Peak Identification

Automated peak identification is now a well developed branch of radiation spectroscopy, and many commercially designed software packages are now available. Most are based on the original work by Mariscotti (1967) and Koskelo *et al.* (1980). Current packages incorporate routines developed by Mariscotti and Koskelo *et al* in the form of the GAUSS and SAMPO families of γ-ray spectroscopy applications.

These particular spectroscopy packages focus on data acquisition from solid state Ge(Li) detectors which are characterised by high energy spectral resolution. Both GAUSS and SAMPO codes use the second difference of raw spectral data to identify points at which the data rapidly alter in gradient, a characteristic feature of a sharp photopeak rising above the background continuum. In the vicinity of a peak structure, the second difference function becomes negative making peak position easily identifiable. The original algorithm proposed by Mariscotti is given by:

$$S_i = N_{i-1} - 2N_i + N_{i+1} \qquad \text{(A.2)}$$

Applying the algorithm in this form to nanoscintometry spectra revealed very few features as the function was only effective over three channel widths. A typical nanoscintometry peak width is of the order of 100 channels, and therefore such a narrow region of interest only revealed minor discontinuities on individual peaks. By broadening the function, however, equation A2 becomes a powerful peak identification tool. A value of approximately half the full width of a peak proved to be the most efficient, and following smoothing, up to 12 peaks could be readily identified. Once identified and the background continuum subtracted, the peak centroid and peak area were calculated. From this data, Gaussian distributions can be fitted to each peak in turn.

As a check of the peak centroid, a second routine (PeakScan) was implemented to identify the peak position using only the original raw spectral data. By inverting the spectrum and applying the same algorithm, the positions of inter-peak valleys could also be identified. Since valleys have a slightly narrower structure than the

associated photo-electron peaks, the function was narrowed to operate over an effective width of 40% of the full width of the peak.

A5. Continuum

In the majority of experiments involving the collection of a radiation spectrum, the desired signal is usually superimposed on a background continuum. Before any analysis of the spectrum can be made, the background must be subtracted, reducing the spectrum to data generated only by the radiation source of interest. Background data are usually then discarded.

Although a conventional continuum is not present in nanoscintometry experiments, the background pseudo-continuum contribution was found to be of importance as it contained valuable information about other radiations associated with primary γ-ray sources. In the case of a pure γ-ray emitter, the continuum followed a distinctive exponential decrease. In the presence of α- and β-particles, the continuum appeared as a Gaussian distribution. Analysis of the associated spectral continuum therefore proved to be a useful tool in the detection of α- and β-particle irradiation.

A6. NanoSpec98 Program Listing

The final version of NanoSpec98 incorporates many of the features that where developed during various experimental runs. The need to include additional calculation subroutines was easily accommodated, and the program continued to have minor refinements added as the need arose. The original program was written in

QBASIC as it was the most accessible programming platform, however, a Windows compatible version was also compiled in VB5, and a FORTRAN version was developed.

This version of the program produces five output data files:

1. **isotope.dat:** contains two sets of data points: a set which describes the original spectrum, and a set which describes the smoothed spectrum after the continuum has been subtracted.
2. **continuu.dat:** contains a set of data points which define the continuum spectrum.
3. **gaussian.dat:** contains the Gaussian fit data of each individual photopeak.
4. **maxima.dat:** contains data points which define the photopeak envelope.
5. **gaussian.tbl:** contains a table of data for the reconstruction of the Gaussian fits: Centroid, peak height, peak width, peak area and continuum.

```
'*****************************************************************
'*****************************************************************
'
' 'Spectrum.bas' This program analyses nanospectrometry spectra and
' extracts physical data.
'
'

    DIM MCAChannel(2048), MCAChannel0(2048), MCAChannelA(2048) AS
    DOUBLE
    DIM Peak(2048), PeakA(2048), Valley(2048), ValleyA(2048) AS DOUBLE
    DIM MCAArray(2048), MCAArray1(2048), MCAData(2048) AS DOUBLE
    DIM MCAData1(2048), PeakArea(100), Continuum0(100) AS DOUBLE
    DIM PeakMax(100), PeakProb(100), PeakMaxima(100) AS DOUBLE
    DIM a AS STRING * 1

' *** Define Experimental conditions and constants
    MaxChan = 2048
    Offset = 86
    pi = 3.1415927#
    CW = 55                          ' Channel Width
```

```
    PeakInterval = 45
    ValleyInterval = 55
    Activity = 1760000!              ' Source Activity in 4pi
    dOmega = pi / (2 * pi)           ' Solid Angle
    Branch = .162                    ' Gamma Branching Ratio

' *** Define and open source data file
    filename$ = "C:\phd\thesis.phd\data\*.chn"
    filename$ = "A:\am241b1.chn"
    OPEN filename$ FOR BINARY AS #1

' *** Extract Data in Ortec Data Format from Channels
    SEEK #1, 33
    FOR i = 1 TO MaxChan
    m = 0
    FOR n = 0 TO 3
     GET #1, , a
     Bit = ASC(a)
     m = m + (256 ^ n) * Bit
    NEXT n
    MCAChannel(i) = m
    MCAChannel0(i) = m
    IF m > MaxDataValue THEN MaxDataValue = m
    NEXT i

' *** Extract Live Time from File
    SEEK #1, 12
    Live = 0
    FOR i = 12 TO 15
     GET #1, , a
     Bit = ASC(a)
     Live = Live + (Bit * (256 ^ (i - 12)))
    NEXT i
    livetime = INT(10 * Live * .02 / 256) / 10
    CLOSE
    PRINT "Live Time ="; livetime

'
**********************************************************************

  ' *** 33-Point Smoothing Routine
  '    -------------------------
  ' This routine seems essential when using a high number of MCA channels.
  ' The 11-point kernel seems to be the best (3, 5 and 7 are inadaquate to
  ' smooth the statistical fluctuations which are present in Nanoscint.
  ' spectra.

     kernel = 33
     interval = (kernel - 1) / 2
```

```
    FOR i = Offset TO MaxChan
     sum = 0
     kernel2 = kernel

     min = i - interval
      IF min < 0 THEN min = 0
     max = i + interval
      IF max > MaxChan THEN
        diff = max - MaxChan
        max = MaxChan
        kernel2 = kernel - diff
      END IF

     FOR n = min TO max
      sum = sum + MCAChannel(n)
     NEXT n

     IF sum > 0 THEN sum = sum / kernel2

     MCAData(i) = sum

    NEXT i

' *** Swap back data into MCAChannel Array

    FOR i = 1 TO MaxChan
     MCAChannel(i) = MCAData(i)
    NEXT i

' *** 11-Point Smoothing Routine
'    -------------------------
' Second smaller smoothing Kernel to remove small peak discontinuities.
' An 11-point smooth has little overall effect on the data but still
' enables minor 'unwanted' features to be removed.

    kernel = 11
    interval = (kernel - 1) / 2
    FOR i = Offset TO MaxChan
     sum = 0
     kernel2 = kernel

     min = i - interval
      IF min < 0 THEN min = 0
     max = i + interval
      IF max > MaxChan THEN
        diff = max - MaxChan
        max = MaxChan
        kernel2 = kernel - diff
      END IF
```

```
        FOR n = min TO max
          sum = sum + MCAChannel(n)
        NEXT n

        IF sum > 0 THEN sum = sum / kernel2

        MCAData(i) = sum

      NEXT i

'
**********************************************************************

      GOSUB Fluence:

      FOR i = Offset TO MaxChan
        MCAChannelA(i) = MaxDataValue - MCAData(i)
      NEXT i

' *** PEAK IDENTIFICATION AND ANALYSIS ***
'   The interval is numerically identical to the average half-width of
'   an average photopeak at its base.

      interval = PeakInterval

      FOR i = Offset TO MaxChan
        sum = 0

        min = i - interval
          IF min < 0 THEN min = 0
        max = i + interval
          IF max > MaxChan THEN max = MaxChan

          sum = (MCAData(min) - (2 * MCAData(i)) + MCAData(max))

          IF sum > 0 THEN sum = 0
          Peak(i) = sum
          MCAArray1(i) = sum
      NEXT i


' *** VALLEY IDENTIFICATION AND ANALYSIS ***
'   The interval is numerically identical to the average half-width
'   between the maximas of two adjacent photopeaks.

      interval = ValleyInterval

      FOR i = Offset TO MaxChan
```

```
        sum = 0

        min = i - interval
          IF min < 0 THEN min = 0
        max = i + interval
          IF max > MaxChan THEN max = MaxChan

          sum = (MCAChannelA(min) - (2 * MCAChannelA(i)) +
MCAChannelA(max))
          IF sum > 0 THEN sum = 0
          Valley(i) = sum
       NEXT i

'
*************************************************************************
' *** End of Initial Data Processing ***
'
*************************************************************************

       GOSUB PeakFormat:
       GOSUB ValleyFormat:
       GOSUB Continuum:
       GOSUB PeakCalc:
       GOSUB GaussFit:

' *** Save Analysis to File

     filename$ = "C:\phd\thesis.phd\data\am241.dat"
     OPEN filename$ FOR OUTPUT AS #1
     FOR i = 1 TO MaxChan
      PRINT #1, i, MCAData(i), MCAData1(i)
     NEXT i
     CLOSE

     PRINT "Continuum Points"
     PRINT "----------------"
     filename$ = "C:\phd\thesis.phd\data\continuu.dat"
     OPEN filename$ FOR OUTPUT AS #1
     FOR i = 1 TO MaxChan
      IF ValleyA(i) = 0 THEN EXIT FOR
      PRINT i; INT(ValleyA(i)); INT(MCAData(ValleyA(i))); INT(ValleyA(i + 1) -
      ValleyA(i)); INT(PeakArea(i)); INT(Continuum0(i))
      PRINT #1, ValleyA(i), MCAData(ValleyA(i))
     NEXT i
     CLOSE

     PRINT "Spectrum Analysis"
     PRINT "----------------"
     filename$ = "C:\phd\thesis.phd\data\spectrum.tbl"
```

```
    OPEN filename$ FOR OUTPUT AS #1
    PRINT #1, "No.  Centroid  Peak Height  Peak Width  Area  Continuum"
    PRINT #1, "-------------------------------------------------------"
    FOR i = 1 TO MaxChan
     IF ValleyA(i) = 0 THEN EXIT FOR
     channel = PeakA(i)
     height = MCAData1(PeakA(i))
     PeakWidth = ValleyA(i + 1) - ValleyA(i)
     Size = PeakArea(i)
     Continuum1 = Continuum0(i)
     Ratio = (Size / height)
     Ratio1 = (Size / PeakWidth)
     PRINT i; channel; TAB(17); height; PeakWidth; Size; Continuum1; Ratio;
      Ratio1
     PRINT #1, i; channel, height, PeakWidth, Size, Continuum1
    NEXT i
    CLOSE

    GOSUB PeakScan:
    END


PeakFormat:
i = 0
j = 0
DO WHILE i < MaxChan
  i = i + 1
  IF i > MaxChan THEN RETURN
  IF Peak(i) < 0 THEN
    suma = 0
    sumb = 0
    DO WHILE Peak(i) < 0
      suma = suma + Peak(i)
      sumb = sumb + Peak(i) * i
      i = i + 1
      IF i > MaxChan THEN RETURN
    LOOP
    j = j + 1
    x = sumb / suma
    PeakA(j) = x
    MaxPeaks = j
  END IF
LOOP
RETURN


ValleyFormat:
' This routine calculates the mean position of the valley minima, however,
' it is prone to slight statistical fluctuations due to peak shape. This
```

' is corrected in the numerical Valleyscan routine:-

```
i = 0
j = 0
DO WHILE i < MaxChan
  i = i + 1
  IF Valley(i) < 0 THEN
    suma = 0
    sumb = 0
    DO WHILE Valley(i) < 0
      suma = suma + Valley(i)
      sumb = sumb + Valley(i) * i
      i = i + 1
      IF i > MaxChan THEN EXIT DO
    LOOP
    j = j + 1
    x = sumb / suma
    ValleyA(j) = x
    IF j = 1 THEN ValleyA(1) = Offset
  END IF
LOOP

Valleyscan:
 ' *** This routine defines precise data points which mark the lowest
 '    point of each inter-peak valley. These points mark out the spectral
 '    continuum present in each spectrum, and can be used to produce
 '    background subtraction data.  This data can also be used to define
 '    the peak limits in the Gaussian peak fit routine.

   FOR j = 1 TO (MaxPeaks - 1)
    MinDataValue = MCAData(INT(ValleyA(j + 1)))
    MinDataPos = ValleyA(j + 1)
     FOR i = INT(PeakA(j)) TO INT(PeakA(j + 1))
      x = MCAData(i)
      IF x <= MinDataValue THEN
       MinDataValue = x
       MinDataPos = i
      END IF
     NEXT i
     ValleyA(j + 1) = MinDataPos
   NEXT j
RETURN

Continuum:
' *** Continuum Subtraction
    FOR j = 1 TO MaxPeaks - 2

      Grad1 = (MCAData(ValleyA(j + 1)) - MCAData(ValleyA(j)))
      Grad2 = (ValleyA(j + 1) - ValleyA(j))
```

```
      IF Grad2 <> 0 THEN
           gradient = Grad1 / Grad2
      ELSE
           gradient = 0
      END IF

      Intercept = MCAData(ValleyA(j)) - gradient * ValleyA(j)

      sum = 0
      FOR i = INT(ValleyA(j)) TO INT(ValleyA(j + 1)) - 1
       Contin = (gradient * i + Intercept)
       calc = MCAData(i) - Contin
       IF calc <= 0 THEN
        MCAData1(i) = 0
       ELSE
        MCAData1(i) = calc
       END IF
       sum = sum + Contin
      NEXT i
      Continuum0(j) = sum
    NEXT j
RETURN

PeakCalc:
' *** This routine calculates individual photopeak areas
    FOR j = 1 TO MaxPeaks - 2
      sum = 0
      FOR i = INT(ValleyA(j)) TO INT(ValleyA(j + 1)) - 1
       sum = sum + MCAData1(i)
      NEXT i
      PeakArea(j) = sum
    NEXT j
RETURN

Fluence:
'*** This routine corrects data for incident photon fluence,  Livetime,
'   geometry of the source and the quantum branching ratio of the decay.

    FOR i = 1 TO MaxChan
      counts = MCAData(i)
      counts = counts / (livetime * Activity * dOmega * Branch)
      MCAData(i) = counts
    NEXT i
    MaxDataValue = MaxDataValue / (livetime * Activity * dOmega * Branch)
RETURN

GaussFit:
' *** This routine fits Gaussians to all photopeaks.
```

```
    PRINT "Gaussian Peak Fitting"
    PRINT "--------------------"
    CLOSE
    filename$ = "C:\phd\thesis.phd\data\Gaussian.dat"
    OPEN filename$ FOR OUTPUT AS #1

    filename$ = "C:\phd\thesis.phd\data\Gaussian.tbl"
    OPEN filename$ FOR OUTPUT AS #2
     PRINT #2, "No.  Centroid   xbar   Coeff   Area   [Chan.Width="; CW; "]"
     PRINT #2, "-------------------------------------------------------------------------"

    ' Generally, no more than twelve photoelectron peaks can be resolved,
    ' with latter peaks exhibiting such extreme statistical fluctuations
    ' that they cannot be easily defined, even with smoothing.  Since less
    ' than 1% (>=0.1%) of the spectrum resides in this range, it is
    ' convenient to ignore their contribution.  Otherwise (MaxPeaks-2) can
    ' be used.

    FOR j = 1 TO 12
     IF PeakArea(j) = 0 THEN EXIT FOR
     prob = MCAData1(PeakA(j)) / PeakArea(j)
     xbar = ((1 / prob) ^ 2) / (2 * pi)
     Coeff = MCAData1(PeakA(j)) / prob
     PeakProb(j) = xbar
     PeakMaxima(j) = Coeff
     PRINT j; PeakA(j); PeakProb(j); PeakMaxima(j)

     min = PeakProb(j) - CW
     max = PeakProb(j) + CW
     shift = PeakProb(j) - PeakA(j)
     IF max > MaxChan THEN max = MaxChan
     FOR i = min TO max
        Gauss = PeakMaxima(j) * ((1 / SQR(2 * pi * PeakProb(j))) * EXP(-((i -
                PeakProb(j)) ^ 2) / ((2 * PeakProb(j)))))
        PeakX = INT(i - shift)
        PRINT #1, PeakX, Gauss
     NEXT i
     PRINT #1, "//nc"
     PRINT #2, j, PeakX, PeakProb(j), PeakMaxima(j), PeakArea(j)
    NEXT j
    CLOSE
RETURN


PeakScan:
   CLOSE
   filename$ = "C:\phd\thesis.phd\data\Maxima.dat"
   OPEN filename$ FOR OUTPUT AS #1
   FOR j = 1 TO (MaxPeaks - 1)
```

```
    MaxDataValue = MCAData1(INT(PeakA(j)))
    MaxDataPos = PeakA(j)
     FOR i = INT(ValleyA(j)) TO INT(ValleyA(j + 1))
      x = MCAData1(i)
      IF x > MaxDataValue THEN
       MaxDataValue = x
       MaxDataPos = i
      END IF
     NEXT i
     PeakMax(j) = MaxDataPos
     PRINT j; PeakA(j); PeakMax(j); MCAData1(PeakMax(j))
     PRINT #1, PeakMax(j); MCAData1(PeakMax(j))
   NEXT j
   CLOSE
RETURN
```

BIBLIOGRAPHY

Ajitanand N.N. and Iyengar K.N., *On the Technique of Preparation of High Quality Thin Film Scintillators,* Nucl. Instrum. Meth., **133**, 71-74 (1976)

Alkharam, A.S., *Specification of the Quality of Ionising Radiations for Unified Dosimetry in Radiobiology and Radiation Protection.*, Department of Physics and Astronomy, University of St Andrews, 58-140

Alkharam, A.S. and Watt, D.E., *Risk Scaling Factors from Inactivation to Chromosome Abberations, Mutations and Oncogenic Transformations in Mammalian Cells,* Rad. Prot. Dosim., **70** (1-4), 537-540 (1997)

Anderson W, and Belchar E.H., *A standard light source of very low intensity based on the Cerenkov effect,* Brit. Jnl. Appl. Phys., **5/12**, 53-57 (1954)

Arfken G., *Mathematical Methods for Physicists, 3rd Edition,* Academic Press Inc, New York (1985)

Ballini J-P., *Spectres D'Impulsions à «Un Photoélectron» des Photomultiplicateurs,* Nucl. Instrum. Meth., **116**, 109-121 (1974)

Ballini J-P., Cazes P. and Turpin P-Y., *Single Electron Multiplication Statistics as a Combination of Poissonian Pulse height Distributions Using Constraint Regression Methods,* Nucl. Instrum. Meth., **134**, 319-330 (1976)

Bartlett M.S., *Stochastic Processes*, Cambridge University Press (1955)

Beaumontt G.P., *Probability and Random Variables*, Ellis Horwood (1986)

Becchetti F.D., Thorn C.E. and Levine M.J., *Response of Plastic Scintillator Detectors to Heavy Ions $Z \leq 35$, $E \leq MeV$,* Nucl. Instr. Meth., **138**, 93-104, (1976)

Bedder A.S., Mackie T.R. and Attix F.H., *Water-equivalent plastic scintillation detectors for high energy beam dosimetry: I. Physical characteristics and theoretical considerations* , Phys. Med. Biol., **37** (10), 1883-1900, (1992)

Bedder A.S., Mackie T.R. and Attix F.H., *Cerenkov light generated in optical fibres and other light pipes irradiated by electrons beams,* Phys. Med. Biol., **37** (4), 925-935, (1992)

Belchar E.H., *The luminescence of irradiated transparent media and the Cerenkov Effect,* Proc. Roy. Soc., **A216**, 90-102 (1953)

Bendiscolli G., Filippini V., Marciano C., Rotondi A. and Zenoni A., *Performance of a Thin Film Scintillator Detector,* Nucl. Instrm. Meth., **227**, 478-482 (1984)

Bengston B. and Moszynski M., *Energy-transfer and Light-Collection Characteristics for Different Types of Plastic Scintillator,* Nucl. Instrum. Mthd., **117**, 227-232 (1974)

Bewley D.K., *Radiation Quality and its Influence on Biological Response,* Brit. Med. Biol., **29(1)**, 7-11 (1973)

Birks J.B., *Scintillations from Organic Crystals: Specific Fluorescence and Relative Response to Different Radiations,* Proc. Phys. Soc, **A64**, 874-877 (1951)

Birks J.B., *The Theory and Practice of Scintillation Counting*, Pergamon Press (1964)

Blanc D., Cambou F. and De Laford Y.G., *Cinétique de la composante rapide de la scintillation dans un milieu organique pur,* Acad. Sci., **254**, 3187-3189 (1962)

Bowen E.J., Mikiewicz E. and Smith F.W., *Resonance Transfer of Electronic Energy in Organic Crystals,* Proc. Phys. Soc. A62, 26-31 (1949)

Brannen E. and Olde G.L., *The Response of Organic Scintillators to Electron Energy Deposited in Them,* Rad. Res., **16**, 1-6 (1962)

Brooks F.D. *Development of Organic Scintillators*, Nucl. Instrum. Meth., **162**, 477-505 (1979)

Brooks F.D., Cilliers W.A, and Allie M.S., *Response of thin NE102 scintillator films to fission fragments,* Nucl. Instr. Meth., **A240**, 338-342 (1985)

Browne E., Firestone R.B. and Shirley V.S., *Table of Radioactive Isotopes*, John Wiley & Sons, Inc. (Wiley-Interscience) (1986)

Burchan W.E., *Nuclear Physics: An Introduction*, Longman, London (1973)

Butts J.J. and Katz R., *Theory of RBE for Heavy Ion Bombardment of Dry Enzymes and Viruses,* Rad. Res., **30**, 855-871 (1967)

Chen C.Z. and Watt D.E., *Biophysical Mechanisms of radiation damage to mammalian cells by X- and γ-rays,* Int. J. Radiat. Biol, **49**(1), 131-142, (1986)

Choi S.I. and Rice S.A., *Exciton-Exciton Interactions and Photoconductivity in Crystalline Anthracene*, J. Chem. Phys., **38**(2), 366-373 (1963)

Chou C.N., *Internal Absorption of Fluorescent Light in Large Plastic Scintillators,* Physics Review, **87**, 376-377 (1952)

Christophorou L.G., *Atomic and Molecular Radiation Physics,* Wiley-Interscience (1971)

Close F., Marten M. and Sutton C., *The Particle Explosion,* Oxford University Press (1987)

D'Ambrosio C., Hao W., You K., Wang Y. and Xu C., *First Results on the hybrid photodiode tube.*, Nucl. Instrum. Meth. **315**, 375-384, (1992)

D'Ambrosio C., Gys T., Leutz D., Piedigrossi C., Puertolas D. and Tailhardat S., *Photon counting with a hybrid photomultiplier tube (HPMT).*, Nucl. Instrum. Meth. **338**, 389-397, (1993)

DEP Delft Instruments, *When Every Photon Counts*, DEP (BV Delft Electronische Producten, Dwazziewegen 2, Roden, Postbus 60, 9300 AB Roden, The Netherlands, (1995)

Edwards J., *Integral Calculus for Beginners*, MacMillan and Co., London (1896)

EMI Electron Tubes, *Photomultipliers and Accessories*, Electron Tubes Ltd, Bury Street, Ruislip, Middlesex HA4 7TA (1995)

Ettinger, G.M., *Some Properties of Light Guides,* Rev. Sci. Instr., **26 (8)**, 763-764 (1955)

Evans H.C. and Bellamy E.H., *The Response of Plastic Scintillators to Protons,* Proc. Phys. Soc. Res. Notes., **74**, 483-485 (1959)

Fessenden R.J. and Fessenden J.S., *Organic Chemistry 3rd Edition*, Brooks/Cole Publishing Company, Monterey, California (1986)

Feynman R.P., *QED: The Strange Theory of Light and Matter*, Penguin Science (1985)

Feynman R.P., Leighton R. B. and Sands M., *The Feynman Lectures on Physics Volume 1*, Addison-Wesley Publishing Company (1963)

Fowler G.N., *Excitons in molecular crystals,* Molecular Physics, **8**, 375-382 (1964)

Frankenberg D., *Repair of DNA Double-Strand Breaks and its Effect on RBE,* Adv. Space Res. **14**, 235-248, (1980)

Halliday D., *Introductory Nuclear Physics 2nd Edition,* John Wiley & Son, New York (1951)

Hammersley J.M. and Handscomb D.C., *Monte Carlo Methods,* Methuen & Co Ltd, London, 1975

Harvey J.A. and Hill N.W., *Scintillation Detectors for Neutron Physics Research,* Nucl. Instrum. Meth., **162**, 507-529 (1979)

Heitler W., *The Quantum Theory of Radiation,* Clarendon Press, Oxford (1936)

Houtermans H., *Probability of Non-Detection in Liquid Scintillation Counting,* Nucl. Inst. Meth, **112**, 121-130 (1973)

Hubbell J.H., *Photon Mass Attenuation and Energy-Absorption Coefficients from 1 keV to 20 MeV,* Int. J. Appl. Radiat. Isot., **33**, 1269-1290 (1981)

IAEA, *Biomedical Dosimetry: Physical Aspects, Instrumentation, Calibration,* IAEA, Vienna (1981)

ICRP Publication 38, *Radionuclide Transformations - Energy and Intensity Emissions,* Pergamon Press, Oxford (1983)

ICRU Report 19, *Radiation Quantities and Units,* ICRU (1971)

ICRU Report 20, *Radiation Protection Instrumentation and its Applications,* ICRU (1971)

ICRU Report 23, *Measurement of Absorbed Dose in a Phantom Irradiated by a Single Beam of X or γ Rays,* ICRU (1973)

ICRU Report 28, *Basic Aspects of High Energy Particle Interactions and Radiation Dosimetry,* ICRU (1978)

ICRU Report 32, *Methods of Assessment of Absorbed Dose in Clinical Use of Radionuclides,* ICRU (1979)

Jelley J.V., *Cerenkov Radiation and its Applications,* Pergamon Press (1958)

Jortner J., Choi S., Katz J.L. and Rice S.A., *Triplet Energy Transfer and Triplet-Triplet Interaction in Aromatic Crystals,* Phys. Rev. Letters, **11**(7), 323-326 (1963)

Jung P. and Wiesenfeld K., *Too quiet to hear a whisper,* Nature, **385**, 291 (1997)

Kallman H. and Brucker G.J., *Decay Times of Fluorescent Substances Excited by High-Energy Radiation,* Phys. Rev. **108**, 1122-1130(1957)

Kanno I. and Nakagome Y., *A new model of Luminescence in a Very Thin Plastic Film,* Nucl. Instrum. Meth. Phys. Rev., **A244**, 551-555 (1986)

Kanno I. and Nakagome Y., *Response Characteristics of Thin Film Detectors to Fission Fragments,* Nucl. Instrum. Meth. Phys. Rev., **A251**, 108-114 (1986)

King T.A. and Voltz R., *The time dependence of scintillation intensity in aromatic materials,* Proceedings of Royal Society, **289**, 424-439 (1966)

Kilvington A.I., Baker C.A. and Illinesi P., *Reflective Coverings For Scintillation Counters*, Nucl. Instrum. Meth., **80**, 177-178 (1970)

Knoll G.F., *Radiation Detection and Measurement - Second Edition*, John Wiley & Son, New York (1986)

Kohl J.W., *Response of Various Thin-Film Scintillators to Low-Energy Particles,* Nucl. Instrum. Meth., **125**, 413-417 (1975)

Koskelo M.J., Aarnio P.A. and Routti J.T., *Sampo80: An Accurate Gamma Spectrum Analysis Method for Minicomputers*, Nucl. Instrum. Meth., **190**, 89-99, (1981)

Kucherov, I.Ia. and Faidysh, A.N., *Migration and Transfer of Electron Excitation Energy in Anthracene and Naphthalene Crystals*, Bull. Acad. Sci. USSR. Phys. Rev., **22**, 27-33 (1958)

Longair M.S., *High Energy Astrophysics*, Cambridge University Press (1981)

McIntyre J.A. and Hofstadter R., *Measurement of Gamma-Ray Energies with One Crystal*, Phys. Rev, **78 (5)**, 617-618 (1950)

McIntyre J.A. and Hofstadter R., *Measurement of Gamma-Ray Energies with Two Crystals in Coincidence*, Phys. Rev, **78 (5)**, 619-620 (1950)

Manduchi C., Russo-Manduchi M.T. and Segato G.F., *Response of Ultra-Thin Scintillation Foils to Fission Fragments,* Nucl, Instrum. Meth. Phys. Rev. A243, 453-458 (1986)

Marscotti M.A., *A Method For Automatic Identification of Peaks in the Presence of Background and its Application to Spectrum Analysis*, Nucl. Instrum. Meth., **50**, 309-320 (1967)

Mehra J., *The Beat of a Different Drum - The Life and Science of Richard Feynman*, Oxford University Press (1996)

Morton G.A., *Time resolution of scintillation counters*, Nucleonics, **10 (3)**, 39 (1952)

Muga L. and Griffith G., *Response of thin film scintillator detector to light and heavy ions,* Nucl. Instrum. Meth., **109**, 289-295 (1973)

Muga L. and Griffith G., *Thin film detector response to the passage of Accelerated Heavy Ions,* Nucl. Instrum. Meth., **111**, 581-585 (1973)

Muga L. and Griffith G., *Specific response studies in plastic scintillators,* Phys. Rev, **9** (9), 3639-3649 (1974)

Nuclear Enterprises, *Scintillation Materials*, NE Technology, Materials Division, Bankhead Medway, Sighthill, Edinburgh EH11 4BY, (1995)

Newman E. and Steigert F.E., *Response of NaI(Tl) to Energetic Heavy Ions,* Phys. Rev., **118** (6), 1574-1578 (1960)

Newman E., Smith A.M. and Steigert F.E., *Fluorescent Response of Scintillation Crystals to Heavy Ions*, Phys. Rev., **122** (5), 1520-1524 (1961)

Prescott J.R., *A Statistcial Model for Photomultiplier Single-Electron Statistics,* Nucl. Instrum. Meth., **39**, 173-179 (1966)

Prescott J.R. and Rupaal A.S., *The Specific Fluorescence of Plastic Scintillation NE102,* Canad Jnl. Phys., **39**, 221-227 (1961)

Roff W.J., *Fibres, Plastics and Rubbers - A handbook of common polymers,* Butterworth Scientific Publications, London (1956)

Rosenstock H.B. and Schulman J.H., *Models for Luminescence Degradation in Organic Solids,* Jnl. Chem. Phys., **30**, 1, 116-125(1959)

Rossi B., *High Energy Particles,* Constable and Co. Ltd, London (1952)

Sandor T., *Single Electron Pulse Height Distribution of Photomultipliers,* Nucl. Instrum. Meth., **78**, 8-10 (1970)

Schorr M.G. and Torney F.L., *Solid Non-Crystalline Scintillation Phosphors,* Phys. Rev., **80,** 474 (1950)

Semat H., *Introduction to Atomic and Nuclear Physics*, Chapman & Hall (1965)

Simpson, O., *Electronic properties of aromanic hydrocarbons. III. Diffusion of Excitons*, Proc. Roy. Soc., A328, 402-411 (1956)

Smith C.M.H., *Textbook of Nuclear Physics,* Pergamon Press, London (1965)

Smith D.L., Polk R.G. and Miller T.G., *Measurement of the Response of Several Organic Scintillators to Electrons, Protons and Deuterons,* Nucl. Instrum. Meth., **64**, 157-166 (1968)

Sowerby B.D., *Cerenkov Detectors for Low-Energy Gamma Rays,* Nucl. Instrum. Meth., **67**, 145-149 (1971)

Sternlicht H., Nieman G.C. and Robinson G.W., *Triplet-Triplet Annihilation and Delayed Fluorescence in Molecular Aggregates,* Jnl. Chem. Phys., **38**(6), 1326-1335 (1963)

Swank R.K., *Slow-neutron liquid-scintillation detector*, Nucleonics, **10 (3)**, 38 (1952)

Timmerhaus K.D., Giller E.B., Duffield R.B. and Drickamer H.G., *Scintillation Conducting Rods in Tracer Work*, Nucleonics, June, 37-41, (1950)

Tove P.A., *Scintillation Spectrometry Using Long Light Guides*, Rev. Sci. Instr., **27 (3)**, 143-146, (1956)

Vlasov V.K. and Karezin V.V., *Microdosimetric model of accumulation of ionizing radiation by solid-state dosimeters*, Moscow State University, (1991), Unpublished

Voltz R., Lopes Da Silva. J., Laustrait G. and Coche A., *Influence of the Nature of Ionizing Particles on the Specific Luminescence of Organic Scintillators*, Jnl. Chem. Phys., **45**(9), 3306-3311 (1966)

Watt D.E, Al-Affan I.A.M., Chen C.Z., and Thomas G.E., *Identification of Biophysical Mechansims of Damage by Ionising Radiations*, Rad. Prot. Dosim., **13**(4), 285-294 (1985)

Watt D.E., *On Absolute Biological Effectiveness and Unified Dosimetry*, J. Radiol. Prot., **9**(1), 33-49 (1989)

Watt D.E., *An Approach towards a Unified Theory of Dosimetry to Mammalian Cells by Ionising Radiations for Absolute Dosimetry*, J. Radiol. Prot. **27**(2), 73-84 (1989)

Watt D.E., and Kadiri L.A., *Physical Quantification of the Biological Effectiveness of Ionising Radiations*, Int. J. Quant. Chem., **38**, 501-520, (1990)

Watt D.E., *Track Structure Data for Ionising Radiations in Liquid Water - Part 2 Neutrons: 100 keV to 100 MeV*, University Report BIOPHYS/11/93, Univ. of St Andrews (1993)

Watt D.E., *Track Structure Data for Ionising Radiations in Liquid Water - Part 2 Heavy Charged Particles: 100eV/A to 1GeV/A*, University Report BIOPHYS/1/93, Univ. of St Andrews (1994)

Watt D.E., *Quantities for Generalised Dosimetry of Ionising Radiations in Medicine and Protection - Part 1 Electrons and Photons*, University Report BIOPHYS/6/95, Univ. of St Andrews (1995)

Watt D.E. and Alkharam A.S., *A feasibility study of scintillator microdosimeters for measurement of the biological effectiveness of Ionising Radiations*, Radiat. Prot. Dosim., **61**(1-3), 211-214 (1995)

Watt D.E., *Quantities for Dosimetry of Ionising Radiations in Liquid Water,* Taylor & Francis, London (1996) ISBN 0-7484-0484-8

Watt D.E., *A Unified System of Radiation Bio-Effectiveness and its Consequences in Practical Applications,* Rad. Prot. Dosim, **70**(1-4), 529-536, (1997)

Wehr M.R., Richards J.A. and Adair T.W., *Physics of the Atoms,* Addison-Wesley Publishing Company, (1984)

Wright G.T., *Scintillation Response of Organic Phosphors,* Phys. Rev., **91**, 1282-1283 (1953)

Yang T.C., Craise L.M., Mei M. and Tobias C.A., *Neoplastic Cell-Transformation by High-LET Radiation - Molecular Mechanisms,* Life Sci. Space Res., XXIII **10**, 131-140 (1989)